Numerical and Experimental Investigation of the Hemodynamics of an Artificial Heart Valve

by

Kyle Davis

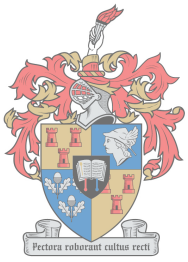

Thesis presented in partial fulfilment of the requirements for the degree of Master of Engineering (Mechanical) in the Faculty of Engineering at Stellenbosch University

Supervisor:	Dr. J.H. Müller
Co-supervisor:	Prof. C.J. Meyer
	Prof. F.E. Smit

December 2018

Declaration

By submitting this thesis electronically, I declare that the entirety of the work contained therein is my own, original work, that I am the sole author thereof (save to the extent explicitly otherwise stated), that reproduction and publication thereof by Stellenbosch University will not infringe any third party rights and that I have not previously in its entirety or in part submitted it for obtaining any qualification.

Date: ..... December 2018 .....

Plagiarism Declaration

1. Plagiarism is the use of ideas, material and other intellectual property of another's work and to present it as my own.
2. I agree that plagiarism is a punishable offence because it constitutes theft.
3. I also understand that direct translations are plagiarism.
4. Accordingly all quotations and contributions from any source whatsoever (including the internet) have been cited fully. I understand that the reproduction of text without quotation marks (even when the source is cited) is plagiarism.
5. I declare that the work contained in this assignment, except where otherwise stated, is my original work and that I have not previously (in its entirety or in part) submitted it for grading in this module/assignment or another module/assignment.

Student number	Signature
Initials and surname K Davis	Date

Abstract

Numerical and Experimental Investigation of the Hemodynamics of an Artificial Heart Valve

K. Davis

Department of Mechanical and Mechatronic Engineering,
University of Stellenbosch,
Private Bag X1, Matieland 7602, South Africa.

Thesis: MEng (Mech)

December 2018

Artificial heart valves used during valve replacement surgery currently suffer from fatigue (biological valves) or thrombosis (mechanical valves). This study focused on the experimental testing and simulation of a new polyurethane valve (PV tall) based on a previous polyurethane valve design. The new PV tall valve was experimentally evaluated against the original polyurethane design (PV short) and a commercially available tissue valve (tissue), as well as numerically simulated.

All three valves were evaluated in a ViVitro Labs pulse duplicator to determine the pressure drop, effective orifice area and percentage regurgitation as required by FDA and ISO regulation. The PV tall valve had a noticeable decrease in the pressure drop and percentage regurgitation compared to the PV short valve, whereas the commercial tissue valve had the lowest values. The effective orifice area of the PV tall valve outperformed the tissue valve at larger cardiac outputs.

Particle image velocimetry testing was performed on all three valves during pulse duplication. The obtained velocity vector fields were examined and the viscous shear stress (VSS), Reynolds shear stress (RSS), major Reynolds shear stress (RSS_{maj}) and turbulent viscous shear stress (TVSS) was determined to predict the onset of hemolysis and platelet activation. The measured VSS was below the threshold for both platelet activation and hemolysis, however the TVSS predicted that platelet activation could potentially occur for all three valves. The RSS_{maj} value predicted that both platelet activation and hemolysis would occur. The RSS_{maj} and RSS values were found to be subject to manipulation through filtering of large velocity fluctuations, however the VSS and TVSS values did not vary significantly through filtering.

A numerical simulation procedure was developed using only open-source software to perform fluid-structure interaction simulations of the newly designed PV tall heart

valve. The simulations were performed using openFOAM and CalculiX, and were coupled together using preCICE. The speed and stability of strongly coupled implicit simulations were significantly improved with the use of fast Quasi-Newton coupling schemes compared to conventional Aitken under-relaxation. The simulations were able to predict the VSS within the fluid domain, after which the wall shear stress (WSS) was obtained from the simulations. The WSS was orders of magnitude larger than the VSS, indicating that the WSS could be a much larger cause of platelet activation and hemolysis.

This study demonstrated the effective use of pulse duplication and particle image velocimetry to experimentally evaluate heart valve hemodynamics. The study also shows that mesh based fluid-structure interaction simulations are capable of providing an early design stage indication of heart valve hemodynamic performance, reducing manufacturing and experimental turn-around times and reducing cost.

Uittreksel

Numeriese en Eksperimentele Ondersoek na die Hemodinamika van 'n Kunsmatige Hartklep

("Numerical and Experimental Investigation of the Hemodynamics of an Artificial Heart Valve")

K. Davis

Departement Meganiese en Megatroniese Ingenieurswese,
Universiteit van Stellenbosch,
Privaatsak X1, Matieland 7602, Suid Afrika.

Tesis: MIng (Meg)

Desember 2018

Kunsmatige hartkleppe wat gedurende klepvervangingchirurgie aangewend word, lei tans aan afmatting (biologies kleppe) of trombose (meganiese kleppe). Hierdie studie fokus op die eksperimentele toetsing en simulasie van 'n poliuretaanklep (PK lang) wat op 'n vorige ontwerp gebaseer is. Die nuwe PK langklep is eksperimenteel teen die oorspronklike poliuretaanontwerp (PK kort) en 'n weefselklep wat kommersiëel beskikbaar is beoordeel.

Die drie kleppe is almal volgens die regulasies soos deur die FDA en ISO vereis word in 'n ViVitro Labs polsduplikator beoordeel om sodoende die drukval, effektiewe openingsarea en herhalingspersentasie te bepaal. Die PK langklep het 'n merkbare verlaging in die drukval en herhalingspersentasie getoon in vergelyking met die PK kortklep, terwyl die kommersiële weefselklep die laagste waardes getoon het. Die effektiewe openingsarea van die PK langklep het die weefselklep tydens groter kardiale uitsette geklop.

Partikelbeeldsnelheidsmetingtoetsing is tydens polsduplikasie op al drie kleppe uitgevoer. Die stroomsnelheidsvektorvelde wat opgelewer is, is ondersoek en die viskose skuif sterkte (VSS), Reynolds skuif sterkte (RSS), hoof Reynolds skuif sterkte (RSS_{hoof}), en die turbulente viskose skuif sterkte (TVSS) is bepaal om die aanvangs van hemolise en plaatjie-aktivering te voorspel. Die gemete VSS was onder die drempel vir beide plaatjieaktivering en hemolise, hoewel die TVSS voorspel het dat plaatjieaktivering potensiëel vir al drie kleppe kon plaasvind. Die RSS_{hoof}-waarde het voorspel dat beide plaatjieaktivering en hemolise sou plaasvind. Daar is gevind dat beide die RSS_{hoof}- en RSS-waardes aan manipulasie deur filtrering van hewigefluktuasie in snelheid onderhewig is, tog het die VSS- en TVSS-waardes nie beduidend deur filtrering gewissel nie.

‘n Numeriese simulasieprosedure, wat slegs van oopbron sagteware gebruik maak, is ontwikkel ten einde vloeistofstruktuur interaksiesimulasies van die nuut-ontwerpte PV langklep uit te voer. Die simulasies is uitgevoer deur gebruik te maak van openFOAM en CalculiX en is saamgekoppel deur preCICE daarvoor in te span. Die spoed en stabiliteit van sterk-gekoppelde implisiete simulasies is beduidend verbeter deur die gebruik van vinnige Kwasi-Newton koppelingskemas vergeleke met konvensionele Aitken onderontspanning. Die simulasies was daartoe in staat om die VSS binne die vloeistofomgewing te voorspel waarna die wand skuif sterkte (WSS) van die simulasies af verkry is. Die WSS was orde van grootte meer as die VSS, wat aangedui het dat die WSS ‘n baie groter oorsaak van plaatjieaktivering en hemolise kan wees.

Hierdie studie demonstreer die effektiewe gebruik van polsduplikasie en partikelbeeldsnelheidsmeting om hartklephemodinamika eksperimenteel te evalueer. Die studie wys ook verder dat stofdigtheidsgebaseerde vloeistofstruktuurinteraksie simulasies daartoe in staat is om in ‘n vroeë ontwerpstadium ‘n aanduiding te gee van hemodinamiese hartkleppresta sie, wat vervaardigings- en eksperimentele omdraaitye asook koste verminder.

Acknowledgements

This study would not have been possible without the contributions of many people. I would like to thank:

- My supervisors Dr. Cobus Müller, Prof. Chris Meyer and Prof. Francis Smit. Their guidance and patience was invaluable throughout this study. I thank them for their financial support, and providing me with the opportunity to travel and learn from experts around the world.
- Everyone at the Cardiothoracic Surgery Department for the interesting conversations and much needed coffee breaks in the office, and for making the move to Bloemfontein easier than expected.
- The Centre for Rapid Prototyping and Manufacturing at the Central University of Technology, for their assistance with manufacturing of the heart valves.
- The preCICE research group at the Technical University of Munich and the University of Stuttgart, for their assistance with the simulations and financial assistance to attend the ECCOMAS conference.
- The group at BERG, for always making trips down to Stellenbosch an enormous amount of fun.
- Lastly, I would like to thank my family and friends for their unwavering support throughout this endeavour. I would especially like to thank my mother and sister, Maria and Samantha, for always listening to my frustrations and for offering advice, regardless of the challenges I faced.

Dedications

This thesis is dedicated to my late father, Michael Davis, who instilled a wonderful passion for engineering in me.

Contents

List of Figures

List of Tables

Nomenclature

Constants

C_μ	Eddy dissipation constant = 0.09
C_s	Smagorinsky constant = 0.17
g	Gravitational constant = 9.81 m/s^2

Variables

D	Diameter of tube
E	Young's modulus
f	Body force in fluid
I	Turbulent intensity
M	Degree of polynomial expansion
N	Number of cycles, or Number of points
P	Pressure
ΔP	Average pressure drop
Q_{rms}	Root mean square of the volumetric flow rate
q_v	Volumetric flow rate
Re	Reynolds number
RV	Regurgitation Volume
S_{ij}	Resolved scale strain rate tensor
t	Time
u, v	Instantaneous velocity
$\bar{U}, \bar{V}$	Mean velocity
u', v'	Fluctuating velocity
x, y, z	Direction
y$^+$	Wall y$^+$
Δ	Measurement point distance
δ_{ij}	Kronecker delta
ϵ	Turbulence dissipation rate

ε	Turbulent dissipation rate
Γ	Domain boundary
κ	Turbulent kinetic energy
λ	Quasi-Newton coefficients
μ	Dynamic viscosity
ν	Kinematic viscosity
Ω	Continuum domain
ω	Specific eddy dissipation rate, or Aitken relaxation factor
ϕ	Radial basis function interpolant
ρ	Density
τ_{ij}	Shear stress
τ_v	Turbulent viscous shear stress

Vectors and Tensors

$\boldsymbol{J}_R$	Interface Jacobian
$\boldsymbol{M}_{AA}$	RBF interpolation matrix
$\boldsymbol{P}$	RBF polynomial matrix
$\boldsymbol{R}$	Aitken interface residual
$\boldsymbol{r}$	Interface residual
$\boldsymbol{S}$	RBF solution vector
$\boldsymbol{s}$	Structural interface response
$\boldsymbol{V}$	Interface residual matrix
$\boldsymbol{W}$	Structural interface response matrix
$\boldsymbol{x}$	Aitken interface information
$\boldsymbol{\alpha}$	Radial basis function coefficients
$\boldsymbol{\gamma}$	Radial basis function polynomial coefficient

Superscripts

k	Aitken iterations within time step
n	Time steps

Subscripts

$Aortic$	Aortic
B	Boundary points
cm^2	Area in cm^2
I	Internal points

k	Iterations within time step
$turb$	Turbulent
$Ventricle$	Ventricle

Abbreviations

2D	Two-dimensional
3D	Three-dimensional
ALE	Arbitrary Lagrangian-Eulerian
BPM	Beats per minute
CFD	Computational Fluid Dynamics
CO	Cardiac output
CPD	Cardiac pulse duplicator
CSD	Computational Solid Dynamics
EDP	End diastolic pressure
EOA	Effective orifice area
FDA	Food and Drug Administration
FSI	Fluid-Structure Interaction
IB	Immersed Boundary
IQN-ILS	Interface Quasi-Newton with approximation of the Inverse of the interface Jacobian by Least Squares
ISO	International Organisation of Standards
LES	Large eddy simulation
MAP	Mean aortic pressure
PIV	Particle image velocimetry
PSP	Peak systolic pressure
PV	Polyurethane valve
RBC‘s	Red blood cells
RBF	Radial Basis Function
RSS	Reynolds shear stress
RSS_{maj}	Major Reynolds shear stress
SGS	Sub-grid scale
SST	Shear stress transport
TVSS	Turbulent viscous shear stress
VIA	Viscoelastic impedance adapter
VSS	Viscous shear stress
WHO	World Health Organisation

Chapter 1

Introduction

1.1 Background

Heart valves play a critical role in ensuring that blood flows unidirectionally through the heart, thereby ensuring that blood is oxygenated in the lungs and distributed throughout the body [1]. Heart valves can also be prone to valve disease, being one of the major causes of cardiovascular pathologies, leading to inadequate function of the heart valve. Ageing, birth defects, or diseases, such as rheumatic heart disease or endocarditis, are but a few causes of heart valve failure leading to stenosis or regurgitation [2]. Stenosis occurs when the heart valve leaflets calcify and harden, impairing the heart valves ability to open and increasing the resistance to the flow of blood. Regurgitation occurs when the heart valve does not close correctly or completely, allowing a significant portion of blood to flow backwards into the heart chambers. Significant regurgitation increases the strain on the heart muscles to pump the required amount of blood throughout the body [3]. A cross section of the heart showing the four major heart valves is shown in Figure 1.1.

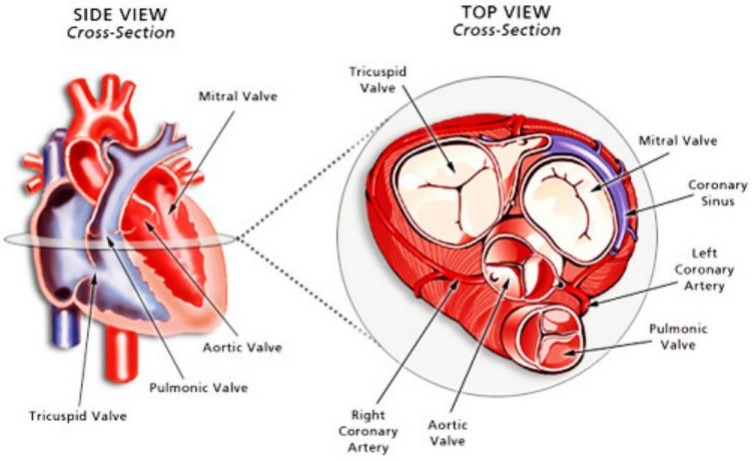

Figure 1.1: A cross section of a human heart showing the four major heart valves (adapted from [4])

A remedy for heart valve failure is for the patient to undergo heart valve replacement surgery, where the native heart valve is replaced with either a mechanical or a biological heart valve. The biological heart valve tends to mimic the natural movement of the leaflets and hemodynamic behaviour of native heart valves, however they suffer from calcification, fatigue damage and leaflet rupture [2]. The mechanical heart valve does not suffer from fatigue as severely as the biological heart valve, however large fluid shear stresses present in the mechanical heart valves causes hemolysis and platelet activation of blood, which can lead to severe thromboembolisms and the formation of blood clots [2; 5]. Patients with mechanical heart valves are required to use anti-coagulation medication, which if not carefully monitored, could lead to thrombosis (blood clots too easily) or bleeding (blood does not clot enough) [6]. Aside from the additional effort of consuming anti-coagulation medication, careful monitoring of anti-coagulant consumption is not always possible for those living in the developing world that do not have access to the necessary health care facilities [7]. The most severe complications of mechanical heart valves and biological heart valves are summarised as; 1) thrombosis and thromboembolism, 2) anti-coagulate related hemorrhage, 3) tissue overgrowth, 4) infection, 5) paravalvular leaks and 6) valve failure due to fatigue and chemical change [8].

Polymer based heart valves, shown in Figure 1.2, have received much attention due to the fact that they have the ability to mimic the physiological flow conditions of a native heart valve, whilst also potentially being cheaper and easier to manufacture [9]. In the past, polymer based heart valves had the tendency to calcify and stiffen, which resulted in a reduction of the fatigue life [10]. Previously, materials such as polyurethanes, polycarbonate urethanes and polyurethane urea have been used to manufacture polymer based heart valves [8]. Recently, large advances have been made regarding polymer based heart valves [11]. New materials, such as Elasteon, have been developed that provide better resistance to bio-degradability, as well as advances in manufacturing techniques providing even leaflet thicknesses, resulting in a higher fatigue life of the valves [10]. These polyurethane based valves with a lower tendency to calcify have the potential to be used for valve replacement [12].

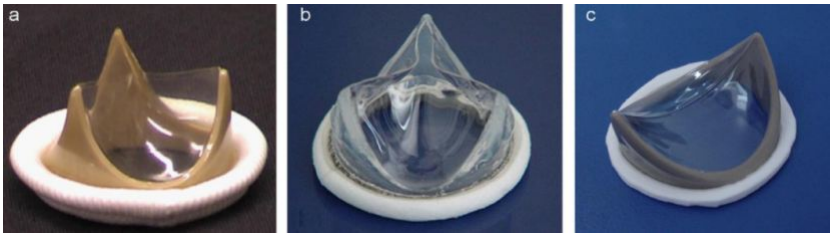

Figure 1.2: Various polymer based heart valves of a frame machined from polyetheretherketone with (a) polyurethane leaflets (b), trileaflet and (c) bileaflet polycarbonate urethane heart valves (adapted from [10])

1.2 Aim and objectives

The aim of this study was to design a polyurethane heart valve, based off a previously designed polyurethane heart valve, in order to evaluate an experimental testing and nu-

merical simulation procedure developed to be used during the design process of heart valves. The new heart valve design will be evaluated and compared to the previous design and a commercially available heart valve using experimental methods. A numerical simulation procedure is to be developed exclusively using open source software that is capable of being used during the design stage of developing a heart valve, and will be used to model the performance of the new heart valve design. A list of the objectives are to:

- Perform a literature study on modern experimental and numerical techniques for determining the hemodynamic performance and modelling of heart valves
- Perform pulse duplication on a commercially available ViVitro Labs Pulse Duplicator at the University of Free State
- Perform particle imaging velocimetry on a custom built pulse duplicator at the University of Stellenbosch
- Develop a numerical procedure capable of simulating the complex fluid-structure interaction of heart valves
- Perform transient fluid-structure interaction simulations of a new polyurethane heart valve
- Analyse and compare the results of the experimental and numerical simulations

1.3 Motivation

The world‘s population is expected to increase to 8.9 billion people by 2050, with the number of heart valve replacement surgeries expected to almost triple to over 850 000 during the same time period [13]. Along with a larger global population, access to proper healthcare in rural areas is on the rise, with people currently living in poverty stricken regions gaining better access to health care. The World Health Organisation (WHO) estimated in 2003 that approximately 1 008 207 children between the ages of 5 and 14 in Sub-saharan Africa suffered from rheumatic heart disease [14]. Rheumatic heart disease has the potential to cause permanent damage to heart valves, leading to heart failure, atrial fibrilation and embolic stroke [14].

With the rise in the number of people that will have access to heart valve replacement surgery, there still exists a need to develop heart valves that do not suffer from fatigue damage, hemolysis and platelet activation. This will prevent re-operation as well as reduce the patient‘s dependency on anti-coagulation medication which is not always accessible to many living in poverty or rural areas [7]. Research and development of polyurethane heart valves has the potential to produce a cost effective heart valve that has an extended fatigue life comparable to mechanical heart valves, whilst requiring very little to no anti-coagulation medication. Designing a trileaflet heart valve using polyurethane also offers advantages during the design stage as fast turn around times can be achieved from initial computer aided design models, numerical simulation, manufacture and experimental testing.

Designing an artificial heart valve is a complex and time consuming process, where strict regulatory requirements must be met from initial experimental and *in vitro* studies

before clinical trials can begin *in vivo*, a process that can spans years. This is where computational modelling of heart valves can significantly reduce the time to perform these initial studies. Furthermore, development of an artificial heart valve by utilising over-the-counter open-source software could potentially reduce the cost of development. Currently, only commercial software packages or custom developed in-house software is utilised in the development of heart valves, significantly increasing development cost.

1.4 Thesis layout

The thesis is organised into the following sections:

Chapter 2: A literature review of the mechanics of trileaflet heart valves is discussed, followed by a review of current pulse duplication and particle image velocimetry experimental techniques for heart valves. The chapter is concluded by an overview of the latest numerical techniques for fluid-structure interaction simulations of heart valves and fluid dynamics.

Chapter 3: The setup and operating conditions for pulse duplication is provided, followed by the results and discussion of the pulse duplication of three trileaflet heart valves.

Chapter 4: The setup and operating conditions of the particle image velocimetry testing is discussed, followed by the results and a discussion of the particle image velocimetry testing on three trileaflet heart valves.

Chapter 5: The development of a numerical procedure is provided. The results from various boundary conditions and numerical simulation coupling is provided, followed by the results and discussion of the numerical simulations of a newly designed trileaflet heart valve.

Chapter 6: The conclusion, limitations and future work of heart valve development is discussed.

Chapter 2

Literature Review

2.1 Fluid mechanics of heart valves

The cardiac cycle is divided into two distinct periods, systole and diastole. Systole is the contracting period of the cardiac cycle, where blood is pumped out of the ventricles and into the pulmonary artery and aorta. Diastole is the resting period of the cardiac cycle, where the heart muscle relaxes and allows blood to flow from the atrium's and into the ventricles.

The pressures in the ventricle and aorta, as well as the ventricle volume, is shown in the Wigger diagram in Figure 2.1 for the cardiac cycle. Systole typically lasts approximately one third of the cardiac cycle and starts with the opening of the aortic valve, which opens completely in approximately 20 - 30 ms [8]. The maximum pressure drop across the heart valve during systole is small, in the region of a few mmHg, whereas the pressure difference during diastole is much higher at approximately 100 mmHg and 30 mmHg for the aortic valve and pulmonary valve respectively [8].

During the normal functioning of the cardiac cycle in the human body, the tissues of the large arteries, such as the aorta, common carotid, subclavian and pulmonary artery expand during systole. The expansion of the arteries absorb energy from the pulsatile flow by deforming, which manifests itself by damping out the pressure fluctuations during the cardiac cycle. This effect of the expansion of the arteries during systole is known as the Windkessel effect [15]. During diastole, the energy absorbed by the tissue is released as the tissues return to their original position.

Designing an artificial trileaflet heart valve similar to that of a native heart valve offers the advantage of mimicking the flow profile and hemodynamic performance to that of a native heart valve [2]. During the opening of a valve, the blood accelerates rapidly to reach a maximum velocity. A maximum velocity during systole in a healthy adult is approximately 1.35 ± 0.35 m/s [8], whereas maximum velocities up to 3.7 m/s have been reported for a porcine heart valve [2]. A jet of fluid emerges from the centre of the heart valve during opening. Once the blood reaches a maximum velocity, the blood begins to decelerate at a slower rate than the initial acceleration [8]. The deceleration of blood through the valve generates a negative pressure gradient across the valve, causing reverse

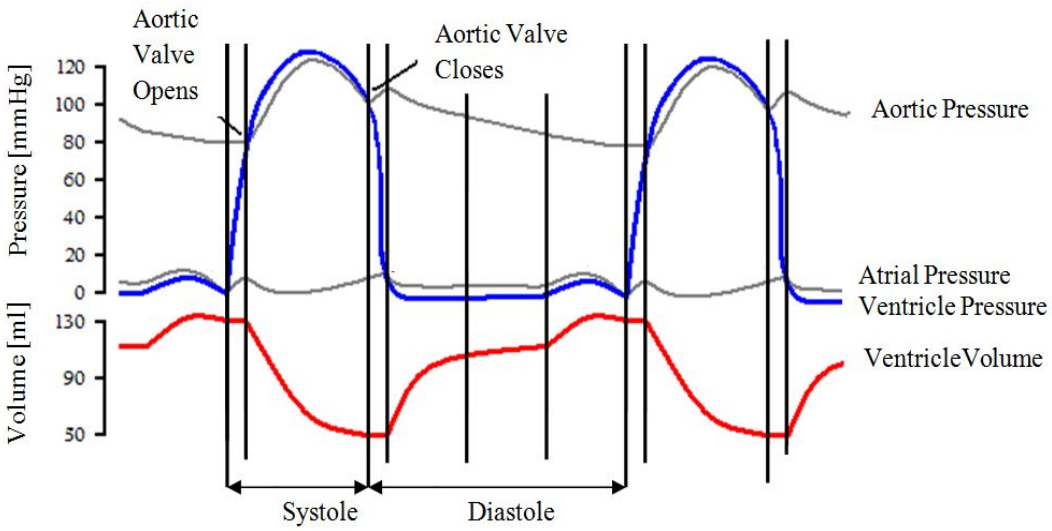

Figure 2.1: Wigger diagram showing the various pressures and ventricle volume in the heart during the cardiac cycle (adapted from [17])

flow near the wall of the aorta in the sinus region [8; 2]. The vortices created in the sinus region is shown in Figure 2.2 by the vortex and vortex rings labels. High shear stresses are therefore present at the interface between the central jet and recirculation flow due to the velocity gradient [8; 2]. The vortices developed in these sinus regions aide in closing the aortic valve (highlighted red) quickly to prevent regurgitation [8; 16].

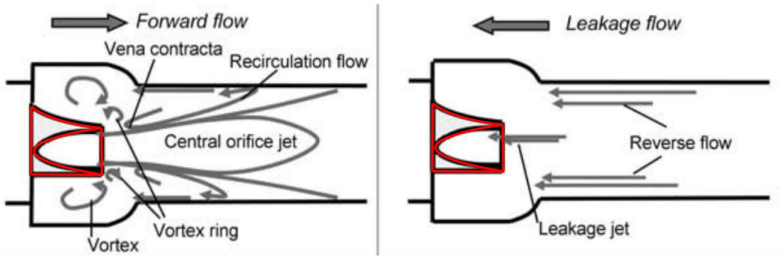

Figure 2.2: Flow profile through a trileaflet heart valve during systole (left) and diastole (right) (adapted from [2])

2.2 Pulse duplication

2.2.1 Background

Pulse duplication provides a means of artificially mimicking the functioning of a human heart in order to experimentally evaluate heart valves or other cardiovascular systems [18]. The *in vitro* hydrodynamic testing of a valve can be determined through pulse duplication before progressing to *in vivo* testing. Experimental pulse duplication testing is performed using a cardiac pulse duplicator (CPD) and are typically divided into two fluid

regions (Figure 2.3): an actuator and a mock systemic circulatory loop. The circulatory system is further divided into:

- a self filling atrial chamber
- a ventricle sac
- an aortic chamber
- a systemic resistance circuit

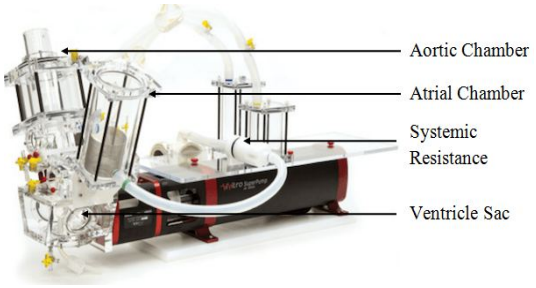

Figure 2.3: Vivitro pulse duplicator showing the various regions of a cardiac pulse duplicator (adapted from [19])

A linear actuator pump moves backwards and forwards, compressing and decompressing the ventricle sac, pumping fluid into and out of the ventricle sac thereby mimicking the functioning of a human heart. A saline-glycerol solution is used within the mock systemic circulatory loop to mimic the density and viscosity of blood. The solution is pumped out of the ventricle sac through the aortic valve during systole, and the ventricle sac is then filled with fluid through the mitral valve during diastole.

Numerous studies have been performed on heart valves in CPD's [20; 21; 22; 23; 24]. Rodriguez [20] redesigned a custom built CPD in order to provide a flexible CPD system to test a variety of heart valves, from stented valves to trans-catheter valves. A custom designed control system was used to study the dynamics of a control heart valve, showing repeatability of the cycle-to-cycle variation results [20]. Yokoyama *et al.* [23] redesigned a CPD to allow for passive filling of the ventricle chamber to mimic the natural mechanics of the heart. Special attention to the Windkessel effects of the systemic, venous and pulmonary systems was incorporated, as well as ensuring similar pressure-volume relationship to a native heart [23]. Capulli *et al.* [22] used pulse duplication to assess the *in vitro* performance of a biohybrid scaffold heart valve before moving onto an *in vivo* ovine model for heart valve deployment. the *in vitro* performance evaluation is critical in ensuring that a potentially fatal valve is not implanted until the performance is satisfactory.

As the design and setup of CPD systems is critical to obtain objectively comparable results between heart valves, a study published by the U.S. Food and Drug Administration (FDA), along with Medtronic Inc. and Edwards Lifesciences showed that obtaining repeatable and reproducible results is extremely difficult [21]. Two valves were circulated between six independent testing centers, and the pressure drop and regurgitation were reported to vary significantly between centres [21]. The FDA study concluded that testing of new heart valve designs should be completed simultaneously with commercially available valves to ensure that the newly designed valve is operating adequately.

There are several performance indicators that describe the function of a normal functioning heart valve. The ideal heart valve should have a minimal pressure drop during

systole, minimal regurgitation, minimal turbulence and shear stress, and aim to reduce the number of stagnant flow regions [8]. Numerous heart valves have been designed to meet these requirements as best they can, however there is still no perfect heart valve design. In order to satisfy these requirements, the following performance indicators are scrutinised for new designs of heart valves.

2.2.2 Pressure drop

The pressure drop, $\triangle P$, across a heart valve indicates the efficiency of the valve to allow blood to flow through the heart valve [8]. A high pressure drop requires a higher systolic pressure, thereby increasing the stress on the heart muscle and increasing oxygen consumption in the heart muscle tissue [8]. The magnitude of the pressure drop indicates the extent to which the heart valve impedes on blood flow, which negatively impacts on the heart valves hemodynamic performance.

Following ISO 5840:2015, the pressure drop across a valve during systole, also referred to as the trans-valvular pressure drop, is defined over the period when the pressure upstream of the heart valve (ventricle pressure) is larger than the downstream pressure (aortic pressure or pulmonary pressure for the systemic and pulmonary circulations respectively) [25]. The pressure drop is calculated as the average pressure during the described time period. The pressure drop period is shown in Figure 2.4, where line 1 is the aortic/pulmonary pressure, line 2 is the ventricular pressure and line 3 is the volumetric flow rate.

$$\Delta P = \frac{1}{N}\sum_{i=1}^{N}(P_{ventricle} - P_{aortic}) \tag{2.1}$$

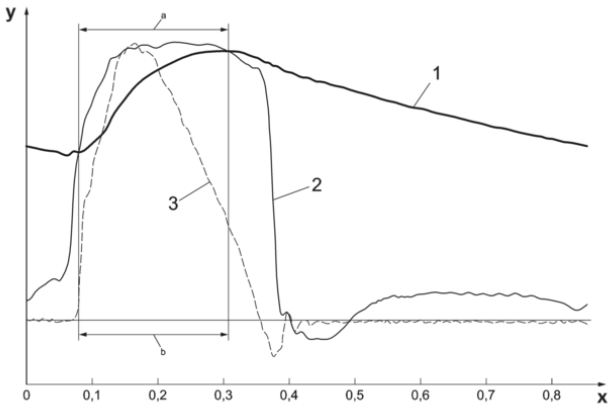

Figure 2.4: Positive trans-valvular pressure drop and volumetric flow rates to determine Q_{rms}. 1 - aortic/pulmonary pressure, 2 - ventricle pressure, 3 - volumetric flow rate (adapted from [25])

2.2.3 Effective orifice area

The effective orifice area (EOA) is a measure of the ability of a heart valve to allow fluid to flow through the orifice, and is defined in ISO 5840:2015 [25] as

$$EOA_{(cm^2)} = \frac{Q_{rms}}{51.6\sqrt{\frac{\triangle P}{\rho}}} \tag{2.2}$$

where $\triangle P$ is the average trans-valvular pressure drop, Q_{rms} is the root mean square of the volumetric flow rate during the same period as the positive trans-valvular pressure drop (Section 2.2.2), and ρ is the fluid density. The Q_{rms} is calculated using the trapezoidal numerical integration technique on the volumetric flow rate graph, indicated in Figure 2.4, and is defined in International Organisation of Standards [25]

$$Q_{rms} = \sqrt{\frac{\int_{t_1}^{t_2} q_v(t)^2 dt}{t_2 - t_1}} \tag{2.3}$$

where q_v is the instantaneous volumetric flow rate, t_2 and t_1 is the time period during the positive trans-valvular pressure drop. When designing a heart valve, increasing the EOA is desirable. As the EOA increases, the pressure drop required to ensure a constant volumetric flow rate decreases, reducing the strain on the heart. The EOA is also dependant on the geometric area of the valve, therefore the EOA can be normalised by dividing the EOA by the valve sewing area, called the performance index [8].

2.2.4 Regurgitation

Regurgitation is the reverse flow of blood through the heart valve and is divided into two different periods: closing volume and leakage volume. The closing volume is the volume of blood that flows back through the open heart valve while it is closing, while the leakage volume is the volume of blood that leaks through a closed heart valve during diastole. The regurgitation volume (RV), which is the sum of the closing and leakage volumes, is shown in Figure 2.5, where the closing volume is shown as shaded area marked 1 and the leakage volume is shown as the shaded area marked 2.

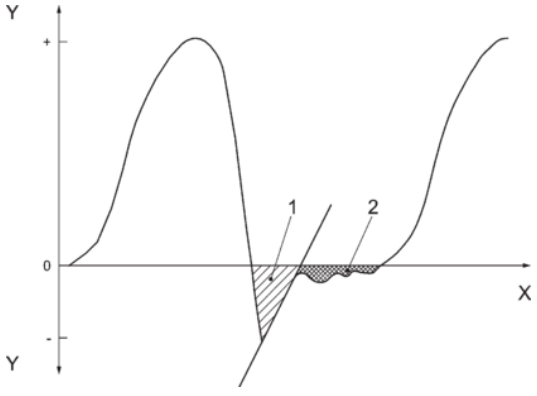

Figure 2.5: Volumetric flow rate graph during the cardiac cylce showing the closing and leakage volume regions during one cardiac cycle (adapted from [25])

The minimum requirements according to ISO 5840:2015 for the EOA and percentage regurgitation per valve size is shown Table 2.1. The RV is determined by taking the integral of the volumetric flow rate

$$RV = \int_{t_1}^{t_2} q_v(t)dt \tag{2.4}$$

where t_1 is the time where the volumetric flow rate becomes negative and t_2 is the time at the end of diastole. The percentage RV is then determined by calculating the RV as a percentage of the stroke volume, where the stroke volume is the total volume of fluid expelled by the ventricle during systole.

$$PercentageRV = \frac{RV}{StrokeVolume} * 100\% \tag{2.5}$$

Table 2.1: Minimum ISO performance requirements for an aortic and mitral heart valve of various sizes [25]

Position	Aortic							Mitral			
Valve size (TAD, mm)	19	21	23	25	27	29	31	25	27	29	31
EOA (cm^2)	≥ 0.70	≥ 0.85	≥ 1.00	≥ 1.20	≥ 1.40	≥ 1.60	≥ 1.80	≥ 1.20	≥ 1.40	≥ 1.60	≥ 1.80
Percentage RV (%)	≤ 10	≤ 10	≤ 10	≤ 15	≤ 15	≤ 20	≤ 20	≤ 15	≤ 15	≤ 20	≤ 20

2.3 Particle imaging velocimetry

2.3.1 Background

Particle imaging velocimetry (PIV) is a technique used for fluid flow visualisation where small, neutrally bouyant particles are mixed with a fluid and are illuminated with a laser sheet. A camera captures two consecutive images with which the velocities of the particles can be determined [26]. Combining PIV with pulse duplication offers an advantage of being able to determine the performance of a heart valve according to [25] whilst visually inspecting the velocity vector fields through the heart valve itself. The setup of a PIV system with the laser, camera and imaging area is shown in Figure 2.6.

Various imaging techniques apart from the standard PIV techniques are available, with the most common being tomographic PIV, stereoscopic PIV and laser doppler anemometry. Stereoscopic PIV makes use of two cameras with different viewing angles to the laser sheet plane in order to determine the movement of the particles in and out of plane [26]. This enables the post-processing software to not only determine the fluid velocity in the x and y direction in the plane of the laser sheet (Figure 2.6), but also the velocity of the particles in and out of the plane in the z direction (direction out of the page in Figure 2.6) [27]. Tomographic PIV and laser doppler anemometry take this one step further by determining the velocity in the x, y and z direction in the entire fluid chamber, giving a complete three dimensional field of view. PIV provides an advantage due to the length of time required to perform laser doppler anemometry [28], as PIV allows for the instantaneous velocity field across a heart valve whereas laser doppler anemometry requires

point by point measurements [29; 30].

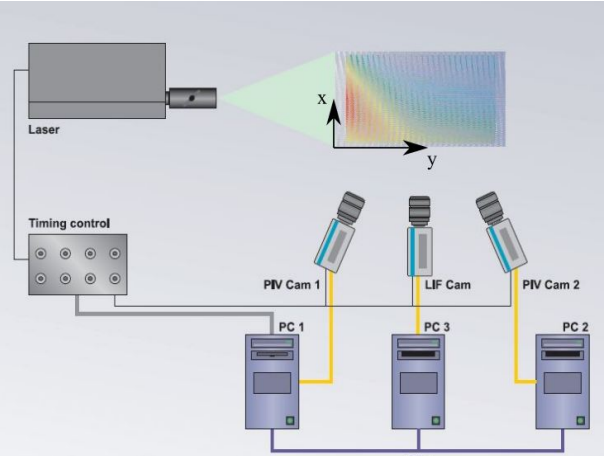

Figure 2.6: PIV setup displaying the laser, camera's and imaging region (adapted from [31])

PIV has been performed by many researchers to evaluate the performance of a heart valve [28; 30; 32; 33; 34], as well as to compare the PIV experiments with numerical simulations [35; 36; 37]. Toninato *et al.* [34] used PIV to determine the effect that the vortical structures in the sinus of Valsalva have on the dynamics of heart valves. Ducci *et al.* [38] extended this work to evaluate the flow field in the sinus region of a native heart valve with that of a transcatheter heart valve, where the transcatheter heart valve severely impacted the functioning of the sinus region by introducing large stagnant regions in the sinus region, and thereby potentially increasing the thrombogenic potential of the heart valve.

Stereoscopic PIV was performed by [39; 40; 41; 42]. Leo *et al.* [42] used stereoscopic PIV to evaluate three polymeric heart valves. The tests were performed at several heights in order to develop a semi 3D visualisation of the flow domain. The leakage of fluid through the valves was examined during diastole, where reverse flow was found in the sinus region of approximately 0.02 m/s, however a much higher leakage flow jet was found in the center of the valve up to 1.63 m/s [42]. High shear stresses were recorded in the leakage jet, indicating that diastole has an important role to play in heart valve hemodynamics [42]. Tomographic PIV was performed by Hasler *et al.* [43] for a bioprosthetic heart valve inserted in a transparent silicone model, where two cameras were setup to record images from four different angles. Hasler *et al.* [43] reported only on the velocity field of the flow and the resulting vortical structures and not on the shear stresses.

2.3.2 Shear stress

The flow patterns, velocity vector field and subsequently the shear stress, are important factors in determining the longevity of a heart valve. Areas of stagnant flow, flow separation and high shear stress could lead to thrombus formation, hemolysis (damage of red

blood cells (RBCs)) and platelet activation [8; 2]. PIV has been successfully used to determine the shear stress threshold at which hemolysis and platelet activation will occur [36; 44; 45].

The value of the shear stress required for the onset of hemolysis and platelet activation varies in literature and seems to be dependent on the method used to determine its value. The viscous shear stress (VSS) threshold for hemolysis was reported to be between 150 Pa and 400 Pa in Ge *et al.* [36], 100 Pa by Sutera *et al.* [46], or a turbulent shear stress of 800 Pa in Lu *et al.* [47] and 340 Pa in Yen *et al.* [45]. Yen *et al.* [45] measured the hemolysis threshold using the turbulent viscous shear stress (TVSS), as described in Sheng *et al.* [48] and Li *et al.* [44], and found a TVSS threshold of 60 Pa and a major Reynolds shear stress (RSS_{maj}) threshold of 517 Pa. A summary of the hemolysis threshold limits performed by multiple researchers are summarised in Yen *et al.* [45]. The threshold for platelet activation is reported to be of an order of magnitude smaller, thereby indicating that platelet activation is more prevalent than hemolysis. VSS as low as 10 Pa by Ge *et al.* [36] have been reported in literature to cause platelet activation.

It is widely accepted that turbulence is a significant contributer to RBC and platelet damage. When combining the effects of shear stress and turbulence on the threshold limits, confusion has often arisen due to the various ways the shear stress can be determined in turbulent flow [36]. The Reynolds shear stress (RSS) and RSS_{maj} have been used to determine the shear stress in both experimental and numerical simulations, and could incorrectly be evaluated against other works where the VSS were calculated. The VSS can be considered to be the actual stress experienced by the RBCs and platelets, whereas the RSS and RSS_{maj} is a statistical, time averaged value that has no physical interpretation [36]. In laminar flows, the VSS term found in the Navier-Stokes equation is defined as [36; 44]

$$\tau_{ij} = \mu\left(\frac{\partial u_i}{\partial x_j} + \frac{\partial u_j}{\partial x_i}\right) \tag{2.6}$$

where the i and j subscripts refer to the x and y direction of the flow. The VSS is dependant only on the instantaneous velocity gradients and the fluid viscosity. The RSS is only found once Reynolds decomposition is applied to the Navier-Stokes equations which are defined as [49]

$$\rho\frac{\partial \overline{u}_i}{\partial t} + \rho\overline{u}_j\frac{\partial \overline{u}_i}{\partial y} = \rho\overline{f}_i - \frac{\partial}{\partial x_j}\left[-\overline{P}\delta_{ij} + 2\mu\overline{S}_{ij} - \rho\overline{u_i' u_j'}\right] \tag{2.7}$$

The Reynolds stress tensor, $\tau_{ij} = \rho\overline{u_i' u_j'}$ is determined from the Reynolds decomposition. The variables u_i' and u_j' are the fluctuating velocity components and the variables $\overline{u}_i$ and $\overline{u}_j$ are the mean components in the x and y direction of the velocity field respectively and are defined as

$$\overline{u}_i = \frac{1}{N}\sum_{i=1}^{N} u_i \qquad \overline{u}_j = \frac{1}{N}\sum_{j=1}^{N} u_j \tag{2.8}$$

$$u_i' = u_i - \overline{u}_i \qquad u_j' = u_j - \overline{u}_j \tag{2.9}$$

Numerous studies have been performed where the RSS was used as a measure for determining the onset of hemolysis or platelet activation [36; 33; 50; 42], whereas Yen *et al.* [45]; Falahatpisheh and Kheradvar [32]; Raghav *et al.* [51] used the RSS_{maj} value, as the standard RSS formula is not invariant under coordinate rotation. The RSS_{maj} is defined as

$$RSS_{maj} = \rho \sqrt{\left(\frac{\overline{u_i' u_i'} - \overline{u_j' u_j'}}{2} \right)^2 + \left(\overline{u_i' u_j'} \right)^2} \tag{2.10}$$

Ge *et al.* [36] introduced a three part decomposition of the velocity, where the instantaneous velocity is divided into the mean velocity, cycle-to-cycle velocity and turbulent velocity fluctuation defined as

$$u_i = \overline{u}_i + \widehat{u}_i + u_i^{'} \tag{2.11}$$

Due to the dynamic conditions of pulsatile flow in a CPD, the three part decomposition may be incorrect [36]. When using two part decomposition during early opening of the valve when the flow is laminar, the fluctuating term is non-zero due to the cycle-to-cycle variation [36]. However at peak flow, when the flow is turbulent, it is impossible to determine whether the fluctuation is due to cycle-to-cycle variation or turbulent fluctuations [36].

In turbulent flows, the damage incurred by the RBCs is a direct cause of the smallest vortices present in the flow [45]. The RSS that is determined from the Reynolds time-averaged Navier-Stokes equations is not considered a physical force and is not representative of the physical shear stress experienced by the RBCs and platelets, causing hemolysis and platelet acitvation [44; 36]. Even though the RSS is not considered a physical force, Grigioni *et al.* [52] found that there is an increase in hemolysis for an increase in RSS.

Not only is the RSS not representative of the real shear stress, it is also dependent on the averaging method used such as time-averaging, ensemble-averaging or phase-averaging [36]. Alternatively, spatial-averaging, referred to as filtering in the Large Eddy Simulation (LES), can be employed, which introduces the subgrid scale (SGS) stress [36; 45]. Ge *et al.* [36] argues that modelling the TVSS would also apply a filtering technique, in this case spatial filtering, however Yen *et al.* [45] and Sheng *et al.* [48] argue that using a LES based spatial filtering would be appropriate for calculation of the shear stress from PIV. This is due to the method in which LES resolves for the large scale turbulent eddies that are larger than the grid size, and models the small scale eddies smaller than the grid size. This principle can be extended from computational fluid dynamics to PIV where the PIV interrogation windows size is similar to the computational grid size.

The turbulent kinetic energy present in turbulent flows is present in the large scale eddies and is transferred down to the smaller scale eddies, where the energy is dissipated in the viscous sub-range [49]. Situated between these two scales is the inertial sub-scale range where the energy in the large scale is transferred to the small scale, and as such, no change in the turbulent kinetic energy occurs. This principal is used in the large eddy PIV

analysis, where the energy in the inertial sub-range is determined from the PIV velocity field, and the same amount of energy is transferred down to the small scale eddies. This requires that the spatial resolution of the PIV interrogation windows be situated in the inertial sub-range in order to be valid [53]. By using the large eddy PIV method, the velocity field does not need to be resolved down to the Kolmogorov scale in order to determine the shear stress in the fluid on the micro scale [48]. The instantaneous velocity is given as

$$u_i = \overline{U}_i + \widehat{u}_i \qquad u_j = \overline{U}_j + \widehat{u}_j \tag{2.12}$$

where $\overline{U}$ is the resolved velocity and $\widehat{u}$ is the unresolved-scale velocity [48]. By filtering the Navier-Stokes equations, the LES equations are obtained as follows

$$\frac{\partial \overline{U}_i}{\partial t} + \frac{\partial (\overline{U}_i)\overline{U}_j}{\partial y} = \frac{\partial \overline{P}}{\partial x} + \nu \frac{\partial^2 \overline{U}_i}{\partial y^2} - \frac{\partial \tau_{ij}}{\partial y} \tag{2.13}$$

where the sub-grid scale (SGS) stress is given as

$$\tau_{ij} = \overline{U_i U_j} - \overline{U_i}\ \overline{U_j} \tag{2.14}$$

The LES Navier-Stokes equation in the x is then multiplied by $\overline{U_i}$ and contracted as described in Sheng *et al.* [48]

$$\frac{\partial \frac{1}{2}\overline{U}_i \overline{U}_i}{\partial t} + \overline{U}_j \frac{\partial \frac{1}{2}\overline{U}_i \overline{U}_i}{\partial y} = \frac{\partial}{\partial y}\left(-\overline{P}\ \overline{U}_j + \nu \frac{\partial \frac{1}{2}\overline{U}_i \overline{U}_i}{\partial y} - \tau_{ij}\overline{U}_i\right) - \nu \frac{\partial \overline{U}_i}{\partial y}\frac{\partial \overline{U}_i}{\partial y} + 2\tau_{ij}\overline{S_{ij}} \tag{2.15}$$

where $\overline{S_{ij}} = \frac{1}{2}(\frac{\partial \overline{U}_i}{\partial x_i} + \frac{\partial \overline{U}_i}{\partial x_j})$ is the resolved scale strain rate tensor [48]. The term $2\tau_{ij}\bar{S}_{ij}$ is the turbulent eddy dissipation and models the kinetic energy transferred down to the small scale eddies. As the fundamental assumption is that the energy transferred from the turbulent kinetic energy in the integral scale is equal to the dissipated energy in the micro scales [44], the turbulence dissipation rate can be determined by

$$\varepsilon = 2\tau_{ij}\overline{S_{ij}} \tag{2.16}$$

The resolved strain rate tensor can be calculated directly from the velocity field. To finalise the TVSS model, a SGS model is now required in order to determine τ_{ij}. There are a number of models, where Sheng *et al.* [48] provide a summary of the applicability of the SGS models based on PIV data. The most common LES models are the Smagorinsky model, used in Sheng *et al.* [48] and Yen *et al.* [45], similarity model, gradient model and the dynamic model, although the similarity and dynamic models are not applicable to experimental large eddy PIV [48]. For the Smagorinsky model, the eddy viscosity is modelled as in [48; 44; 53]

$$\tau_{ij} = -C_s^2 \Delta^2 |\overline{S}| \overline{S_{ij}} \tag{2.17}$$

where the Smagorinsky constant $C_s = 0.17$, Δ is the distance between two measurement points and $|\overline{S}| = \sqrt{2\overline{S_{ij}S_{ij}}}$. The eddy dissipation rate in Equation 2.16 is then determined

and substituted into the TVSS formula

$$\tau_v = \sqrt{\frac{1}{2}\rho\mu\varepsilon} \tag{2.18}$$

All of the above methods for determining the shear stress, VSS, RSS, RSS_{maj} and TVSS have been applied to PIV for heart valves, however all four metrics have not been compared for determining hemolysis and platelet activation of a trileaflet heart valve using a single data set to the best of the authors knowledge. Even though TVSS model may provide additional information about the shear stress on the RBCs and platelets, very few results were found in literature where the TVSS model was applied to heart valves.

2.4 Numerical simulation

2.4.1 Background

Computational fluid dynamics (CFD) has previously been used to model the flow of blood through heart valves. Initially, two-dimensional (2D) CFD simulations were performed to evaluate prosthetic heart valves. In later years, computer resources improved to the point where three-dimensional (3D) CFD computations could be performed [36], however simplifications such as symmetric flow were still assumed [54; 55]. It was found that the flow directly downstream of a heart valve is highly sensitive to the grid resolution, and that for Re = 1200, the flow field is fully 3D, shedding some scepticism on work done with higher Re numbers and symmetry assumptions [56]. More recently, full 3D simulations of heart valves, with and without moving domain boundaries, have been performed by numerous researchers [57; 58; 59; 60; 61; 62]. A full CFD evaluation was conducted for both laminar and turbulent flow conditions, as well as using a two phase lagrangian formulation to model platelet damage over time by Alemu and Bluestein [60]. In studying fully 3D results, Prakash and Ethier [63] found that the wall shear stress (WSS) is particularly sensitive to mesh refinement and a higher grid resolution is required for shear stress independence than that for the velocity field. Turbulence modelling through heart valves is also a non-trivial activity as the flow typically begins laminar and transitions to turbulent flow. LES models are currently the most promising method for predicting turbulence and re-laminarisation in heart valve simulations [8], however full LES simulations are still limited by computational resources.

In order to fully model the functioning of heart valves, the complex fluid-structure interaction (FSI) between the fluid flow and the heart valve leaflets must be accounted for. Various techniques have been developed to account for this interaction, where each has their own advantages and disadvantages. For mechanical heart valves, the use of rigid bodies combined with CFD can be used to model the opening and closing of the heart valve leaflets. This has been applied by Nobili and Morbiducci [57] and Ge and Sotiropoulus [59], by allowing the leaflets to only rotate around a fixed point, where the forces determining the movement are calculated from the pressures and shear forces on the leaflet walls. This method is not suitable for tissue and polymer based heart valves, where the movement of the leaflets is complex and cannot be determined before the simulation or with rigid bodies. The complex motion of the leaflets can be determined

by coupling a fluid solver and a structural solver to compute the fluid flow and structural deformation simultaneously.

2.4.2 Fluid-structure interaction

FSI has been used in many applications, including but not limited to simulating the flow through heart valves [64; 65; 62; 66; 67; 68], aero-elasticity and aerodynamics [69; 70] and airflow through parachutes [71]. Due to the complex interaction of the fluid and structural domains, the development of computational methods than can account for the complexities of FSI has been developed by researchers and engineers around the world. The most widely used techniques for simulating the leaflet motion of heart valves are the Arbitrary Lagrangian-Eulerian (ALE) method and the ficticious domain or Immersed Boundary (IB) method [29].

2.4.2.1 Arbitrary-Lagrangian Eulerian

The ALE method has been around since the 1960's and has been used in the field of FSI to overcome the disadvantages of pure Lagrangian and Eulerian formulations [72]. ALE is a boundary fitted method where the solid domain is modelled in a Lagrangian formulation while the fluid domain is modelled in a Eulerian formulation [73]. The ALE method has been used by [67; 62] to model the movement of flexible heart valves, however the majority of researchers make use of an IB method to account for the extreme deformation of the heart valve leaflets. The benefit of the ALE method over the IB method is the ability to account for accurate boundary layer flows, however severe mesh distortion makes it difficult to perform ALE based simulations of the heart valves themselves. Hsu *et al.* [74] used a hybrid IB-ALE method, where the IB method was used for the heart valve leaflet movement, and the ALE method was used to model the arterial wall, where much smaller deformations are present. Bavo *et al.* [62] compared the ALE and IB method in 2D and 3D for a tissue heart valve using Abaqus/Explicit version 12.0 (Dassault Systemes, Providence, RI, USA). The ALE method required far fewer mesh elements than the IB method, however in 3D the ALE simulation diverged after a simulation time of 24 ms due to the generation of inverted elements. This highlights the added difficulty of handling large mesh deformations during heart valve opening and closing.

Hof [75] modelled the opening of a simple tissue and bileaflet mechanical heart valve using the software Unicorn [76], a distribution of the FEniCS project [77] using a monolithic ALE method. Wu *et al.* [67] simulated a percutaneous heart valve using the ALE method with ANSYS LS-DYNA 971 release 7.0 (LSTC, Livermore CA, USA and ANSYS, Inc., Canonsburg, PA, USA), with the intent on predicting the fatigue life of the heart valve. Dumont *et al.* [78] used a dynamic mesh method in ANSYS FLUENT®(ANSYS, Inc., Canonsburg, PA, USA) combined with an FSI coupler to model the thrombogenic performance of a bileaflet mechanical heart valve, as well as Mirkhani *et al.* [79] who simulated the On-X bileaflet mechanical valve using the ALE method in ANSYS FLUENT®14.1 (ANSYS, Inc., Canonsburg, PA, USA). The majority of heart valve models using the ALE method in literature is restricted to mechanical heart valves.

2.4.2.2 Immersed boundary method

The IB method was developed by Peskin in order to simulate cardiac mechanics [80; 81]. The IB method does not require a body fitted mesh as the solid is artificially accounted for in the discretised Navier-Stokes equations. Figure 2.7 shows the difference between a body fitted and IB mesh. An IB method using the fictitious domain method was developed by De Hart *et al.* [64]. A problem found in typical FSI studies of heart valves is the accurate measurement of the WSS on the valve leaflets, especially at higher *Re* numbers. This was considered a disadvantage of the IB method, and many models have recently been implemented in IB methods to improve near wall accuracy. A sharp interface IB method was implemented by Kang [82] based on the work done by Ge and Sotiropoulus [59], and openFOAM currently has an IB method to determine the IB wall cell value by using a least squares method using an extended stencil method [83]. The sharp interface method applied wall functions for the accurate determination of the wall shear stress under higher *Re* numbers. This method was applied for both mechanical heart valves by Ge and Sotiropoulus [59], and for bicuspid and tricuspid heart valves by Gilmanov and Sotiropoulus [58].

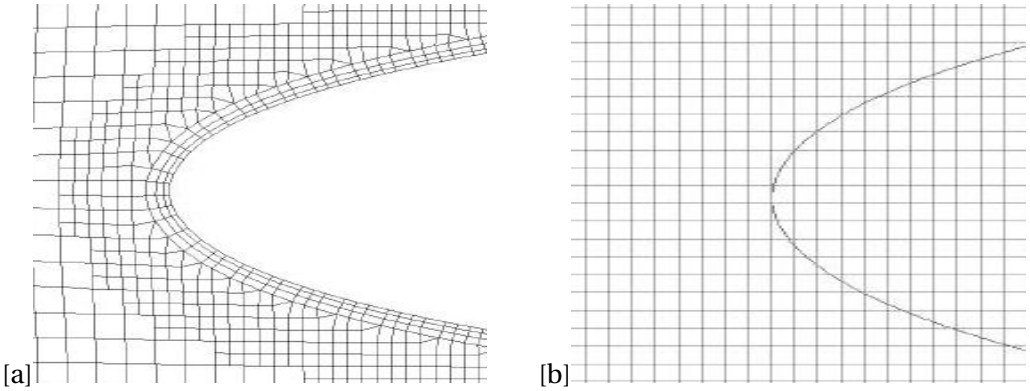

Figure 2.7: Comparison of a [a] body fitted mesh and [b] an immersed boundary mesh (adapted from [83])

The use of IB methods has recently been further extended to model cardiovascular mechanics, where the immersogeometric method was applied to patient specific models of an aortic outflow tract with patient specific geometries [84]. An IB method was implemented in foam-extend using a discrete forcing approach with wall functions to obtain higher accuracy at higher *Re* numbers [83; 85]. The validation results showed that a high level of accuracy can be attained for lower *Re* numbers ($Re = 3000$), however inaccuracies can occur for very high *Re* numbers ($Re = 8\text{x}10^6$) [83]. A more thorough decription of various IB methods can be found in Sotiropoulus and Yang [86].

2.4.3 Coupling strategies

When performing FSI simulations, two methods are used to couple the fluid and solid domains: a monolithic or partitioned method [87; 88]. Using a monolithic method, a global system of equations is described for both the fluid and solid and all equations are solved simultaneously [89]. Using a partitioned method, the system of equations for the

fluid and solid are formulated independently and coupled along a common interface [88]. The benefit of the partitioned method is that independent software designed for a specific task can be used as black-boxes, whereas the monolithic method must be formulated for the problem at hand [87]. Different software exists to couple two black-box solvers together in a partitioned manner, and are summarised by Uekermann [90] and Gatzhammer [87].

Gatzhammer [87] summarised the work done by Förster *et al.* [91], Degroote *et al.* [92] and Causin *et al.* [93] on the instabilities of the added mass effect when using an implicit, partitioned approach. A summary of the parameters that increase instabilities with the added mass effect are when [87]:

1. the solid to fluid density ratio is decreased
2. the stiffness of the structure, E, is decreased
3. the viscosity of the fluid is increased
4. the time step is increased for explicitly coupled schemes
5. the time step is decreased for implicitly coupled schemes
6. the aspect ratio of the FSI interface is increased

In "*explicit*" coupling, also referred to as one-way coupling or weak coupling, the fluid and solid domains are only solved a fixed number of times for every timestep [87], typically once for each domain. In "*implicit*" coupling, also referred to as two-way coupling or strong coupling, each domain is solved multiple times and the interface information is transferred until convergence is reached for both domains. The under-relaxed implicit coupling iterations may be able to cope with small instabilities, however Aitken and Newton based methods are better for large instabilities but are harder to implement in a coupler [87]. For the sake of brevity, only Aitken under-relaxation and Quasi-Newton based methods are discussed.

2.4.3.1 Aitken relaxation coupling

In Aitken relaxation, the under-relaxation factor continually changes in order to increase stability and decrease the number of iterations per time step required for convergence. The new interface value is determined from

$$\mathbf{x}^{k+1} = \omega^k \cdot \mathbf{x}^k + \left(1 - \omega^k\right) \cdot \mathbf{x}^k \tag{2.19}$$

where ω^k is the relaxation factor. Aitken relaxation introduces a varying relaxation factor by

$$\omega^k = -\omega^{k-1} \frac{\left(\mathbf{R}^{k-1}\right)^T \left(\mathbf{R}^k - \mathbf{R}^{k-1}\right)}{\|\mathbf{R}^k - \mathbf{R}^{k-1}\|_2^2} \tag{2.20}$$

where $\mathbf{R}^k = \tilde{\mathbf{x}}^k - \mathbf{x}^k$ is the residual. The constantly changing relaxation factor has been shown to speed up convergence [90; 94].

2.4.3.2 Quasi-Newton coupling

The solving of Quasi-Newton based schemes is more complex and harder to implement than Aitken relaxation, and the reader is referred to Uekermann [90], Bogaers [88] and Gatzhammer [87] for the implementation of various Quasi-Newton schemes. The Quasi-Newton algorithm used in this study is the **I**nterface **Q**uasi-**N**ewton with approximation of the **I**nverse of the interface Jacobian matrix by **L**east **S**quares (IQN-ILS) scheme and is shown in Algorithm 1. The structural coupling results **s** and the output residual of the interface **r** is defined in Gatzhammer [87] as

$$\Delta \mathbf{r}_k = \mathbf{r}_{k+1} - \mathbf{r}_k \tag{2.21}$$

$$\Delta \mathbf{s}_k = \mathbf{s}_{k+1} - \mathbf{s}_k \tag{2.22}$$

The deltas above are used to construct matrices of the changes of the intermediate solver outputs and the residuals of the solver outputs

$$\mathbf{V}_k = \left(\mathbf{r}_k, \mathbf{r}_{k-1}, ..., \mathbf{r}_1, \mathbf{V}^{n-1}, ..., \mathbf{V}^{n-j}\right) \tag{2.23}$$

$$\mathbf{W}_k = \left(\mathbf{s}_k, \mathbf{s}_{k-1}, ..., \mathbf{s}_1, \mathbf{W}^{n-1}, ..., \mathbf{W}^{n-j}\right) \tag{2.24}$$

The subscripts of Equations 2.23 and 2.24 above denote the iterations within one time step, whereas the superscript denotes the previous time steps iterations. The inclusion of previous time steps iterations improves the performance of the IQN-ILS method [88; 87]. The IQN-ILS uses a least squares method to solve for a linear combination of the residual deltas according to [87] and [88]

$$\Delta \mathbf{r} = \mathbf{V}_k \lambda \tag{2.25}$$

To determine a new residual that is zero, the least squares method is used to solve for

$$\underset{\lambda}{\operatorname{argmin}} \| \Delta \mathbf{r} - \mathbf{V}_k \lambda \| \tag{2.26}$$

The IQN-ILS method enables the addition and removal of columns from $\mathbf{V}_k$ and $\mathbf{W}_k$, which is especially important when columns from previous time steps are reused to increase the performance of the IQN-ILS method [88]. The coefficients λ are then used to determine the $\Delta\tilde{\mathbf{s}}$ by

$$\Delta \tilde{\mathbf{s}} = \mathbf{W}_k \lambda \tag{2.27}$$

Determining the inverse of the interface Jacobian, the strength of the IQN-ILS method, is done by setting

$$\Delta \mathbf{r} = \Delta \tilde{\mathbf{s}} - \Delta \mathbf{s} \tag{2.28}$$

where the change in the interface displacements is determined as

$$\Delta \mathbf{s} = -\mathbf{J}_R \left(\mathbf{s}_k\right)^{-1} \mathbf{r}_{k+1} = \mathbf{W}_k \lambda + \mathbf{r}_{k+1} \tag{2.29}$$

Implementing column addition and deletion is critical to enhance the performance of the IQN-ILS method, however it is impossible to know how many time steps should

be reused to achieve optimal FSI coupling [88]. The total number of columns and time steps can be set within the preCICE coupling adapter and is set arbitrarily at the start of the simulation.

Algorithm 1 IQN-ILS Algorithm (adapted from[87])

procedure FROM KNOWN VALUES OF $\overline{U}$, $\overline{V}$ VELOCITY VECTOR FIELDS
  $\tilde{\mathbf{s}}_1 = \mathbf{S} \cdot \mathbf{F}(s_0)$
  $\mathbf{r}_1 = \tilde{\mathbf{s}}_1 - \mathbf{s}_0$
  if $n = 0$ **then**
    $\mathbf{s}_{k+1} = (1-\omega)\mathbf{s}_k + \omega\tilde{\mathbf{s}}_{k+1}$
  else
    $\mathbf{s}_1 = \mathbf{s}_0 + \triangle\mathbf{s} = \mathbf{s}_0 + -\mathbf{J}_R(\mathbf{s}_k)^{-1}\mathbf{r}_{k+1}$
    k = 1
  while not converged
  $\tilde{\mathbf{s}}_{k+1} = \mathbf{S} \cdot \mathbf{F}(\mathbf{s}_k)$
  $\mathbf{r}_{k+1} = \tilde{\mathbf{s}}_{k+1} - \mathbf{s}_k$
  Update $\mathbf{V}_k$ and $\mathbf{W}_k$
  $\mathbf{s}_1 = \mathbf{s}_0 + \triangle\mathbf{s} = \mathbf{s}_0 + -\mathbf{J}_R(\mathbf{s}_k)^{-1}\mathbf{r}_{k+1}$
  $\mathbf{s}_{k+1} = \mathbf{s}_k + \Delta\mathbf{s}$
  $k = k+1$

2.4.4 Coupling procedure

The coupling procedure can vary between serial and parallel coupling. Figure 2.8 shows the various ways that coupling can occur for strongly coupled FSI simulations. Figure 2.8 (left) displays a simple serial coupling where the updated fluid domain results are mapped to the solid domain, and the solid domain is solved with the new mapped fluid solver information. Figure 2.8 (right) shows a parallel implementation where the fluid and solid domain are solved with the previous iteration results, and the updated results are fed to the coupler.

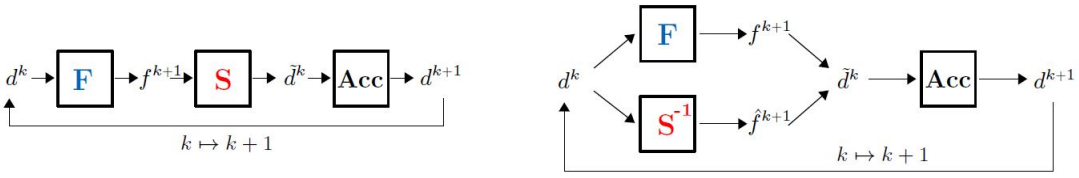

Figure 2.8: Visual comparison of a serial (left) vs parallel (right) coupling process (used with permission from [90])

2.4.5 Radial basis function mesh motion

When using the ALE method, the deformation of the structure influences the fluid domain. The deformation of the structure is accounted for by either moving the fluid mesh in an optimisation scheme to maintain the mesh quality, or through topology changes

by using a mesh motion solver to move the mesh. Methods exist to remesh the domain locally after a mesh distortion threshold is reached.The radial basis function (RBF) method can be used to solve for the mesh motion in the fluid domain for FSI simulations [88; 95; 96], as well as for solving of partial differential equations [97]. The RBF mesh motion solver method is defined as

$$\mathbf{S}(x) = \sum_{i=1}^{N_B} \boldsymbol{\alpha}_i \phi(\|x - x_i\|) + \sum_{k=0}^{M} \boldsymbol{\gamma}_k \boldsymbol{P}_k(x) \tag{2.30}$$

where $\mathbf{S}$ is the known deformation at the moving and fixed boundary points, N_B is the total number of boundary points, $\boldsymbol{\alpha}$ is the unknown coefficients of the RBF interpolation, $\phi(x)$ is the radial basis function, $\|x - x_i\|$ is the euclidean distance between two points and $\mathbf{P}_i$ is a polynomial of degree M. An additional constraint is placed on Equation 2.30 to avoid ill-conditioning of the system matrix

$$\sum_{j=1}^{N_B} \boldsymbol{\alpha}_j \mathbf{P}_j(x) = 0 \tag{2.31}$$

Equation 2.30 and 2.31 form a highly dense, linear matrix, where the accuracy increases for an increase in the number of RBF points, however the matrix often becomes ill-conditioned. The above equations can be reformulated into the following matrix equations:

$$\begin{bmatrix} \mathbf{M}_{AA} & \mathbf{P} \\ \mathbf{P}^T & 0 \end{bmatrix} \begin{bmatrix} \boldsymbol{\alpha} \\ \boldsymbol{\gamma} \end{bmatrix} = \begin{bmatrix} \mathbf{S} \\ 0 \end{bmatrix} \tag{2.32}$$

$$\mathbf{M}_{AA} = \begin{bmatrix} \phi_{A_1A_1} & \phi_{A_1A_2} & \cdots & \phi_{A_1A_N} \\ \phi_{A_2A_1} & \phi_{A_2A_2} & \cdots & \phi_{A_2A_N} \\ \vdots & \vdots & \ddots & \vdots \\ \phi_{A_NA_1} & \phi_{A_NA_2} & \cdots & \phi_{A_NA_N} \end{bmatrix}; \mathbf{P} = \begin{bmatrix} 1 & x_1 & y_1 & z_1 \\ 1 & x_1 & y_1 & z_1 \\ \vdots & \vdots & \vdots & \vdots \\ 1 & x_N & y_N & z_N \end{bmatrix}; \begin{bmatrix} \boldsymbol{\alpha} \\ \boldsymbol{\gamma} \end{bmatrix} = \begin{bmatrix} \alpha_1 \\ \vdots \\ \alpha_N \\ \gamma_0 \\ \vdots \\ \gamma_3 \end{bmatrix} \tag{2.33}$$

where $(\mathbf{M}_{AA})_{ij} = \phi(\|x_i - x_j\|)$, $\mathbf{P} = (1\ x_i\ y_i\ z_i)$, $\boldsymbol{\alpha} = (\alpha_1,...,\alpha_N)$, $\boldsymbol{\gamma} = (\gamma_0,...,\gamma_3)$ and $\mathbf{S}$ is the known values for the RBF interpolation in 3 spatial dimensions. The aim of the RBF interpolation is to solve for $\alpha_i \in \Re, i = 1,...,N$ and $\gamma_i \in \Re, i = 0,...,3$. Typical basis functions of $\mathbf{M}_{AA}$ are summarised in Table 2.2, where a is a constant and r is the local support basis functions radius. If the euclidean distance between points is larger than the specified radius r, $(\zeta > 1)$, the RBF interpolant becomes zero for local support basis functions. The choice of the constant a varies, therefore the thin-plate-splines basis function is recommended to reduce the number of variables affecting the accuracy, as well as offering global support. Once the weights α and γ have been solved, the movement of each interior point can be found by taking

$$\mathbf{S}(x_{N_I}) = \sum_{i=1}^{N_B} \boldsymbol{\alpha}_i \phi\left(\|x_{N_I} - x_i\|\right) + \sum_{k=1}^{M} \boldsymbol{\gamma}_k \mathbf{P}_k(x) \tag{2.34}$$

where x_{N_I} is the interior point to be determined and $\mathbf{S}\left(x_{N_I}\right)$ is the movement of an interior point.

Table 2.2: Common basis functions used for radial basis function interpolation ($\zeta = r/a$)

	Basis Function	Support Field
Gaussian	$\exp^{-(a\|x\|)^2}$	Global
Multiquadratics	$\sqrt{a^2+\|x\|^2}$	Global
Thin Plate Splines	$\|x\|^2 log(\|x\|)$	Global
Compact Polynomial C0	$(1-\zeta)^2$	Local
Compact Polynomial C2	$1-30\zeta^2-10\zeta^3+45\zeta^4-6\zeta^5-60\zeta^3 log\zeta$	Local
Compact Polynomial C6	$(1-\zeta)^8(32\zeta^3+25\zeta^2+8\zeta+1)$	Local

2.4.6 Data mapping

Mapping interface information between non-matching surface meshes is an extremely important topic in FSI, and has been the subject of research by a number of individuals and researchers. Non-matching surfaces are surfaces that occupy the same geometric space, but the vertices and edges of each mesh are not identical, as shown in Figure 2.9.

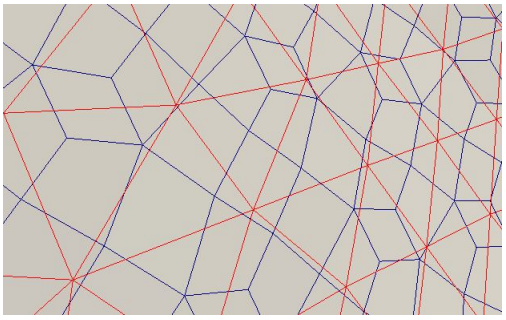

Figure 2.9: Overlap of different mesh vertices and edges used for data mapping from mesh A to mesh B

Mapping provides a means of interpolating data at the surface of an interface, A, onto another, non-matching interface B. There are numerous ways to map data between two non-matching surfaces. The simplest mapping method is the nearest-neighbour mapping [87; 98]. Nearest-neighbour mapping requires only the point's spatial position with no information on node connectivity, and is highly suited for black-box solvers and parallel implementation. The nearest-neighbour mapping sets the value of a point on mesh A equal to the value of the nearest point on mesh B. Nearest-projection mapping offers higher accuracy for non-matching methods, as the point on mesh A is projected onto mesh B and the value is determined based on linear interpolation from the nodes

on mesh B [94]. The nearest-neighbour and nearest-projection mapping schemes are shown in Figure 2.10.

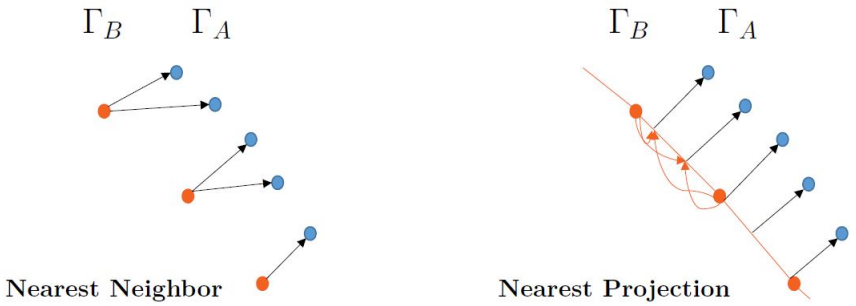

Figure 2.10: Nearest neighbour vs nearest projection methods for data mapping (used with permission from [90])

The RBF method can also be used for data mapping as well as mesh motion. The variable $\boldsymbol{S}(x)$ of Equation 2.30 are the known values of the data on interface A where the weights $\boldsymbol{\alpha}$ are solved for in Equation 2.30. The values for each point on interface B are determined by substituting the point locations into Equations 2.30 with the known weights $\boldsymbol{\alpha}$. The RBF mapping can offer higher accuracy mapping, however the RBF interpolation creates large, dense matrices to be solved, in a similar fashion to the problems in the mesh motion implementation. Uekermann [90] warns that the RBF mapping must be applied with caution in preCICE as it may have a large initialisation time and potentially ill-conditioning of the system matrix. Specific details are not elaborated on in this thesis and the reader is encouraged to read Uekermann [90], Bogaers [88] and Wang *et al.* [98] for more information on mapping techniques.

2.5 Turbulence modelling

2.5.1 Background

Turbulent flow conditions are found in heart valves during peak systole when the flow rate is at its maximum. It is therefore necessary to have an understanding of turbulence modelling to gain an understanding of the blood flow through heart valves. Turbulence modelling has been studied extensively due to its applicability in engineering. Choosing the correct turbulence model for an application is a non-trivial task, encouraging the development of new turbulent models suited for specific categories of turbulent flow, as well as the development of complete general purpose turbulence models [49].

Turbulent flows are typically associated with high Re numbers, where the Re number provides the relationship between the inertial and viscous forces. The Re number was named after Osborne Reynold, who found that the flow of a fluid begins to transition from laminar to turbulent once a critical Re number is reached [99].

When a fluid comes into contact with a surface, a boundary layer forms over the surface. The boundary layer of a fluid flowing over a flat plate is shown in Figure 2.11, where the boundary layer grows and the fluid regime eventually transitions from laminar to transitional to turbulent flow, forming turbulent eddies. The eddies in the turbulent flow regime consist of both large and small eddies, where the kinetic energy of the large eddies are transferred down to small eddies in the energy cascade [49].

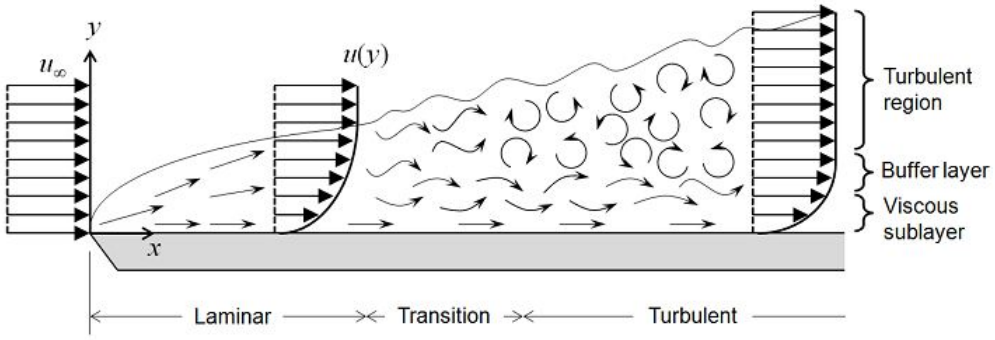

Figure 2.11: Transition of a boundary layer from laminar to turbulent flow (adapted from [100])

The turbulent energy present in the eddies are shown in Figure 2.12, where the high energy large scale eddies are shown in the energetic scales, whilst the lower energy small scale eddies are shown in the inertial subrange and dissipative scales. These small scale eddies are more uniform and universal in characteristics. In the small scale eddies, the kinetic energy is eventually dissipated into thermal energy [49].

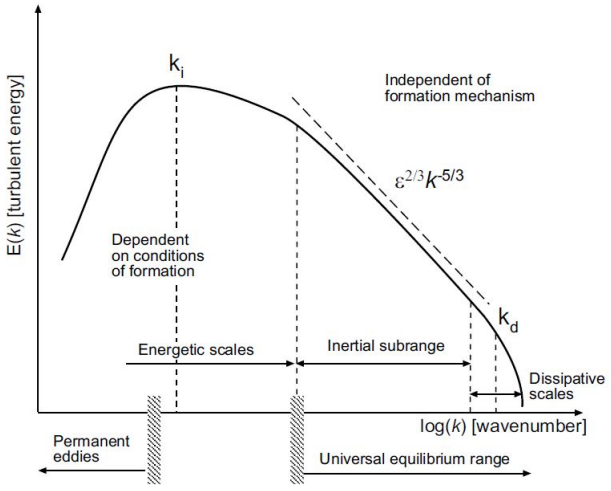

Figure 2.12: Energy cascade for turbulent flow vortices (adapted from [101])

2.5.2 Near wall boundary layer

One of the most prevalent problems in fluid mechanics is simulating turbulent flow near walls, where the wall makes the flow anisotropic and increases the production of turbulence [102]. A boundary layer is formed over the wall, where the velocity varies from the no-slip condition at the wall to the free stream velocity. Near the wall, the viscous forces are more prevalent than inertial forces, whereas the inertial forces are more prevalent far from the wall.

The boundary layer on the wall is subdivided into three regions: 1) viscous sublayer ($y^+ < 5$), 2) buffer layer ($5 < y^+ < 30$) and 3) log-law region ($y^+ > 30$) [103]. The wall y^+ value is a dimensionless distance relating the first cell layer height to the velocity near the wall. The region closest to the wall, the viscous sublayer, is extremely small and the fluid shear stress in this region can be assumed to be constant and equal to the WSS [49]. The various regions, and their associated y^+ values, are shown in Figure 2.13.

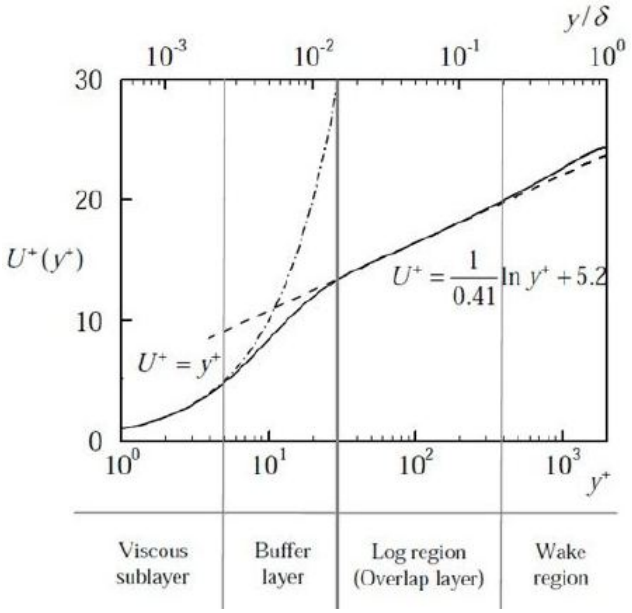

Figure 2.13: Relation between y^+ and U^+ for various regions of y^+ (adapted from [49])

2.5.3 Turbulence models

A variety of turbulence models are available, each with their own advantages and disadvantages. One of the earliest and most common turbulence models is the $\kappa-\varepsilon$ turbulence model, where the solutions for turbulent kinetic energy, κ, and the turbulent dissipation, ε, are solved in addition to the Navier-Stokes equations. The $\kappa-\omega$ *Shear Stress Transport* (SST) model is a combination of the $\kappa-\omega$ and the $\kappa-\varepsilon$ models, where the $\kappa-\omega$ model is used for modelling the boundary layer [104]. In order to provide accurate boundary layer modelling, the first cell layer height must be set so that $y^+ > 30$ for the $\kappa-\varepsilon$ model as the fluid flow is integrated through the boundary layer. Conversely, the $\kappa-\omega$ model can be resolved through the boundary layer for $y^+ < 5$ (low Re number model) and by

integrating through the boundary layer for $y^+ > 30$ (high *Re* number model) [102]. The size of the first layer height for $y^+ > 30$ (integrating through boundary layer) and $y^+ < 5$ (resolving through boundary layer) is shown in Figure 2.14.

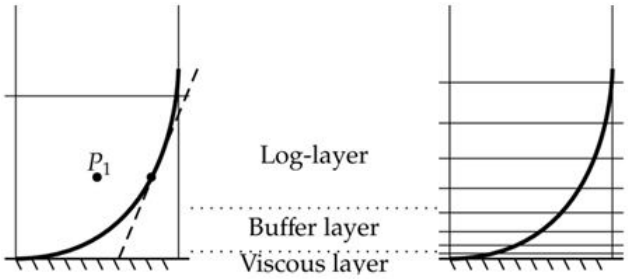

Figure 2.14: First layer cell height comparison for integrating through the boundary layer (left) and resolving through the boundary layer (right)(adapted from [105])

Another method for modelling turbulence is with LES models. A LES model resolves the large eddies in the flow whilst modelling the small eddies by utilising spatial filtering instead of time-averaging [49]. The assumption is that the small turbulent structures are more universal in behaviour than large eddies [99], making the small turbulent structures more suitable for modelling than the large eddies. LES models are commonly coupled with wall functions that integrate through the boundary layer [103], as mesh refinement is required to resolve for the near wall flow characteristics in both the stream wise and cross-flow directions [104].

A variety of turbulence models have been used to model heart valves, however the most common being the $\kappa - \varepsilon$ and $\kappa - \omega$ models. LES models are computationally expensive, which makes it challenging to be used with a transient, moving boundary problem such as a heart valve with limited computational resources. Smadi *et al.* [106] and Alemu and Bluestein [60] used the $\kappa - \omega$ model to simulate the flow through a dysfunctional mechanical valve, whereas Gharaie *et al.* [107] used the realizable$-\kappa - \varepsilon$ to model the turbulent flow through a polymeric aortic valve as the flow during the cardiac cycle varies from laminar to turbulent.

The use of turbulence models for low *Re* number laminar flows may result in erroneous velocity and shear stresses [108]. The choice of computational mesh and boundary conditions may also significantly impact the results. Laminar models were found to be accurate for low *Re* numbers, and the $\kappa - \omega$ *SST* models matched the experimental results well for a number of conditions in an FDA study of the flow through a conical tube and diffuser [108].

Chapter 3

Pulse Duplication

3.1 Introduction

Pulse duplication provides valuable information regarding the hydrodynamic performance of a heart valve *in-vitro* before continuing onto further *iv-vivo* studies. Potentially harmful or fatal designs can be evaluated before clinical testing is performed, significantly decreasing the risk of adverse effects in clinical trials. Chapter 3 discusses pulse duplication on three different heart valves. Section 3.2 describes the functioning of the ViVitro CPD. Section 3.3 describes the setup of the CPD for the experiments and the operating conditions that the heart valves were evaluated under. Section 3.4 provides the results for the pulse duplication tests for all heart valves tested, followed by a discussion of the results in Section 3.5.

3.2 Cardiac pulse duplicator

A ViVitro CPD (ViVitro Labs Inc., British Columbia, Canada), combined with the ViVitest data acquisition system was used for pulse duplication at the Robert WM Frater Cardiovascular Research Centre at the University of the Free State in Bloemfontein, South Africa. A comparison of the various regions of a heart with the ViVitro CPD is shown in Figure 3.1.

The air in the aortic compliance chambers is compressed during systole and decompresses during diastole, allowing the fluid to flow through the systemic resistance circuit and into the atrial chamber during diastole when the aortic valve is closed. The compression of the air in the compliance chambers mimics the Windkessel effect of the expanding tissues of the large arteries.

The ViVitro CPD has two compliance chambers, the aortic compliance chambers and the Viscoelastic Impedance Adapter (VIA). The compliance chambers are completely sealed, with a set volume of air inside the chambers. As the ventricle contracts and expels fluid through the aortic valve during systole, the air in the compliance chambers is compressed. Towards the end of systole, the valve closes with the pressure in the aortic compliance chamber higher than the pressure in the atrial chamber. The compressed air in the compliance chambers help to force fluid through the systemic resistance cir-

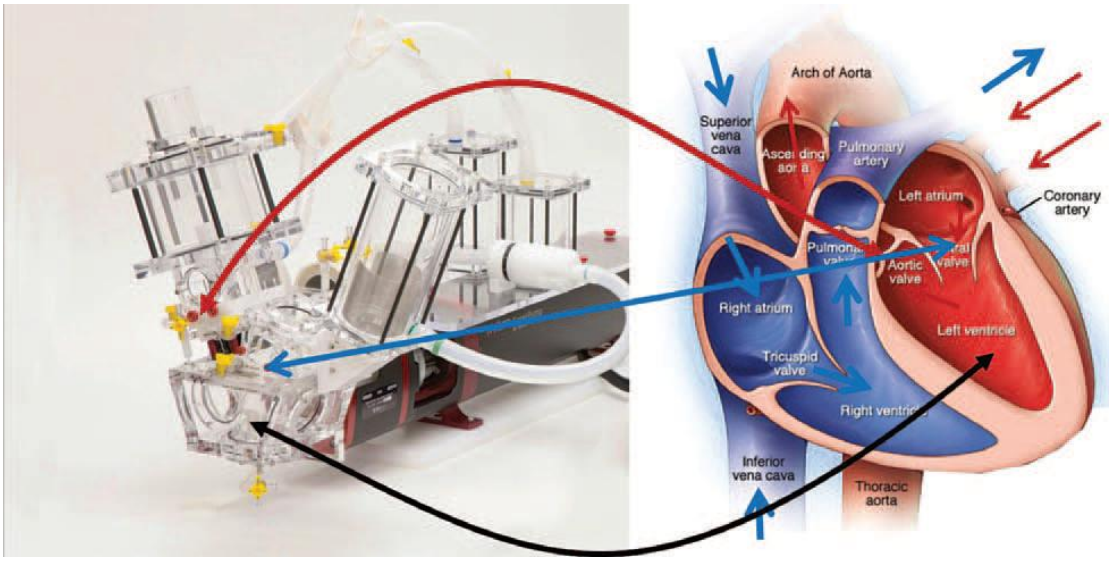

Figure 3.1: Comparison of the ViVitro Labs pulse duplicator regions with a heart (adapted from [18])

cuit during diastole, in a similar fashion that the elastic wall of the arteries aide to push the blood flow through the systemic circulation.

The VIA chamber is located between the linear actuator and ventricle sac. The sudden change in velocity of the linear actuator causes significant pressure oscillations within the Superpump chamber. The VIA dampens out these pressure fluctuations by inserting a small amount of air into the VIA source compliance chamber and the VIA output compliance chambers. The volume of air in each VIA chamber not only dampens out the pressure fluctuations, but also shifts the pressure drop and volumetric flow rate graphs in time to resemble a more physiological flow rate and pressure drop [109]. Jennings *et al.* [109] performed several experiments to determine the effect of the air volumes of the VIA compliance on the pressure and flow rate waveforms, and found that zero VIA compliance resulted in unnatural pressure fluctuations and non-physiological flow rates, where the peak flow rate occurred too soon.

3.3 Methodology

3.3.1 Experimental heart valves

Pulse duplication was performed on three different heart valves (Figure 3.2):

- 19 mm Edwards Lifescience Perimount aortic valve (tissue)
- 19 mm Polyurethane Valve with a height of 8.9 mm (PV tall)
- 19 mm Polyurethane Valve with a height of 5.2 mm (PV short)

Data from the tissue heart valve provided baseline values for comparison as the valve is in commercial use and has proven to have adequate hemodynamic performance and fatigue resistance. A commercial heart valve is recommended to provide baseline data

for testing new heart valve designs as pulse duplication results have been shown to vary depending on the individual CPDs and the experimental setup [21]. Pulse duplication was also performed on the old polyurethane heart valve design moulded from the commercial tissue heart valve.

The polyurethane valves were manufactured at the Centre for Rapid Prototyping and Manufacturing at the Central University of Technology, Bloemfontein, South Africa. The heart valve frames were 3D printed with titanium and placed around an aluminium machined mould of the leaflet shapes. The valves were dip moulded and dried in an oven. Both the PV tall and PV short heart valves were fitted with a custom made Dacron sewing ring, which was then inserted into a plastic retainer and sealed. The plastic retainer was sealed off to prevent any paravalvular leaks within the plastic housing during testing. The plastic retainer was then inserted into a silicon rubber that fit the dimensions of the ViVitro CPD to enable a tight seal and prevent not only paravalvular leaks, but also leaks out of the CPD itself.

Figure 3.2: A commercial tissue heart valve (a), initial polyurethane trileaflet heart valve (b) and the new polyurethane trileaflet heart valve

3.3.2 Calculation procedure

The average pressure drop (Section 2.2.2) and EOA (Section 2.2.3) were calculated according to ISO 5840:2015, however the definition of the regurgitation volume (RV) is not explicitly defined and leaves room for interpretation. In order to perform a consistent analysis of the RV, the same procedure was applied to all tests. According to ISO 5840:2015, a line running parallel to the upward component of the volumetric flow rate must be drawn until the line meets the zero-axis crossing [25], indicating the point in time where closing volume ends and leakage volume begins. In the analysis below, the first peak of the volumetric flow rate after the flow rate becomes negative is chosen as the cut-off between the closing and leakage volumes. As the gradient of the line drawn according to ISO:5840 can vary, the method described here can be applied consistently and can approximate the point in time between closing and leakage. The inflection points chosen to determine the regurgitation are shown in Figure 3.3.

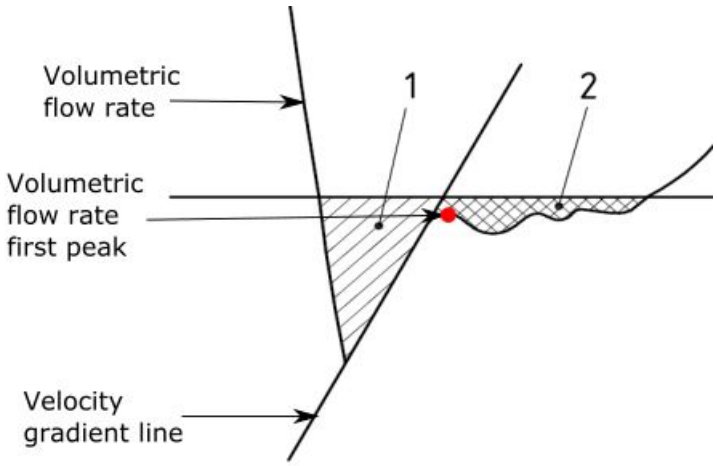

Figure 3.3: Visual representation for consistent calculation of the regurgitation volume (adapted from [25])

3.3.3 Pulse duplicator settings

The Superpump was filled with distilled water, whereas the mock systemic circulatory loop is filled with a saline-glycerol mixture of approximately 47.3% saline and 52.7% distilled water in order to have similar density and viscosity of blood. Each valve was tested under 10 different operating conditions under normotensive pressure conditions [25], as shown in Table 3.1. Under aortic valve conditions, the aortic pressure was set between 120 mmHg and 80 mmHg, ensuring that the maximum aortic pressure did not exceed 120 mmHg. Under pulmonary valve conditions the aortic pressure was set between 35 mmHg and 5 mmHg, where the lowest end diastolic pressure was set to be no less than 5 mmHg. Under aortic and pulmonary pressure conditions, the term aortic pressure refers to the pressure downstream of the heart valve being tested under both aortic and pulmonary valve conditions. Therefore, the pressure drop was always determined by subtracting the aortic pressure from the ventricle pressure.

An example of the aortic pressure, ventricle pressure and volumetric flow rate measured over one cardiac cycle under aortic conditions is shown in Figure 3.4. The cardiac cycle begins at the start of systole (Time = 0 s). The peak aortic pressure rises up to approximately 120 mmHg and slowly decreases to approximately 80 mmHg. The function of the VIA compliance was to reduce the oscillations in the ventricle pressure at the start of systole, where minor oscillations can be seen for the ventricle pressure and small, rapid oscillations in the aortic pressure can be seen the moment the aortic valve closes at approximately 0.4 s into the cardiac cycle. The ventricle pressure oscillations were deemed appropriate as the ventricle pressure only drops below the aortic pressure once near the end of systole.

Table 3.1: Operating conditions of the CPD for hemodynamic testing (BPM - beats per minute, SV - stroke volume, CO - cardiac output, PSP - peak systolic pressure, EDP - end diastolic pressure, MAP - mean aortic pressure)

	BPM	SV [ml]	CO [L/min]	PSP .[mmHg]	EDP .[mmHg]	MAP .[mmHg]
Test 1	60	60	3.6	120	80	100
Test 2	70	72	5.0	120	80	100
Test 3	80	80	6.4	120	80	100
Test 4	100	80	8.0	120	80	100
Test 5	120	80	9.6	120	80	100
Test 6	60	60	3.6	35	5	20
Test 7	70	72	5.0	35	5	20
Test 8	80	80	6.4	35	5	20
Test 9	100	80	8.0	35	5	20
Test 10	120	80	9.6	35	5	20

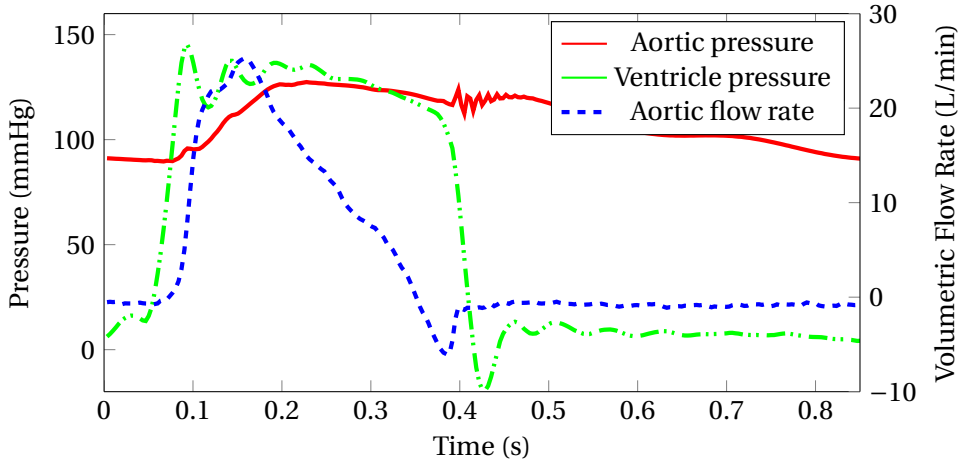

Figure 3.4: Aortic pressure, ventricle pressure and volumetric flow rate for a heart valve tested in a ViVitro pulse duplicator

The amount of air required in the aortic compliance chambers is dependent on achieving the required pressure waveforms. ISO 5840:2015 state that for normotensive pressure waveforms, the peak systolic aortic pressure and the end diastolic aortic pressure should be approximately 120 mmHg and 80 mmHg respectively [25], with a mean arterial pressure (MAP) of 100 mmHg. Under different flow rates and testing conditions, the volume of air in the aortic compliance chamber can change in order to ensure the correct aortic pressure conditions. The VIA compliance chambers were set to 10 ml of air in each of the VIA source and output compliance chambers to reduce spurious pressure oscillations as well as to ensure that the pressure and flow rate waveforms were physiologically representable. An analysis of the impact that the VIA air volume has on the pressure and volumetric flow rate waveforms, as well as the heart valve pulse duplication results, is provided in Appendix B. Increasing the VIA air volume resulted in increased damping of

the pressure drop waveform. The pressure and volumetric flow rate waveforms shifting approximately 33 ms in time, as well as increasing the measured pressure drop.

3.4 Results

3.4.1 Pressure

The peak systolic pressure (PSP), end diastolic pressure (EDP), MAP and pressure drop, under aortic valve conditions (Test 1 to Test 5), are shown in Figures 3.5a to 3.6b. The PSP, EDP, MAP and pressure drop was the average of 10 cycles according to International Organisation of Standards [25]. The pressure values are plotted against cardiac output (CO) specified in Table 3.1. The PSP (Figure 3.5a) was set to a target of 120 mmHg under all CO and varied experimentally between a minimum of 118.5 mmHg and a maximum of 122.8 mmHg between all three heart valves. The EDP (Figure 3.5b) was not constant at 80 mmHg at larger CO's. The tissue and PV tall heart valves were able to maintain a higher EDP when compared to the PV short heart valve, varying between a maximum of 81.6 mmHg and a minimum of 62.6 mmHg for the tissue and PV tall heart valves, whereas the PV short heart valve EDP dropped to a minimum of 48.1 mmHg at a CO of 9.6 L/min.

The MAP under aortic valve conditions (Figure 3.6a) decreased below 100 mmHg as the lower EDP reduced the MAP value, from a maximum of 101.3 mmHg at a CO of 3.6 L/min for the tissue heart valve, to a minimum of 83.8 mmHg at a CO of 9.6 L/min for the PV short heart valve. The pressure drop under aortic conditions (Figure 3.6b) shows that the PV short heart valve had the highest pressure drop over all CO, whereas the PV tall heart valve pressure drop was slightly larger than the tissue valve for all CO.

The PSP, EDP, MAP and pressure drop, under pulmonary valve conditions (Test 6 to Test 10), are shown in Figures 3.7a to 3.8b respectively. The EDP (Figure 3.7b) was set to approximately 5 mmHg under all CO. The EDP was not maintained at 5 mmHg for a CO of 9.6 L/min, where a sharp increase occurred. The tissue heart valve had the highest EDP of 20 mmHg, followed by the PV tall heart valve at 15 mmHg. At the highest CO of 9.6 L/min, the systemic resistance was fully opened and the aortic compliance chamber was completely filled with air to reduce the EDP, however only the PV short valve was able to maintain a low end diastolic pressure of 6 mmHg. The PSP (Figure 3.7a) increased from a minimum of 34 mmHg at a CO of 3.6 L/min for the PV tall heart valve, to a maximum of 73.5 mmHg at a CO of 9.6 L/min for the tissue heart valve. The PSP for the tissue and PV short heart valve were almost identical, with the PV tall valve performing better than the other heart valves.

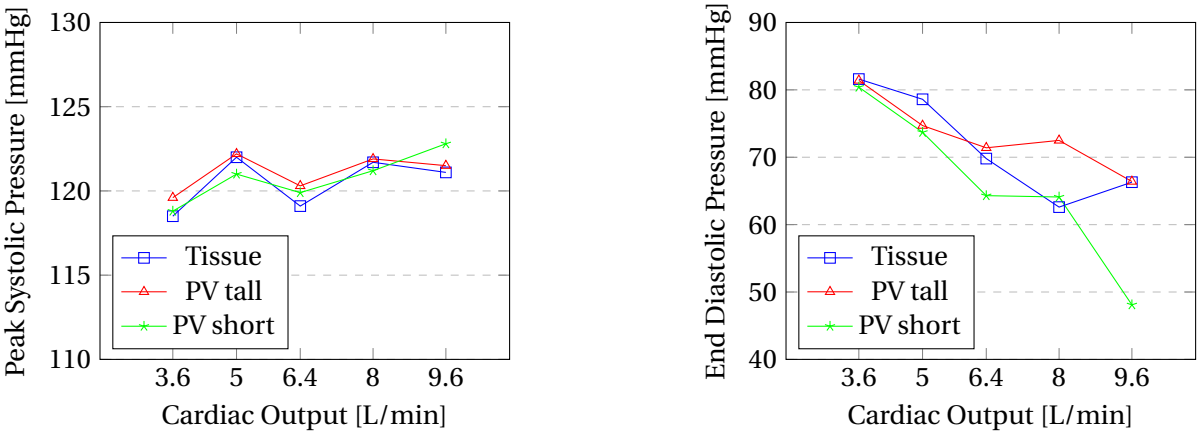

(a) (b)

Figure 3.5: Results for the (a) peak systolic pressure and (b) end diastolic pressure for the tissue, PV tall and PV short heart valves under aortic valve conditions

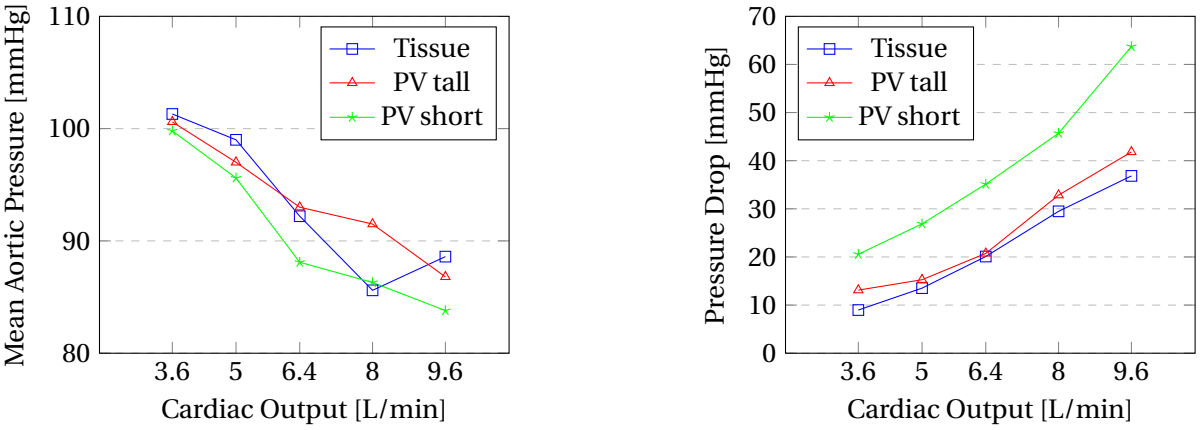

(a) (b)

Figure 3.6: Results for the (a) mean aortic pressure and (b) pressure drop for the tissue, PV tall and PV short heart valves under aortic valve conditions

The MAP increased above 20 mmHg as the PSP almost doubled from a CO of 3.6 L/min to 9.6 L/min. The pressure drop under pulmonary valve conditions (Figure 3.8b) for the PV short heart valve was the largest under all CO conditions, ranging from 18.5 mmHg to 48.8 mmHg, consistent with the findings under aortic valve conditions. The pressure drop for the PV tall and tissue heart valves were almost identical at a CO of 3.6 and 5 L/min, after which the PV tall heart valve had a larger pressure drop than the tissue heart valve.

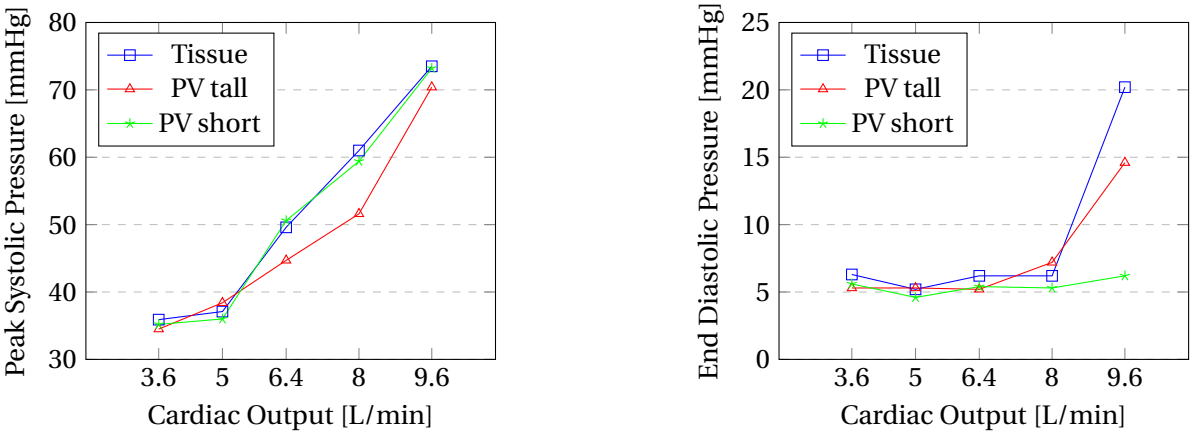

(a) (b)

Figure 3.7: Results for the (a) peak systolic pressure and (b) end diastolic pressure for the tissue, PV tall and PV short heart valves under pulmonary valve conditions

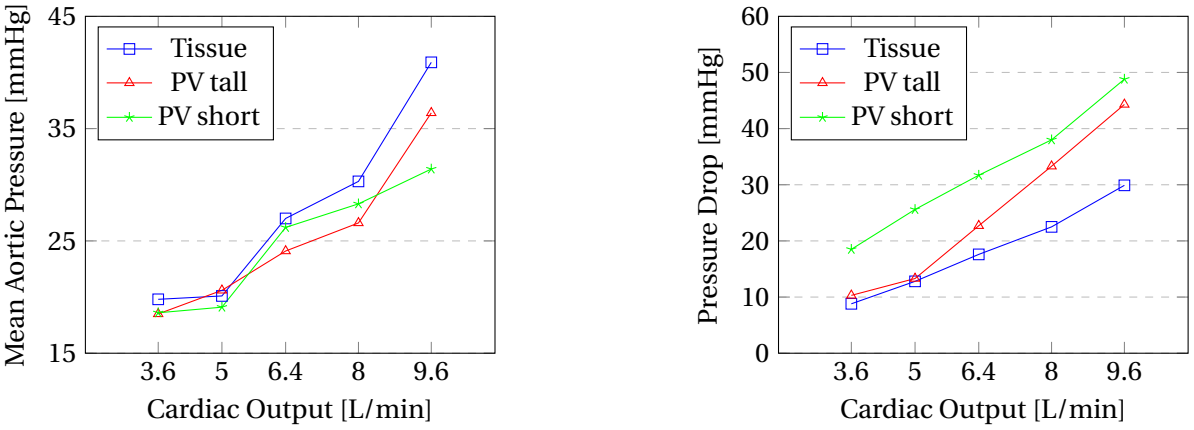

(a) (b)

Figure 3.8: Results for the (a) mean aortic pressure and (b) pressure drop for the tissue, PV tall and PV short heart valves under pulmonary valve conditions

3.4.2 Effective orifice area

The EOA of the tissue, PV tall and PV short heart valves, under aortic valve conditions, is shown in Figure 3.9. The tissue heart valve had the largest EOA for a CO of 3.6 L/min and 5 L/min, whereas the PV tall heart valve was the largest EOA at a CO from 6.4 L/min to 9.6 L/min. The PV short heart valve had the lowest EOA for all CO, ranging from 0.84 at a CO of 3.6 L/min to 1.29 at a CO of 9.6 L/min. Following ISO:5840, the minimum EOA requirement for a 19 mm heart valve is 0.75, therefore all heart valves meet the minimum EOA requirements for a 19 mm heart valve [25].

The EOA of the three tested heart valves, under pulmonary valve conditions, is shown in Figure 3.10. The tissue heart valve was the largest for a CO of 3.6 L/min and 9.6 L/min, whereas the PV tall heart valve was the largest at CO from 5 L/min to 8 L/min. The performance of the tissue heart valve varied minimally under pulmonary conditions compared to aortic conditions, where the tissue heart valve EOA under pulmonary conditions was lower than under aortic conditions apart from at a CO of 9.6 L/min. The PV short heart valve was the lowest for all EOA, ranging from 0.79 at a CO of 3.6 L/min and 1.31 at a CO of 9.6 L/min, similar to the findings under aortic conditions.

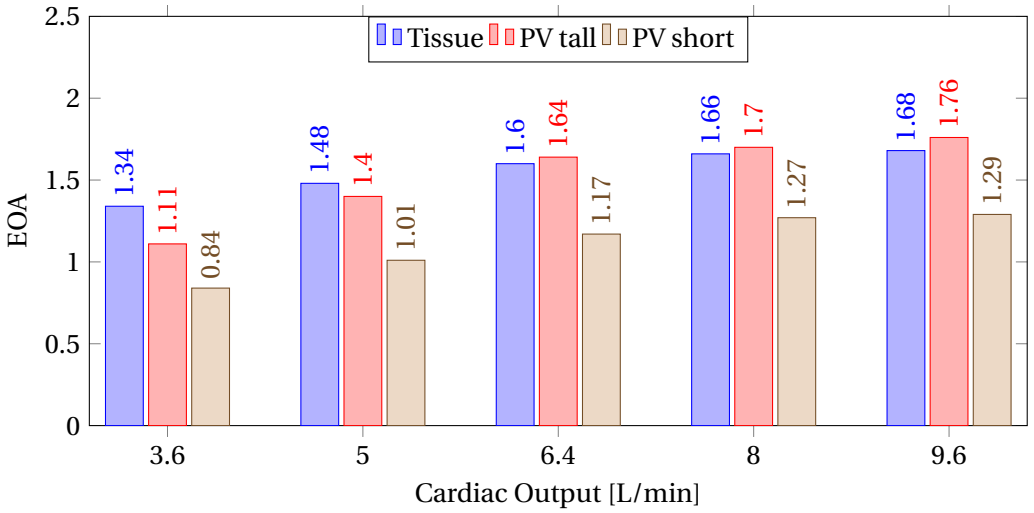

Figure 3.9: EOA for the tissue, PV tall and PV short heart valves under aortic valve conditions

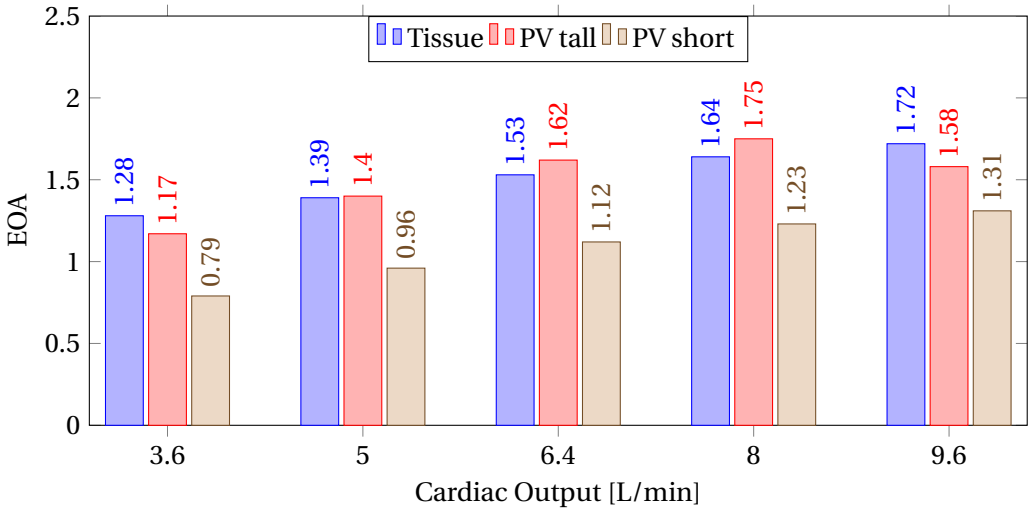

Figure 3.10: EOA for the tissue, PV tall and PV short heart valves under pulmonary valve conditions

3.4.3 Regurgitation

The percentage RV for the tissue, PV tall and PV short heart valves, under aortic valve conditions, is shown in Figure 3.11. The PV short heart valve had the largest percentage RV, ranging from 29.9% at a CO of 3.6 L/min, to 12% at a CO of 9.6 L/min. The tissue heart valve had the lowest percentage RV, ranging from 11.5% at a CO of 3.6 L/min, to 4.8% at a CO of 9.6 L/min. ISO 5840 stipulates that the percentage RV for a 19 mm heart valve cannot be more than 10%. The tissue heart valve satisfies this condition for all CO apart from a CO of 3.6 L/min. The PV tall heart valve outperforms the PV short heart valve for all CO, where the difference between the PV tall and PV short is more pronounced at low CO.

The percentage RV for the tissue, PV tall and PV short heart valves, under pulmonary valve conditions, is shown in Figure 3.12. Once again the PV short heart valve had the largest percentage regurgitation, ranging from 23.4% at a CO of 3.6 L/min, to 12.1% at a CO of 9.6 L/min. The tissue heart valve had the lowest percentage RV, ranging from 4.6% at a CO of 3.6 L/min, to 2.9% at a CO of 6.4 L/min, well below the threshold of 10% for a 19 mm heart valve according to ISO 5840. The percentage regurgitation of the PV tall heart valve varied between a maximum of 14.7% at a CO of 3.6 L/min to a minimum of 8.4% at a CO of 9.6 L/min, and once again outperformed the PV short heart valve.

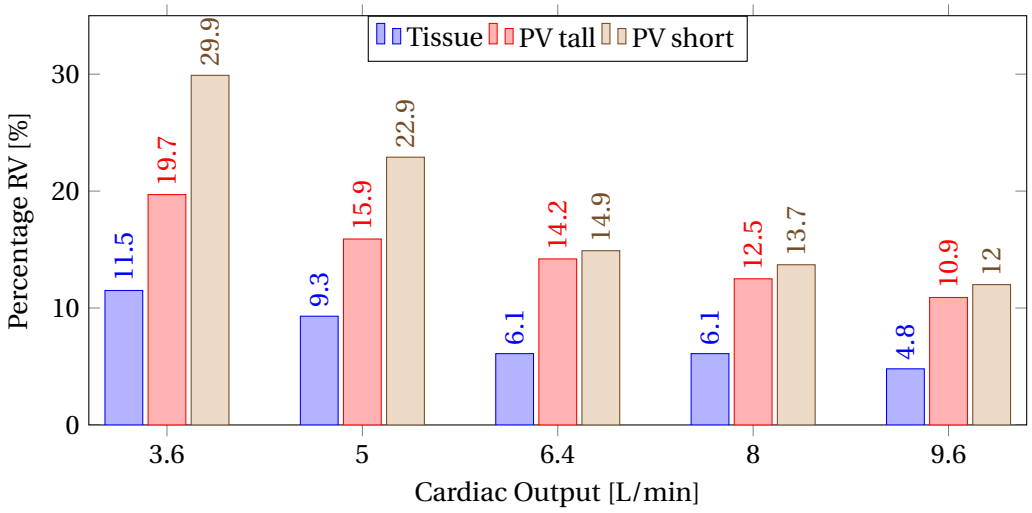

Figure 3.11: Percentage regurgitation for the tissue, PV tall and PV short heart valves under aortic valve conditions

The difference in the type of regurgitation, closing volume versus leakage volume as a percentage of the total RV under aortic and pulmonary conditions, is shown in Table 3.2. Under aortic conditions, the closing volume percentage for the tissue heart valve was lower than the leakage volume for all CO, ranging from 9.17% to 27.55%, whereas the closing volume percentage for the PV tall heart valve ranged from 29.27% to 56.99%. More than half of the total regurgitation of the PV tall heart valve was due to the closing volume at a CO of 8.0 L/min and 9.6 L/min. This is in contrast to the tissue and PV

short heart valve, where the leakage is consistently higher for all CO, shedding light on the impact of the closing mechanisms of the heart valves. Under pulmonary conditions, the amount of regurgitation contributed by the closing volume for each valve increased, apart from the PV short heart valve at a CO of 8 L/min and 9.6 L/min. The closing volume percentage of the tissue, PV tall and PV short heart valves ranged from 20.86%, 45.25% and 27.61% respectively at a CO of 3.6 L/min, to 37.47%, 62.48% and 32.89% respectively at a CO of 9.6 L/min.

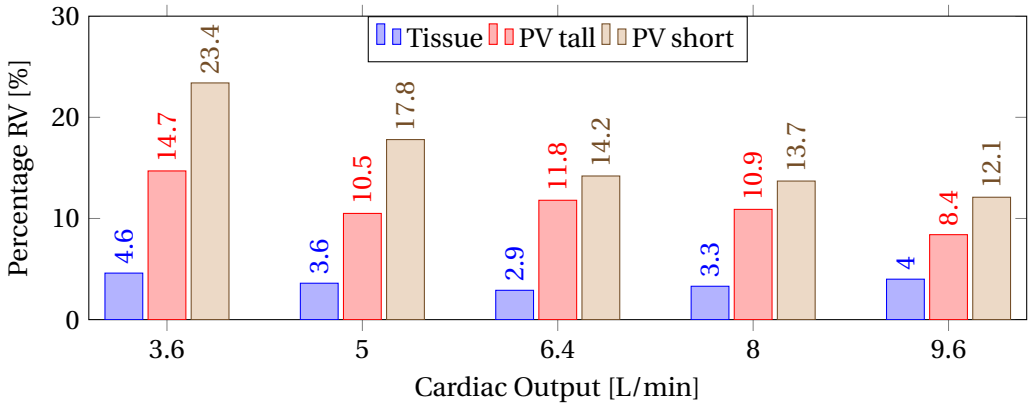

Figure 3.12: Percentage regurgitation for the tissue, PV tall and PV short heart valves under pulmonary valve conditions

Table 3.2: Percentage difference of the closing volume and leakage volume for the tissue, PV tall and PV short heart valves under aortic valve condition. CO - Cardiac output [L/min]

Tissue - Aortic		
Closing	CO	Leakage
9.17%	3.6	90.83%
10.72%	5	89.28%
16.43%	6.4	83.57%
19.68%	8	80.32%
27.55%	9.6	72.45%

PV tall - Aortic		
Closing	CO	Leakage
29.27%	3.6	70.73%
30.58%	5	69.42%
42.28%	6.4	57.72%
50.27%	8	49.73%
56.99%	9.6	43.01%

PV short - Aortic		
Closing	CO	Leakage
22.29%	3.6	77.71%
24.14%	5	75.86%
31.59%	6.4	68.41%
31.85%	8	68.15%
33.07%	9.6	66.93%

Tissue - Pulmonary		
Closing	CO	Leakage
20.86%	3.6	79.14%
22.49%	5	77.51%
26.88%	6.4	73.12%
29.63%	8	70.37%
37.47%	9.6	62.53%

PV tall - Pulmonary		
Closing	CO	Leakage
45.25%	3.6	54.75%
41.67%	5	58.33%
54.53%	6.4	45.47%
57.32%	8	42.68%
62.48%	9.6	37.52%

PV short - Pulmonary		
Closing	CO	Leakage
27.61%	3.6	72.39%
29.85%	5	70.15%
32.54%	6.4	67.46%
29.14%	8	70.86%
32.89%	9.6	67.11%

3.5 Discussion

3.5.1 Pressure drop

The pressure drop for the PV short heart valve was significantly larger than the PV tall and tissue heart valves under both aortic and pulmonary valve conditions. By examining the opening of the heart valves during peak systole, the minimum geometric orifice area of the PV short heart valve (Figure 3.13a) was significantly smaller than the PV tall (Figure 3.13b), where the PV short had an orifice diameter of approximately 12 mm compared to approximately 16 mm for the PV tall heart valve. In addition to the small open geometric area, the PV short heart valve had a low profile design, where the majority of the leaflet sits almost perpendicular to the direction of flow when closed due to its design, increasing the energy necessary to open the heart valve and increasing the pressure drop.

The manner in which the polymer material of the PV short heart valve leaflets attached to the titanium frame differed significantly to that of the PV tall heart valve. The polymer leaflets of the PV short heart valve protrude radially towards the centre of the heart valve, whereas the PV tall heart valve leaflets protrude vertically off of the frame before bending towards the heart valve center. The difference in the leaflets design enabled the PV tall heart valve to open more easily than the PV short, increasing the open geometric area of the valve and reducing the pressure drop.

The EDP of the PV short heart valve was lower than that of the tissue and PV tall heart valves, as shown in Figure 3.5b. The PV short heart valve did not close completely during diastole, leaving a gap open at the center of the valve. The gap allowed for fluid to flow not only through the systemic resistance circuit, but also back through the heart valve and into the ventricle, relieving the pressure downstream of the PV short heart valve much quicker than for the other two heart valves. The drop in EDP reduced the MAP, as the aortic pressure was reduced for the cardiac cycle.

Ducci *et al.* [38] performed pulse duplication with a reduced mean systolic aortic pressure of 55 mmHg instead of 100 mmHg as specified by ISO 5840, where the authors concluded that the reduced mean systolic aortic pressure had negligible effects on the pressure drop and flow rate. By examining Figure 3.6b and Figure 3.8b, the pressure drop decreases when a lower MAP is used during testing, especially at higher CO, drawing some scepticism on testing with a lower MAP.

The pressure drop of the PV short heart valve was higher than that of the tissue and PV tall heart valves under pulmonary valve conditions (Figure 3.8b). The reason for the larger pressure drop of the PV short heart valve under pulmonary conditions was the same as that of the aortic conditions. The PSP under pulmonary conditions (Figure 3.7a) was not constant at 35 mmHg at CO above 5 L/min. The aortic pressure increases at larger CO, as there is not enough time for the pressure to subside in the aortic chamber before the next cardiac cycle begins, causing the rise in the PSP.

The EDP under pulmonary conditions (Figure 3.7b) fluctuated consistently around 5 mmHg for CO below 8 L/min. A sharp increase in the tissue and PV tall heart valves

EDP was observed, however the PV short heart valve did not. The PV short heart valve does not close properly during diastole, allowing the fluid to flow back into the ventricle in the same manner as the EDP under aortic conditions. The systemic resistance was fully opened and the aortic compliance chambers were filled with air to reduce the end diastolic pressure with negligible effect. The systemic circuit was partially drained to reduce the volume of liquid in the aortic chamber downstream of the heart valve with minimal impact on reducing the EDP. The MAP increased with CO as the PSP increased at a higher rate than the EDP.

[a]  [b] 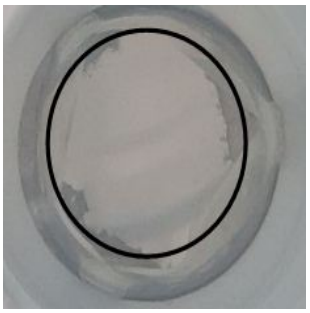

Figure 3.13: Top view during peak flow of the (a) PV short and (b) PV tall heart valve

3.5.2 Effective orifice area

The EOA is a measure of the ease with which fluid is able to pass through the heart valve [25], where a larger EOA is indicative of a superior performing heart valve. The EOA of the PV short heart valve was the lowest at all CO under both aortic and pulmonary valve conditions, where the tissue and PV tall heart valves had the largest EOA's under differing conditions. By examining Equation 2.2, the EOA is directly proportional to the Q_{rms} and inversely proportional to the pressure drop. The PV short valve had a larger pressure drop (Section 3.5.1) for all CO, thereby reducing the EOA. All three heart valves met the minimum EOA requirement according ISO 5840:2015, thereby not representing a problem for heart valve certification in the future, however other metrics such as regurgitation, fatigue life and bio-compatibility would still need to be met.

3.5.3 Regurgitation

The percentage RV of the tissue heart valve satisfied the minimum requirement of ISO 5840:2015 for all tests (Figure 3.11 and Figure 3.12) for both aortic and pulmonary conditions, apart from at a CO of 3.6 L/min for aortic conditions. The low percentage RV is due to a combination of a highly flexible material (pericardium) as well as effective sealing of the leaflets during diastole to limit the leakage volume. The tissue valve closes efficiently and quickly, evident by the low percentage closing volume compared to the percentage leakage volume (Table 3.2).

In contrast to the tissue heart valve, the PV tall heart valve had a larger portion of the regurgitaion attributed to the closing volume, especially under pulmonary conditions.

The leaflets of the PV tall valve protrude vertically off of the frame, whereas the PV short and tissue heart valve leaflets protrude radially off of the frame towards the valve center (Figure 3.14). The geometry of the tissue and PV short heart valves leaflet attachment helps with reducing the closing volume as the stress in the leaflets help pull the valve back to the closed position without external forces, whereas the PV tall heart valve requires a small amount of reverse flow to help push the heart valve leaflets closed. The PV tall heart valve had a larger percentage RV than the minimum requirement according to ISO 5840:2015. Additional design changes will be necessary to ensure a lower closing volume, by adjusting the height that the titanium frame fits onto the mould and shifting the position that the leaflets attach to the frame. The new design will have to be evaluated as the pressure drop and EOA performance will differ. The PV tall heart valve had adequate sealing during diastole, limiting the leakage volume.

[a] 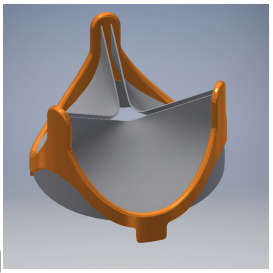 [b] 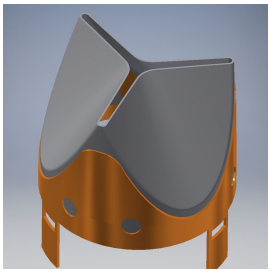

Figure 3.14: CAD designs of the heart valve leaflet attachment to the frame for the (a) PV short and (b) PV tall heart valves.

The percentage RV was observed to have reduced under pulmonary conditions when compared to aortic conditions, which can be attributed to the reduced MAP. The higher leakage volume of the PV short heart valve can be attributed to the gaps between the leaflets during diastole. The gaps between the leaflets provide a passage for fluid to flow back into the ventricle as the ventricle sac is expanding during diastole.

3.5.4 Visual observation

Observation of the heart valves was conducted to determine any difference regarding the opening and closing behaviour of the heart valves. The tissue heart valve offered almost no resistance to opening, thereby allowing for a low pressure drop. The tissue heart valve closed almost immediately and tightly, thereby having a small closing and leakage volume (Figure 3.15a and 3.15b). The PV tall heart valve opened easily and two of the three leaflets remained opened without any forces required to keep the heart valve open (Figure 3.15c). The ease of opening translates to a relatively low pressure drop. Adversely, in order for the PV tall heart valve to close, reverse flow is required to force the leaflets closed, translating to a higher closing volume. The PV short heart valve had a very small opening orifice that closes on its own in approximately 5 seconds (Figure 3.16a to 3.16c). This self closing mechanism helped to lower the closing volume, however the remaining

gap between the closed leaflets allowed for a large leakage volume (Figure 3.16c).

[a]  [b]  [c] 

Figure 3.15: (a) forced open position of the tissue heart valve, (b) naturally closed position of the tissue heart valve and (c) naturally opened position of the PV tall heart valve

[a]  [b]  [c] 

Figure 3.16: (a) forced open position of the PV short valve, (b) mid closing position of the PV short heart valve without external forces and (c) naturally closed position

3.6 Conclusion

Pulse duplication was performed on three different heart valves. The tissue heart valve had the lowest percentage RV under both aortic and pulmonary valve conditions. The PV short heart valve had a large leakage volume due to gaps between the heart valve leaflets that allowed fluid to flow backwards during diastole. The PV tall heart valve had a larger percentage closing volume due to the leaflet shape that allowed for easy opening of the heart valve, but increased the closing volume. The tissue heart valve was the only heart valve to satisfy the minimum percentage RV requirement for ISO 5840:2015. The new polyurethane heart valve will require adjustments to the height that the titanium frame fits onto the mould.

The tissue heart valve had the lowest average pressure drop and the PV short heart valve had the largest average pressure drop. The PV short heart valve could not maintain the EDP due to the excessive leakage of the heart valve. All heart valves satisfied the minimum EOA requirement for ISO 5840:2015.

Chapter 4

Particle Imaging Velocimetry

4.1 Introduction

This chapter describes the procedure for performing particle image velocimetry (PIV) for two polyurethane heart valves and a commercial tissue heart valve. PIV was performed on a CPD developed at the University of Stellenbosch and further enhanced by Rodriguez [20]. Section 4.3 describes the methodology used to extract the velocity vectors from the PIV images and the post-processing techniques used to obtain the VSS, RSS, RSS_{maj} and TVSS, as well as the filtered shear stress results. Section 4.2 describes the experimental setup of the CPD and PIV equipment. Section 4.4 shows the results obtained for the PIV experiments, followed by a discussion of the results in Section 4.5.

4.2 Experimental setup

A sketch of the PIV setup is shown in Figure 4.1, with the interrogation areas shown in the shaded gray areas. The camera had a resolution of 2048 x 2048 pixels, with the wavelength of 532 nm and 3 mm thick. A final interrogation window of 32 x 32 was used with adaptive correlation to obtain the velocity vector fields. The laser pulse seperation was adjusted for each test between 200 μs and 500 μs to ensure that particle movement of approximately 8 pixels was observed to reduce spurious vectors and to enhance accuracy of the velocity interpolation. The fluid was seeded using Dantec Dynamics PSP-50 Polyamid seeding particles, diam. 50 μm, 250 g, with diameters of 50 μm. The laser timing was synced to the CPD to ensure that the PIV system fired at exactly the same point in time between each cardiac cycle. A synchronisation signal was sent from the CPD controller to the PIV system so that 300 repeatable image pairs were obtained.

The ventricle volume and volumetric flow rate conditions of the CPD are shown in Figure 4.2. The input change in ventricle volume was obtained from the volumetric flow rate from the ViVitro CPD described in Chapter 3 and programmed into the Stellenbosch University CPD. The flow rate waveform represents a physiological waveform where there is a sharp increase in the flow rate during the first third of the systolic phase. Once the volumetric reaches the maximum flow rate at approximately a third into the

systolic phase, the flow rate decreases at a relatively constant rate.

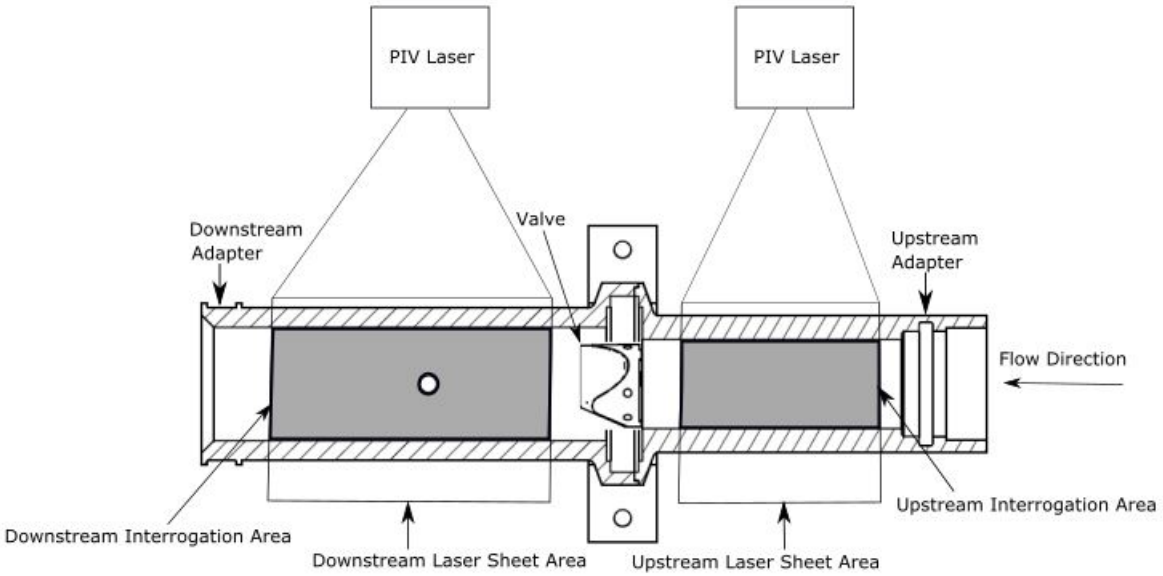

Figure 4.1: Diagram of the PIV experimental setup

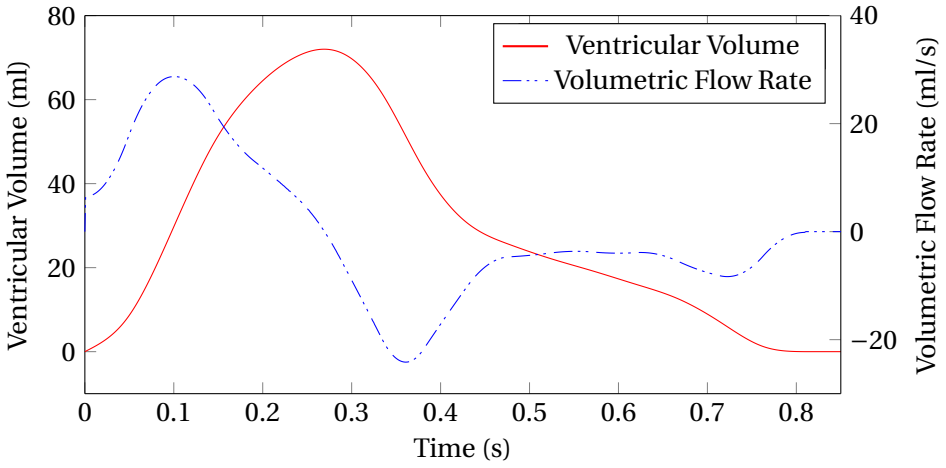

Figure 4.2: Experimental flow rate and corresponding change in ventricular volume for the PIV testing

4.3 Methodology

A Dantec Dynamics (2012) system, with a FlowSense 4M camera, DualPower laser and Dynamic Studio post-processing software was used to perform the PIV experiments and

post-processing of raw images to obtain 2D velocity vectors in a 2D plane. PIV was performed both downstream and upstream of the heart valves during systole and diastole respectively, where PIV was performed during diastole to check for reverse flow through the heart valves, similar to Leo *et al.* [42]. Once the PIV system had obtained the image sets, masking was performed to extract the region to apply post-processing and obtain the velocity vectors.

The velocity vector data set was used to determine the VSS, RSS, RSS_{maj} and TVSS. The VSS was determined using the shear stress for a simple laminar flow case defined in Equation 2.6. The RSS refers specifically to the τ_{xy} term in the RSS tensor, representing the shear stress and not normal Reynolds stresses, as done in Yen *et al.* [45]. The algorithm describing the process of determining the RSS and RSS_{maj} is shown in Algorithm 2, as described in section 2.3.2. The velocity vector data sets was used to determine the mean velocity values over all 300 images, where one image was captured per cardiac cycle on the pulse duplicator. The mean velocity was used to determine the velocity fluctuation for RSS, RSS_{maj}.

Algorithm 2 RSS and RSS_{maj} Algorithm

1: **procedure** FROM KNOWN VALUES OF u AND v VELOCITY VECTOR FIELDS
2: u and v are the velocities in the x and y direction respectively
3: $\overline{u} = \frac{1}{N}\sum_{i=1}^{N} u$
4: $\overline{v} = \frac{1}{N}\sum_{i=1}^{N} v$
5: $u^{'} = u - \overline{u}$
6: $v^{'} = v - \overline{v}$
7: $RSS = \rho\overline{u^{'}v^{'}}$
8: $RSS_{maj} = \rho\sqrt{\left(\frac{\overline{u^{'}u^{'}} - \overline{v^{'}v^{'}}}{2}\right)^2 + \left(\overline{u^{'}v^{'}}\right)^2}$

Algorithm 3 TVSS Algorithm

1: **procedure** FROM KNOWN VALUES OF $\bar{U}$, $\bar{V}$ VELOCITY VECTOR FIELDS
2: $\bar{S}_{ij} = \frac{1}{2}(\frac{\delta\bar{V}}{\delta x} + \frac{\delta\bar{U}}{\delta y})$ where δx and δy are known
3: set constant $C_s = 0.17$
4: $|\bar{S}| = \sqrt{2\bar{S}_{ij}\bar{S}_{ij}}$
5: $\tau_{ij} = -C_s^2\Delta^2|\bar{S}|\bar{S}_{ij}$
6: $\epsilon = \tau_{ij}\bar{S}_{ij}$
7: $TVSS = (\frac{1}{2}\rho\mu\epsilon)^2$

The algorithm describing the process of determining the TVSS is shown in Algorithm 3. The resolved strain rate tensor and the SGS stress (Equation 2.17) was used to determine the eddy dissipation (Equation 2.16), which models the kinetic energy that is transferred from the resolved scales to the small, modelled scales [48].

4.4 Results

4.4.1 Velocity profile

The velocity magnitude during peak flow of systole of all three heart valves are shown in Figure 4.3. The x axis (horizontal) represents the radial distance of the heart valve perpendicular to the flow direction through the tube, and the y axis displays the axial distance downstream from the heart valve, where the heart valve is situated at the bottom of the image. The fluid flow direction during systole is from bottom to top, where the fluid flow during diastole is from top to bottom (reverse flow).

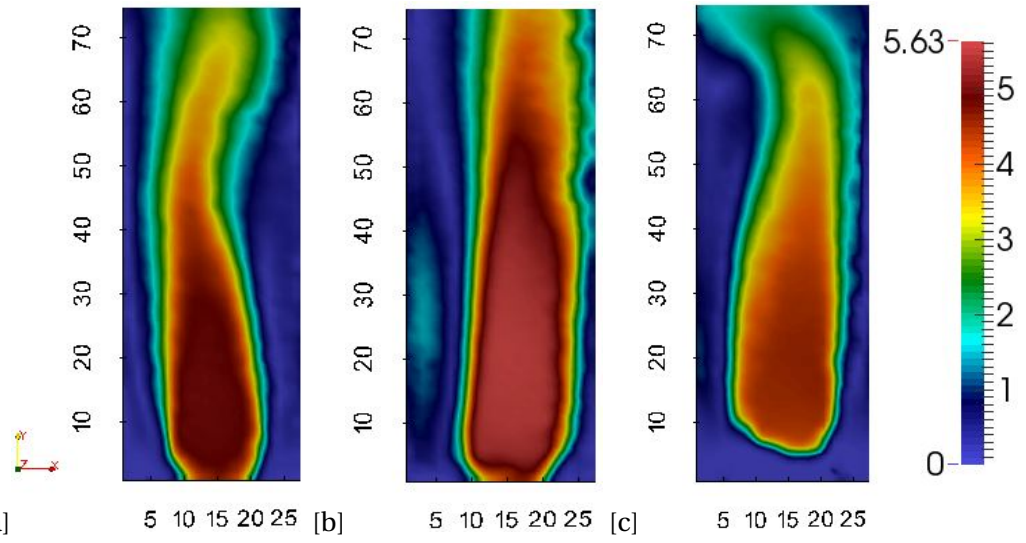

Figure 4.3: Velocity magnitude [m/s] for the (a) tissue (b) PV short and (c) PV tall heart valve during peak systole at 150 ms in the cardiac cycle

The maximum velocity obtained from PIV was 4.9 m/s, 5.6 m/s and 4.5 m/s for the tissue, PV short and PV tall valve respectively. The first 5 mm to 10 mm of the PV tall heart valve measured zero velocity as the polyurethane leaflets protruded into the field of vision, therefore the camera did not pick up the seeding particles behind the leaflets. The velocity profile of the tissue valve angles to the left, where after 40 to 48 mm downstream of the valve the velocity jet curves to the right. The PV tall valve exhibits a similar trend, where the central jet initially angles to the right and curves left after 55 mm. The PV short valve angles to the right without moving back towards the centre of the tube. The maximum reverse flow at the start of diastole during heart valve closing is shown in Figure 4.4. The tissue heart valve had the lowest reverse flow velocity of 0.046 m/s, whereas the PV tall heart valve had the largest reverse flow velocity of 0.44 m/s, almost

double the reverse flow velocity of the PV short heart valve.

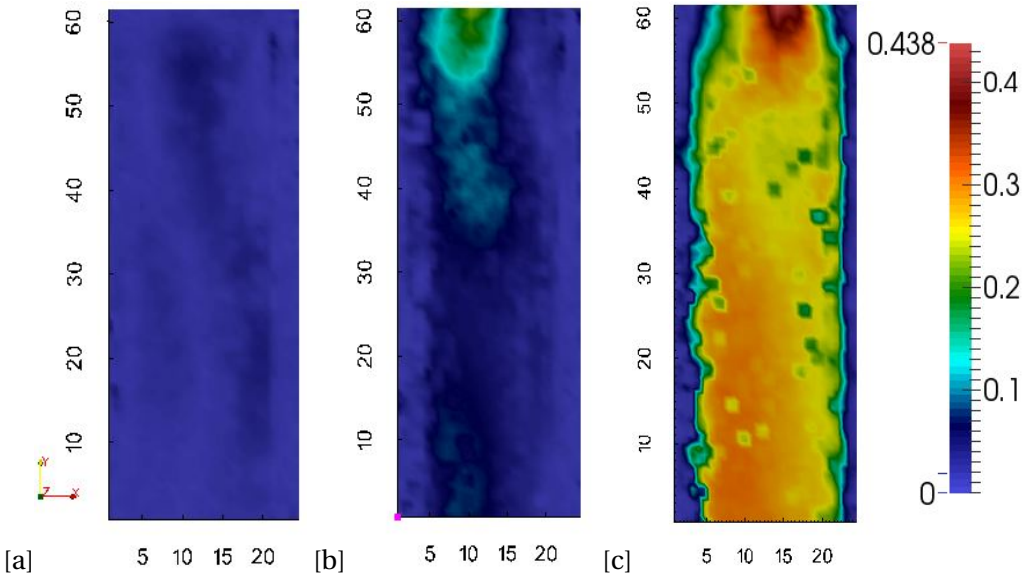

Figure 4.4: Velocity magnitude [m/s] for the (a) tissue (b) PV short and (c) PV tall heart valve during early diastole at 500 ms in the cardiac cycle

The velocity profile for the tissue, PV short and PV tall heart valve at peak flow is shown in Figure 4.5 and Figure 4.6. The results are only presented during peak flow for brevity as peak flow exhibited the largest recirculating flow and maximum velocity. Recirculating flow was observed around the left and right sides of the velocity jet (radial distance of less than 5 mm and more than 24 mm) for the tissue heart valve. The PV short heart valve had an asymmetric distribution of the velocity profiles, where a larger recirculating flow velocity is noted at a radial distance of less than 7 mm with a maximum velocity of -1.4 m/s. The right side wall velocity of the PV short valve was large at 1.44 m/s at an axial distance of 60 mm, whereas velocities near zero are shown for axial distances of 1 mm, 5 mm and 10 mm. The velocity profile for the PV tall heart valve was skewed to the right at an axial distance of 5 mm, 40 mm and 60 mm from the heart valve, but with lower recirculating velocities on the left side of the heart valve than the PV short heart valve. A maximum recirculating flow velocity of -0.86 m/s was observed at an axial distance of 25 mm on the left side of the PV tall heart valve.

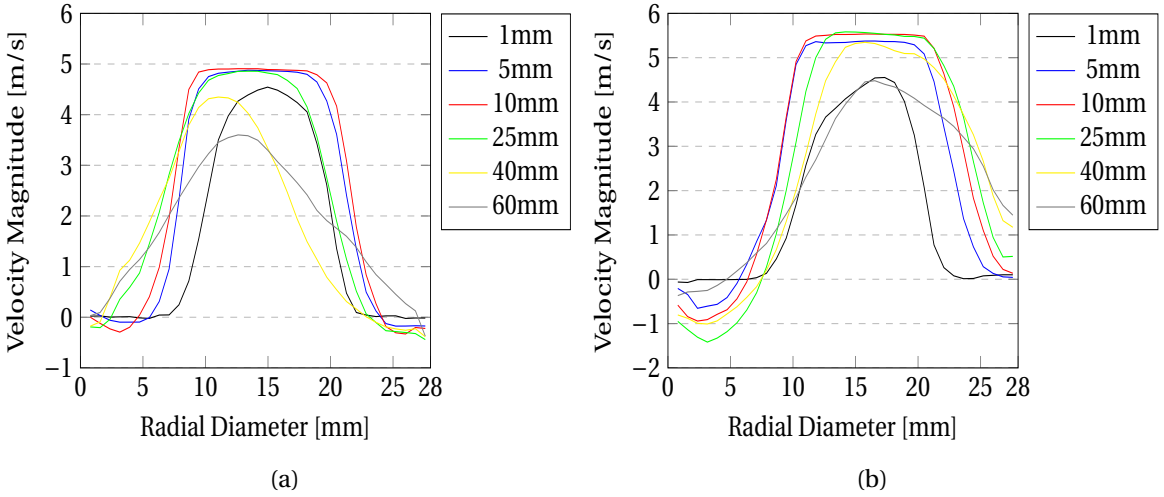

Figure 4.5: Velocity profile distribution at various distances downstream of the (a) tissue heart valve and (b) PV short heart valve at peak velocity

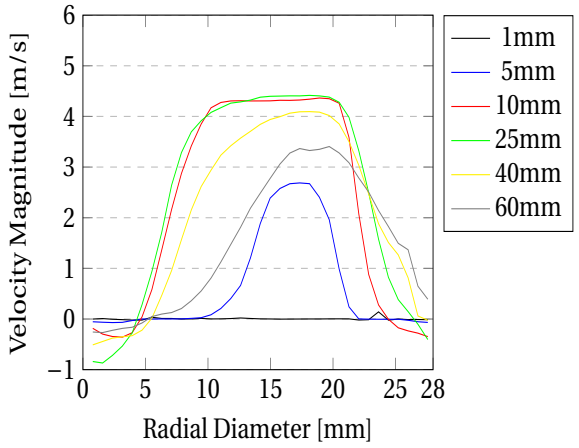

Figure 4.6: Velocity profile distribution at various distances downstream of the PV tall heart valve at peak velocity

The maximum reverse flow velocity of all three heart valves is shown in Table 4.1. The maximum reverse flow velocity of the PV tall heart valve reduces significantly from 600 ms into the cardiac cycle until the start of systole. In contrast to the PV tall heart valve, the PV short heart valve increases during diastole. The tissue heart valve had extremely low reverse velocity in the heart valve throughout diastole.

Table 4.1: Summary of various PIV metrics for all three heart valves during diastole

	Tissue				
Time [ms]	Velocity [m/s]	VSS [Pa]	RSS [Pa]	RSS_{maj} [Pa]	TVSS [Pa]
500	0.047	-0.11	-1.2	2.2	0.2
600	0.051	-0.11	-1.2	1.7	0.11
700	0.073	0.12	-0.75	1.2	0.089

	PV Short				
Time [ms]	Velocity [m/s]	VSS [Pa]	RSS [Pa]	RSS_{maj} [Pa]	TVSS [Pa]
500	0.23	0.17	-19	31	0.69
600	0.31	0.32	-19	31	0.61
700	0.41	0.45	26	61	0.89

	PV Tall				
Time [ms]	Velocity [m/s]	VSS [Pa]	RSS [Pa]	RSS_{maj} [Pa]	TVSS [Pa]
500	0.44	-0.59	-21	36	0.6
600	0.11	-0.24	8.8	18	0.48
700	0.1	-0.2	4.6	9.4	0.37

4.4.2 Viscous shear stress

The VSS for the tissue, PV short and PV tall heart valves, during peak flow, are shown in Figure 4.7 and calculated using Equation 2.6. The regions around the central orifice jet experienced the maximum VSS as the largest velocity gradients occur in the region around the central jet. The maximum VSS for the tissue, PV tall and PV short heart valves are 6.7 Pa, 5.8 Pa and -5.8 Pa respectively. The peak VSS for the tissue heart valve occurs in a small region approximately 5 mm in length around the left side of the central jet, whereas the peak VSS for the PV short heart valve was observed to be approximately 20 mm in length. The PV tall heart valve had a relatively short peak VSS region of approximately 7 mm in length on the right side of the central jet. Note that the sign of the VSS is irrelevant and only the absolute value of the VSS is important for determining the potential for platelet activation and hemolysis. The sign indicates the direction of rotation of the fluid at any spatial point. The maximum VSS measured during diastole were approximately one order of magnitude lower than the maximum VSS results found during systole, as shown in Table 4.1.

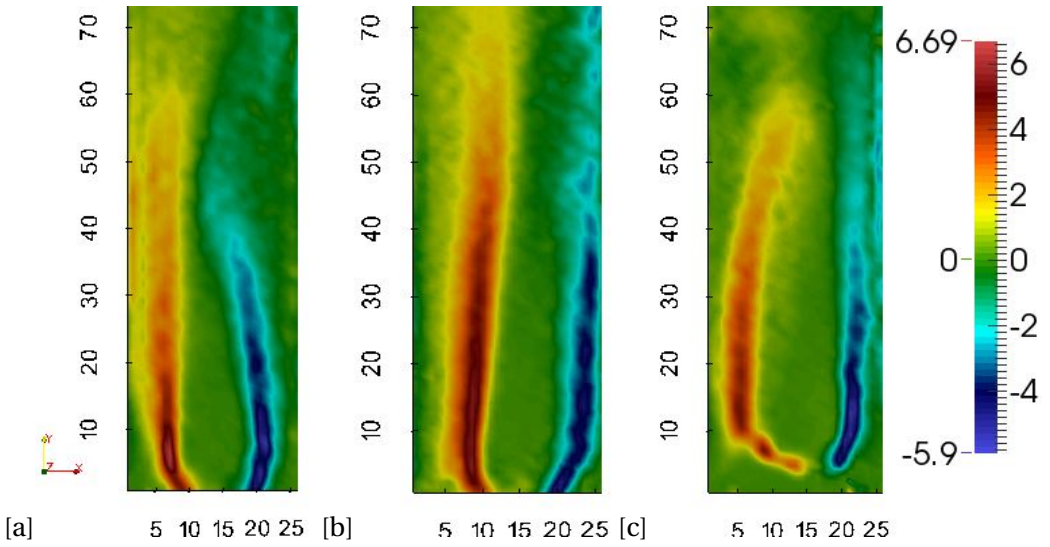

Figure 4.7: Viscous shear stress [Pa] of (a) tissue (b) PV short and the (c) PV tall heart valves at peak flow rate

4.4.3 Reynolds shear stress

The RSS_{maj} results for the tissue, PV short and PV tall heart valves, during peak flow, are shown in Figure 4.8. The maximum RSS_{maj} values are 2600, 2500 and 1200 Pa for the tissue, PV short and PV tall heart valves respectively. The maximum RSS_{maj} occurs in a small region at the heart valve opening for the tissue and PV short heart valves, whereas the maximum RSS_{maj} results for the PV tall heart valve resembled the same pattern as that of the VSS results. All heart valves had a low RSS_{maj} in the central jet where the peak velocity occurs.

The RSS results for the tissue, PV short and PV tall heart valves, during peak flow, are shown in Figure 4.9. The maximum RSS values are -390 Pa, 500 Pa and -380 Pa for the tissue, PV short and PV tall heart valves respectively. Contrary to the RSS_{maj} results above, the maximum RSS values for the tissue and PV tall heart valves occur around the edges of the central jet and not at the heart valve opening. The PV short heart valve had an increase in the RSS value at the heart valve opening, where the same observation was not present for the tissue heart valve. A large difference of approximately one order of magnitude is noticed between the RSS_{maj} and RSS formula. The RSS_{maj} and RSS magnitudes were significantly lower during diastole than in systole, shown in Table 4.1.

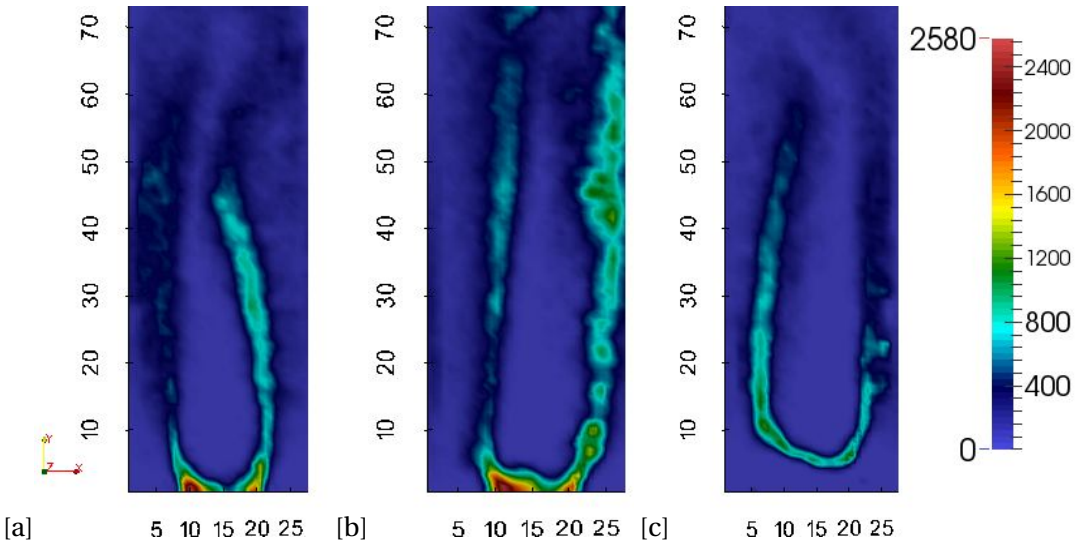

Figure 4.8: Major Reynolds shear stress [Pa] of (a) tissue (b) PV short and the (c) PV tall heart valves at peak flow rate

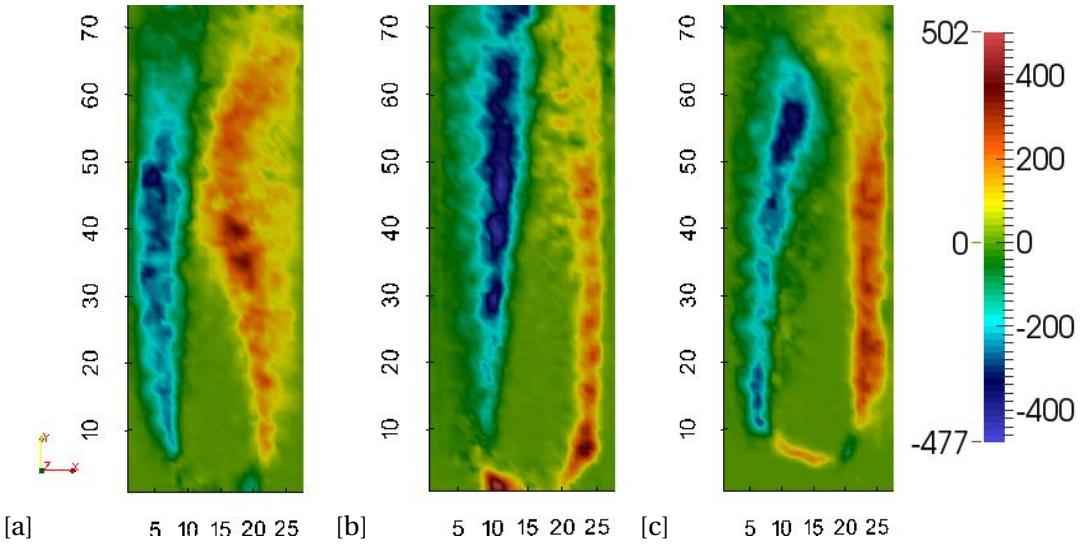

Figure 4.9: Reynolds shear stress [Pa] of (a) tissue (b) PV short and the (c) PV tall heart valves at peak flow rate

By recreating the RSS_{maj} images for the tissue and PV short heart valves with a maximum RSS_{maj} = 1200 Pa (maximum RSS_{maj} for the PV tall heart valve) produces the images in Figure 4.10. The magnitude of the RSS_{maj} throughout the domain changes minimally, with the majority of the maximum RSS_{maj} occurring at the leaflet edges and the edge of the central jet.

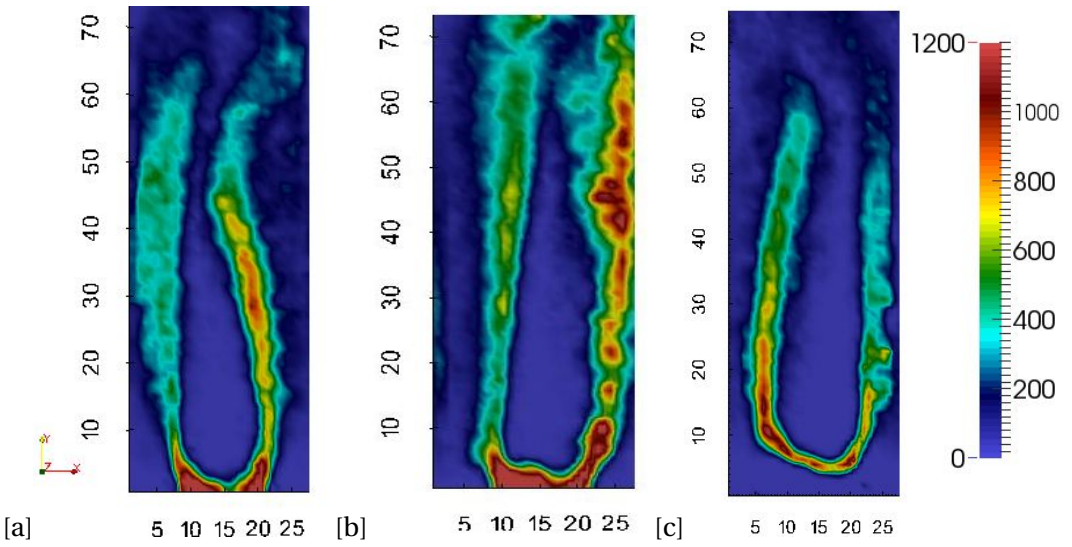

Figure 4.10: RSS_{maj} plot with a maximum RSS_{maj} = 1200 Pa for the (a) tissue, (b) PV short and (c) PV tall heart valve

4.4.4 Turbulent viscous shear stress

The TVSS for the tissue, PV short and PV tall heart valves, during peak flow, are shown in Figure 4.11. The maximum TVSS values were 18.7, 15 and 15 Pa for the tissue, PV short and PV tall heart valves respectively, where the maximum TVSS occurs in the same regions of the velocity field as the VSS. The length of the maximum TVSS regions are approximately identical to the VSS. The TVSS magnitudes were significantly lower during diastole than in systole similar to the VSS, RSS and RSS_{maj}, shown in Table 4.1.

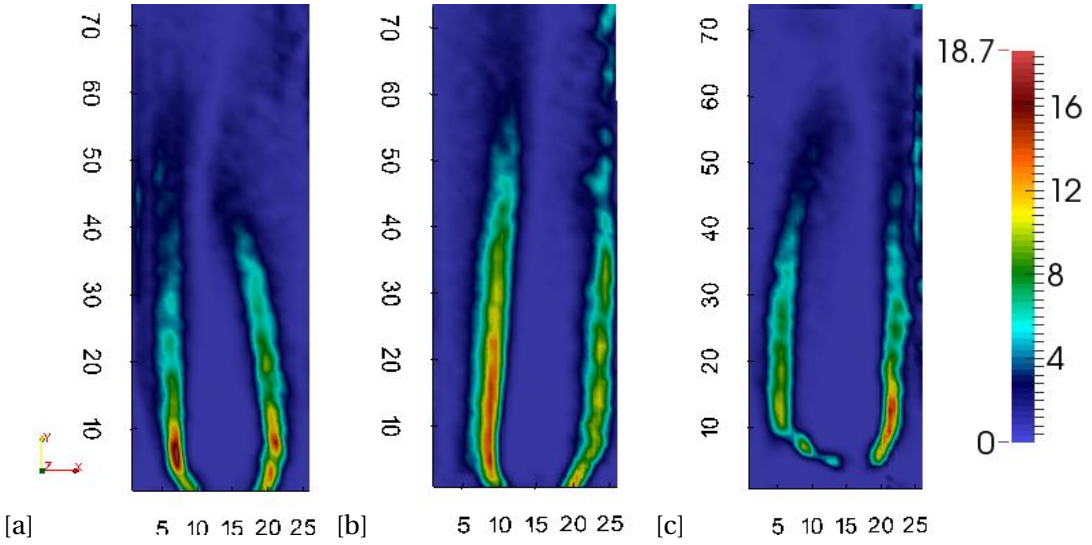

Figure 4.11: Turbulent viscous shear stress [Pa] of (a) tissue (b) PV short and the (c) PV tall heart valves at peak flow rate

4.4.5 Filtered stresses

The filtered RSS_{maj}, RSS, VSS and TVSS are shown in Table 4.2. The RSS magnitude drops dramatically when excluding large velocity fluctuating components of the RSS equation (Equation 2.9). The RSS_{maj} dropped from a maximum of 2600 Pa for the tissue heart valve with no filtering, to a minimum of 180 Pa for the PV tall heart valve for a fluctuating velocity cut-off of 0.75 m/s. Similarly, the RSS values dropped from a maximum of 500 Pa to a minimum of -65 Pa for the PV short heart valve. The VSS and TVSS were less significantly impacted by the filtering.

Table 4.2: Velocity fluctuation filtered results for the RSS_{maj}, RSS, VSS and TVSS

	Tissue			PV Short			PV Tall		
	No Filter	Filter A	Filter B	No Filter	Filter A	Filter B	No Filter	Filter A	Filter B
RSS_{maj}	2600	900	240	2500	760	240	1200	650	180
RSS	-390	-250	-110	500	-240	-65	-380	-260	79
VSS	6.7	7.6	7.5	5.8	6.6	6.3	5.8	6.7	6.4
TVSS	19	23	22	15	21	17	15	19	17

4.5 Discussion

4.5.1 Velocity profiles

Figure 4.3 shows the peak velocity magnitude of the tissue, PV short and PV tall heart valves, which ranged between 4.5 m/s to 5.6 m/s. The peak velocity magnitudes of the heart valves were larger than results from literature. Leo *et al.* [42] reported peak velocity magnitudes of between 2 and 2.4 m/s for 23 mm polymeric heart valves at a CO of 5 L/min at 70 BPM, and Raghav *et al.* [51] reported peak velocity magnitudes up to 2.5 m/s for a 23 mm Carpentier-Edwards Perimount Magna Ease commercial heart valve under the same testing conditions. Saikrishnan *et al.* [110] reported a maximum velocity of 4 m/s for a bicuspid 21 mm, and 2.8 m/s to 3 m/s at peak flow for a trileaflet 21 mm heart valve. Hasler *et al.* [43] found velocities up to 2.1 m/s for a 23 mm Carpentier-Edwards bioprosthetic heart valve at 60 BPM and 72 ml stroke volume. All of the heart valves examined in literature were larger than the heart valves tested in this study, making a direct comparison challenging. Examining the velocity jets from Figure 4.3, the PV short valve had the narrowest central jet, ranging from approximately 10 mm at the heart valve opening to 15 mm at the widest point 8 mm downstream from the heart valve. The narrowing of approximately 10 mm may be the cause of the large peak velocity of 5.6 ms for the PV short heart valve. The tissue heart valve had a wider orifice than the PV short heart valve, however the PV tall heart valve had the widest central jet, ranging from 14 mm at the heart valve opening to 17.5 mm approximately 8 mm from the heart valve opening. Taking into account the heart valves in this study had a diameter of 19 mm, smaller than the heart valves in literature, and the experimental setup of the pulse duplicators vary between this study and literature, the peak velocity results are considered to be accurate in this study.

Both the tissue and PV tall heart valves exhibit a twisting motion of the fluid flow far downstream from the heart valve opening (approximately 40 to 55 mm downstream), however no such behaviour was observed for the PV short heart valve. It may be that the same behaviour occurs much further downstream due to the higher maximum velocity, however this could not be determined as the observation window was cut-off where the downstream tube met the aortic compliance chamber. Changes to the CPD would need to be made to increase the downstream length of the CPD to observe if this phenomena occurs for the PV short heart valve.

The tissue heart valve seemed to exhibit relatively symmetric behaviour of the recirculating flow velocities on either side of the heart valve, with low maximum recirculation flow velocities. Both the PV tall and PV short heart valves had asymmetric reverse flow velocities, where much higher reverse flow was observed to the left of the heart valves behind the free leaflet. The reverse flow observed are due to vortices that form around the leaflet edges, and have been shown to be beneficial to assist in closing the heart valves quickly [8]. A large recirculating flow velocity near the tube walls is not detrimental to the functioning of the heart valve, provided that the EOA and forward flow volume is sufficient, that the percentage RV is low and that the recirculating flow does not cause significantly large VSS to cause hemolysis or platelet activation near the wall. A large velocity near the wall on the right of the heart valve was noticed for the PV short and PV tall heart valves. This could be due to large near wall velocities and uncertainties in determining the exact wall location [111], as well as calibration errors due to the high curvature at the CPD downstream tube near the wall.

The large reverse flow velocity throughout the entire domain of the PV tall heart valve at 500 ms is due to the long closing time, where back flow is required to close the valve. This re-affirms the conclusion from pulse duplication that a larger reverse flow occurs during closing, increasing the closing volume of the PV tall heart valve. The maximum velocity for the PV tall heart valve rapidly decreases (Table 4.1) due to the valve closing and sealing efficiently. The PV short heart valve has a large reverse flow velocity throughout diastole due to the gaps between the heart valve leaflets, a conclusion drawn from the pulse duplication measurements. The observations from the PIV results provides insight into the results obtained during pulse duplication and confirms the conclusions drawn about the functioning of the heart valves from pulse duplication.

4.5.2 Shear stress

The VSS is considered to be the "real" forces felt by the RBCs and platelets and should be the first metric for determining the onset of hemolysis and platelet activation [36]. All of the VSS values were below 10 Pa, considered to be the minimum threshold for platelet activation [36]. Studies have also shown that the time that the platelets are under stress impacts the amount of platelet activation, where a thorough summary of VSS and RSS values of hemolysis and platelet activation is provided in Ge *et al.* [36]; Li *et al.* [44]; Yen *et al.* [45]. The length of time that particles were exposed to high levels of shear stress was not determined with PIV in this study, however the length of the largest VSS region was determined in order to approximate the amount of damage to RBCs and platelets.

The tissue heart valve had the smallest maximum VSS length, followed by the PV tall and PV short heart valves, potentially indicating less damage to RBCs and platelets for the tissue heart valve. Retta *et al.* [21] recommend that all new heart valves are tested against commercial heart valves to serve as a *non inferiority* test when performing pulse duplication. The same methodology can be extended to PIV experiments as tissue heart valves are known to resist hemolysis and platelet activation, therefore providing a suitable PIV comparison for any new heart valve design.

The maximum RSS_{maj} values, shown in Figure 4.8, occured in the orifice opening of the heart valves. A similar observation as found in Raghav *et al.* [51]; Del Gaudio *et al.* [33]; Li *et al.* [44], albeit at much lower RSS_{maj} values. Raghav *et al.* [51] state that larger RSS near the leaflet edges are expected due to leaflet flutter during systole. The maximum RSS_{maj} values are well above the minimum threshold for both hemolysis and platelet activation, generally considered to be between 600 Pa - 800 Pa [36] and 517 Pa [45] for hemolysis. The maximum RSS values are shown in Figure 4.9 and are approximately an order of magnitude lower than the RSS_{maj}. The RSS profile of the valves are similar in shape and magnitude to Leo *et al.* [42], where a maximum RSS of 5180 dyn/cm^2, equivalent to 518 Pa occurred at peak systole for a 23 mm polymeric heart valve. The dynamic nature of the opening and closing of the heart valves may potentially cause the large RSS_{maj} values in Figure 4.8. Adjusting the maximum value of the RSS_{maj} in the legend plot reveals that the majority of the flow region, even in the central jet downstream of the heart valve leaflets, is below the 800 Pa threshold.

The RSS is not a real measure of the forces experienced by the RBCs and platelets, but is instead a statistical average of the fluctuation of the velocity. Several studies have been performed where either the RSS_{maj} or RSS was used as a shear stress metric [36; 33; 51; 44; 42]. There is very little data on the PIV results of 19 mm heart valves, and the heart valves tested in the literature were larger than the heart valves tested in this thesis. The lack of data makes it difficult to draw a conclusion on the accuracy of the RSS_{maj} and RSS results presented in this study. The difference in heart valve sizes and the experimental setup makes it difficult to compare results from various studies, where the setup alone may impact results significantly [21]. Due to the results found in this study, when using either the RSS or RSS_{maj} as a metric for platelet activation or hemolysis, it is recommended that the other metric is simultaneously performed to check for large discrepancies between the two metrics.

The TVSS pattern follows that of the VSS pattern, where the maximum TVSS occurs in the same region and is approximately the same length as the maximum VSS regions. This is due to the TVSS being determined from the measured velocity gradients, with sub-grid scale models to model the forces on the smallest of length scales. According to Yen *et al.* [45], hemolysis will occur for a TVSS of 60 Pa, however no minimum threshold for platelet activation using the TVSS metric was provided. In the absence of a TVSS threshold limit for platelet activation, the VSS magnitude threshold was used. The TVSS attempts to model the VSS on the subgrid scale smaller than the spatial resolution of the PIV experiments, by using the energy present in the small scales that are not resolved on the grid size. If the VSS threshold is used to determine platelet activation, all three heart valves would potentially induce platelet activation.

The maximum RSS, RSS_{maj} and TVSS throughout diastole was minimal when compared to peak systole. All shear stress metrics were well below any threshold for either platelet activation or hemolysis. The region where the largest velocity gradients would occur during diastole are at the leaflet edges inside the heart valve once the leaflets are closed. It was not possible to perform PIV in these regions, and the CPD and valves would need to be re-designed to perform PIV at the leaflet edges for the polyurethane valves. Due to the non transparent pericardium tissue, it may not be possible to perform 2D PIV in this region for the tissue heart valve.

In order to increase the accuracy and reliability of the PIV results, a grid independence study similar to that in Ge *et al.* [36] can be performed. Grid independance was attempted for the PIV experiments but it was found that decreasing the observation windows from 32 x 32 to 16 x 16 pixels introduced errors in the velocity vector measurements. Accurately determining the velocity on finer PIV grids would need to be investigated before attempting to perform shear stress comparisons on finer PIV grids, either by re-examining the CPD viewing windows, calibration technique or particle seeding.

4.5.3 Filtered shear stresses

The filters used for the calculation of the RSS, VSS and TVSS (Filter A and Filter B) were implemented by selecting the data sets based on the velocity fluctuations, described in Section 4.4.5. The method of filtering the $u^{'}$ velocity components is similar to discarding outliers from the mean value of a large data set. The purpose of the filtering was to determine whether discarding "outliers" from the velocity fluctuations has an impact on the RSS and RSS_{maj} magnitudes. For Filter A, the velocity fluctuating component had to be within 1.5 m/s of the mean velocity magnitude to be selected, whereas for Filter B the velocity fluctuating component had to be within 0.75 m/s of the mean velocity magnitude. The filters reduced the magnitude of the average $\overline{u}^{'}$ and $\overline{v}^{'}$ values, which reduced the magnitude of the RSS_{maj} and RSS values. However the VSS and TVSS increased when the filters were applied, indicating that the VSS and TVSS are less sensitive to the cycle to cycle variation.

4.6 Conclusion

PIV was performed during systole and diastole for the tissue, PV short and PV tall heart valves. The velocity profiles showed that the small orifice area of the PV short valve results in large velocities during peak systole, and that leakage throughout diastole is present for the PV short heart valve in line with the pulse duplication findings. The tissue valve had adequate performance in terms of the velocity magnitude and distribution, especially during diastole where very small velocity magnitudes were observed, once again in line with the low leakage volume findings from pulse duplication. The PV tall heart valve showed a large velocity magnitude during early diastole as the heart valve takes longer to close than the tissue and PV short heart valve. However, the velocity magnitude during diastole decreases below that of the PV short heart valve at the end of

closing, reducing the leakage volume of the PV tall heart valve.

The VSS for all three heart valves were below the minimum threshold for platelet activation and hemolysis. The RSS_{maj} results were much larger than the minimum threshold for platelet activation and hemolysis. The RSS values were below the hemolysis threshold limit and an order of magnitude lower than the RSS_{maj}. The SGS modelling for the TVSS accounted for the energy present in the smaller turbulent eddies. The TVSS method provided a more accurate means of determining the real forces on the RBCs and platelets in the small scale vortices, and indicated a larger potential for platelet activation around the central jet when compared to the VSS. More research on determining the TVSS threshold limits for hemolysis, and especially platelet activation is required.

Chapter 5

Numerical Simulation

Chapter 5 describes the numerical procedures to evaluate heart valves using FSI simulations. Section 5.1 describes the simulation methodology and layout of the simulation procedure. Section 5.2 describes the numerical simulation setup, geometry, boundary conditions and meshing. Section 5.3 and 5.4.1 describe the software development necessary to enable FSI simulations using open-source software and the FSI software validation. The results of the mesh independence, solver coupling and heart valves are provided in Section 5.4, followed by a discussions in Section 5.5.

5.1 Methodology

The steps used to perform the numerical simulations are shown in Figure 5.1. Laminar flow simulations were performed for the entire fluid simulation until closing of the valve, whereas turbulent model simulations were only performed after valve opening. Turbulent models were run at a throat Reynolds number larger than $Re = 2600$, as laminar simulations were shown to be more accurate for $Re < 2600$ [108]. The throat Reynolds number was defined as $Re = \frac{DV\rho}{\mu}$, where D is the throat diameter, V is the average pipe velocity, ρ is the fluid density (1050 kg/m^3) and μ is the fluid viscosity (0.0035 Ns/m^2). The coarse, medium and fine fluid and solid meshes were run to perform a mesh independence study, as well as a combination of the mesh sizes to determine the impact of the mesh sizes on the simulation coupling results. All simulations were performed on an Intel Xeon E5-2609, 1.9 GHz, with 16GB RAM running Ubuntu 14.04 LTS.

All numerical simulations were performed using foam-extend-3.2 [112] (referred to as openFOAM) for the fluid domain simulations with the FOAM-FSI adaption from Blom [113], CalculiX [114] for the solid domain simulations and preCICE [115] to couple openFOAM and CalculiX together. During the simulation procedure, once the fluid domain had significant distortion of the mesh, the domain was remeshed according to the remeshing procedure discussed in Algorithm 4. The displaced solid domain in CalculiX was exported as an *stl* file and used as an input in the fluid domain remeshing with cfMesh. The output restart file of CalculiX, *valve.rout*, was saved as *valve.rin* to be used in an input file to restart CalculiX. The new openFOAM simulation's start time was changed to continue the from the last time step of the previous simulation.

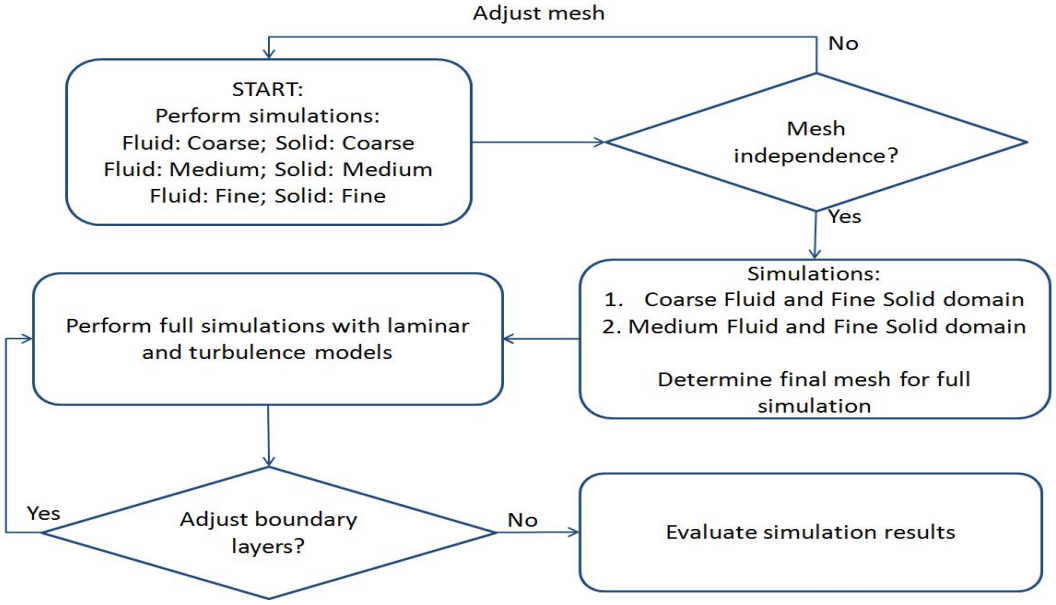

Figure 5.1: Simulation flow chart process for the numerical simulation procedure

Algorithm 4 openFOAM remeshing procedure

procedure
simulation end
display displacement at final time step view final displacement
Export final displacement as an *stl* file
copy the *stl* to *cfMesh* meshing directory
replace the previous interface *stl* with the new displaced interface *stl* from CalculiX
remesh using new *stl* boundary file
copy the new mesh to a new openFOAM simulation directory
change the relevant simulation parameters to restart the simulation from the new directory
perform a consistent field map to map the field variables from the old mesh to the new mesh
Change directory in *config.yml* to ensure the restart CalculiX file points to the correct *precice-config.xml* file as the new simulation is in a new directory

In order to accurately determine the WSS when utilising turbulence models, the wall y^+ values need to be within a certain range, depending on whether the flow was integrated through boundary layer or resolved through to the wall. Turbulence models that resolve through the boundary layer have been shown to be reasonably accurate for confined flows in medical type devices [111; 108]. The potential presence of flow separation and wall reattachment makes the $\kappa-\omega\ SST$ model resolving through the boundary layer more attractive than the $\kappa-\epsilon$ type turbulent models that integrate through the boundary layer. In this study, the $\kappa-\omega\ SST$ turbulence model was utilised resolving through the

boundary layer. Wall functions integrating through the boundary layer were not utilised in this study as the mesh elements near the wall would need to be increased to attain the correct y^+ size. Increasing the near wall mesh elements would make the mesh too coarse, potentially affecting the pressure across the heart valve.

5.2 Numerical simulation setup

5.2.1 Geometry

The geometry of the heart valve was generated using Autodesk Inventor Professionalő 2016 using a method similar to that in Thubrikar [116]. A simple tube was constructed from the PIV tube dimensions and the heart valve geometry was placed inside the tube, shown in Figure 5.2. Simplifications were made with the attachment of the heart valve to the frame and tube, where the titanium frame was set to the same thickness of the leaflets in order to ensure that there was no pinching of the mesh between the leaflets and the frame during opening and closing. A narrow throat was used to mimic the narrowing upstream of the valve due to the plastic retainer and sewing ring used to hold the valve in the CPD. The sinus regions of the aorta were not included in the design to ensure geometric correspondence between the simulation and PIV experiment.

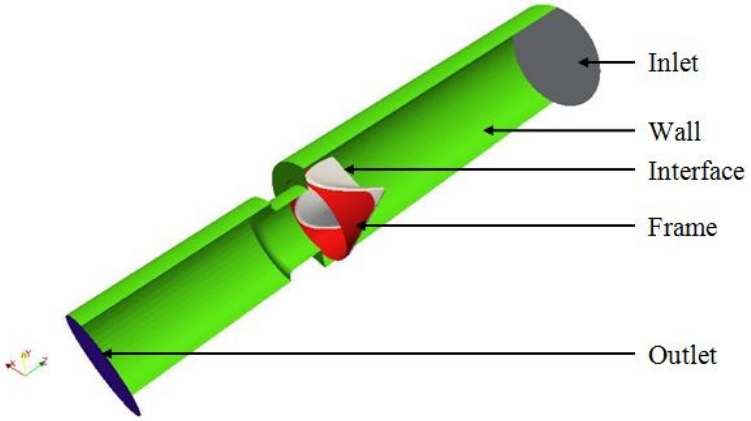

Figure 5.2: Geometry of simulated heart valve domain

5.2.2 Boundary conditions

The correct boundary conditions are important in achieving accurate simulation results. The boundary conditions applied on each patch are shown in Table 5.1. The volumetric flow rate was specified at the inlet based on the experimental volumetric flow rate of the pulse duplicator pump and not the experimentally measured flow rate through the heart valve itself. This was done to ensure that the simulation input settings were independent of the heart valve or specific VIA settings used during pulse duplication testing. The velocity on the wall and heart valve frame was set to zero for the no-slip condition. For internal flow problems under turbulent conditions, the correct turbulent intensity, I, needs to be calculated to determine the turbulent kinetic energy, κ, for the $\kappa-\omega$ SST model. The turbulent intensity is determined from the pipe Reynolds number [117; 118]

$$I = 0.16 Re_L^{-\frac{1}{8}} \tag{5.1}$$

where Re_L is the pipe Reynolds number. The turbulent kinetic energy is then determined by

$$k = \frac{1}{2}(UI)^2 \tag{5.2}$$

Where U is the mean pipe flow velocity. The specific dissipation rate ω was calculated by

$$w = C_\mu^{-\frac{1}{4}} \frac{\sqrt{k}}{l} \tag{5.3}$$

where $l = 0.07D$ and $C_\mu = 0.09$ is a constant.

Table 5.1: openFOAM simulation boundary conditions

Property	Inlet	Outlet	Wall/Frame	Interface
Velocity	Time Varying	Zero Gradient	Fixed Value	Moving Wall
Pressure	Zero Gradient	Fixed Value	Zero Gradient	Zero Gradient
Turbulent Kinetic Energy (κ)	Fixed Value	Inlet Outlet	Fixed Value	Fixed Value
Specific Dissipation Rate (ω)	Omega Wall Function	Omega Wall Function	Omega Wall Function	Omega Wall Function

The solid domain was fixed (displacements set to zero) at the intersection of the leaflets with the fixed frame in order to model the attachment of the heart valve leaflets to the titanium frame. The forces in the x, y and z direction for the moving interface were initialised as zero for the preCICE coupler with CalculiX. This was to ensure that no spurious forces cause instability during the simulation initialisation with preCICE.

5.2.3 Meshing

The fluid mesh for the coarse, medium and fine domains are shown in Figure 5.3. The meshes were generated using cfMesh available within foam-extend-3.2. The mesh sizes were generated by reducing the size of the mesh throughout the domain, as well as by refining the mesh around the heart valve leaflets. The solid mesh for the coarse, medium and fine domains are shown in Figure 5.4. The solid mesh was created using a STEP file of the heart valve leaflets only and meshed using second order tetrahedral elements in SALOME.

The mesh sizes for the coarse, medium and fine mesh for the fluid domain are shown in Table 5.2. The fluid domain was remeshed during opening, where $Step$ 1 represents the mesh for a simulation time of 0 to 10 ms, $Step$ 2 represents the mesh for a simulation time of 10 to 25 ms, and $Step$ 3 represents the mesh for a simulation time of 25 to 31 ms.

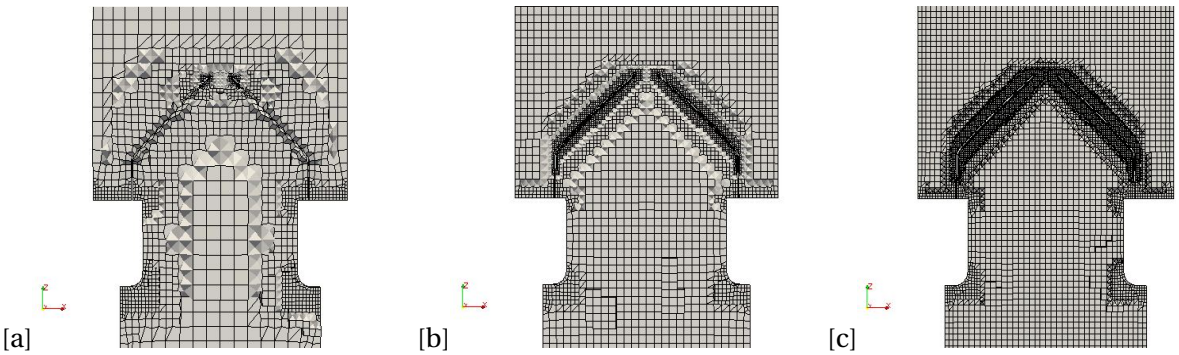

Figure 5.3: Mesh for the (a) coarse, (b) medium and (c) fine fluid domain at time 0 ms

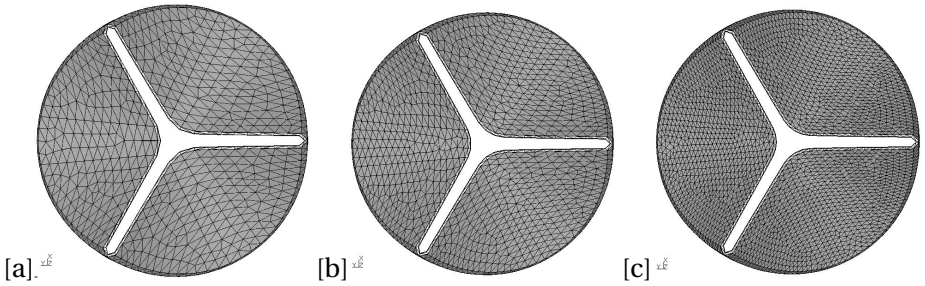

Figure 5.4: Mesh for the (a) coarse, (b) medium and (c) fine solid domain at time 0 ms

Table 5.2: Number of cells and points for the coarse, medium and fine mesh before and after remeshing of the fluid domain

	Fluid Cells			Fluid Points		
	Coarse	Medium	Fine	Coarse	Medium	Fine
Step 1	189149	495619	1043197	135582	384266	846326
Step 2	238475	569743	1057859	171293	445388	849111
Step 3		576193			443730	

5.3 Software development

The preCICE adapters for openFOAM and CalculiX had been developed prior to the beginning of this study, however they were not able to perform the FSI simulations with remeshing. Software changes were required to add stability to the CalculiX adapter during simulation restarts, as well as to the mesh motion solver of openFOAM.

During a restart, the CalculiX simulation would diverge during the first iteration of the first time step. Examining the source code of CalculiX showed that the force vector array was altered by the preCICE adapter during the initialisation process. The mesh motion algorithm within openFOAM quickly ran into memory problems with approximately 10 000 boundary points used in the RBF interpolation matrix, and required a

more in depth analysis of the source code. A description of the software changes to both openFOAM and CalculiX is given in Appendix D.1.

5.4 Results

5.4.1 FSI coupling validation

A simple wave propagation through tube and beam in cross flow simulations were simulated to verify that the coupled solvers work correctly after implementing the CalculiX stability changes and the RBF mesh motion solver change. The results from the test cases are given in Appendix E. A wave propagation through a tube and a beam in cross flow where completed for the FSI validation.

5.4.2 Mesh independence and mesh motion analysis

The mesh independence study for both openFOAM and CalculiX is provided in Appendix F.1. Mesh independence was achieved for fine solid mesh and the medium fluid mesh. The nearest neighbour data mapping scheme was used as the RBF mapping was too expensive to compute for the problem size on current computational resources. The fluid pressure and heart valve leaflet interface velocity were used for mesh independence. An analysis of the mesh motion performance using the RBF mesh motion solver, combined with remeshing is shown in Appendix F.2.

5.4.3 Solver coupling

The difference in the number of iterations per timestep between the Aitken and IQN-ILS coupling schemes was examined for the coarse, medium and fine mesh and the results displayed in Figure 5.5 and Figure 5.6. The IQN-ILS method clearly out performs the Aitken under-relaxation scheme, significantly reducing the simulation time. This is especially important if a large number of iterations are performed without restarting a simulation, such as a case where the heart valve was fully opened and performed up to 400 time steps.

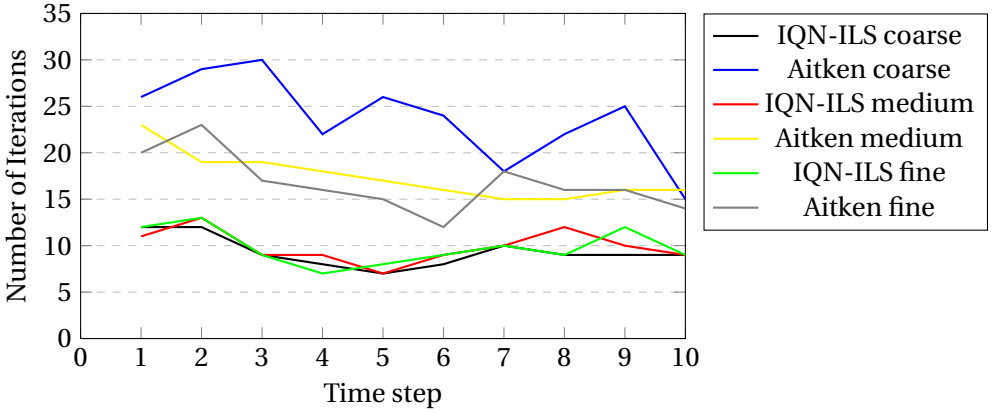

Figure 5.5: Numerical coupling results for the coarse, medium and fine mesh using the Aitken relaxation and IQN-ILS coupling for the first simulation without a restart

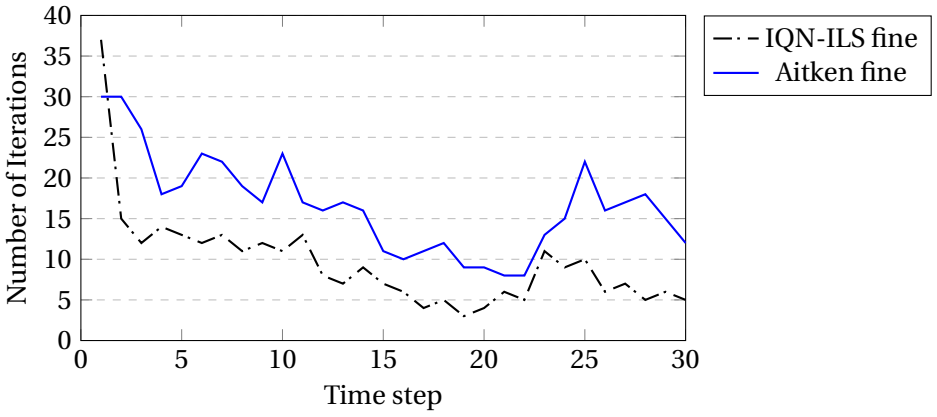

Figure 5.6: Numerical coupling results for the medium mesh using the Aitken relaxation and IQN-ILS coupling after a simulation restart

5.4.4 Pulse duplication

A comparison between the experimental, laminar flow simulation and turbulent flow simulation pressure drop is shown in Figure 5.7. The simulations had a much lower pressure drop during the first 60 ms of the cardiac cycle. The simulation pressure drop dipped at approximately 20 ms which correlated with the change in volumetric flow rate gradient shown in Figure 5.8. The peak pressure drop for the laminar and turbulent flow simulations match closely with the second peak of the experimental pressure drop. The simulation pressure drop decreases steadily with time after approximately 70 ms, however the laminar flow simulation spikes again at approximately 140 ms whereas the turbulent flow simulation does not.

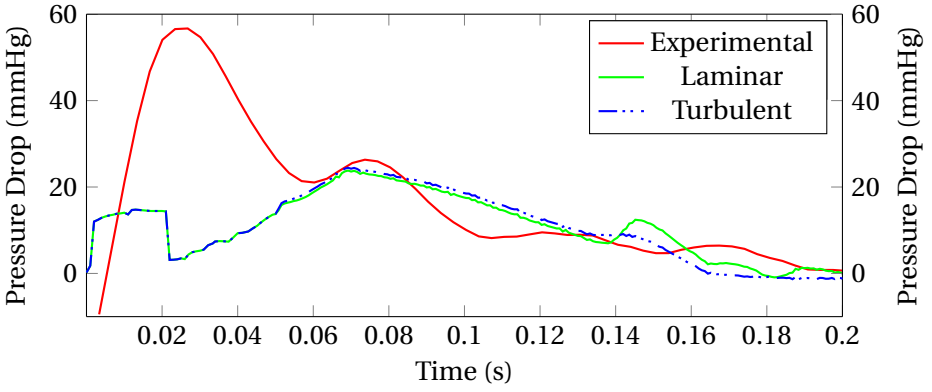

Figure 5.7: Experimental, laminar flow simulation and turbulent flow simulation pressure drop

The experimental volumetric flow remains zero until approximately 40 ms, where a sharp rise occurs until the peak volumetric flow rate of 24 L/min occurs at approximately 125 ms. The simulation volumetric flow rate had a change in gradient at approximately

20 ms and continues smoothly to a peak of 27 L/min at 120 ms. The experimental average pressure drop was obtained from the ViVitro CPD and calculated from the raw data using two methods, whereas the simulation average pressure drop was obtained only from the following two methods:

- Method 1: averaging the pressure drop from the start of the positive pressure drop interval until the pressure drop becomes zero
- Method 2: averaging the pressure drop from the second peak for the experimental results or from the maximum peak for the simulations until the pressure drop becomes zero

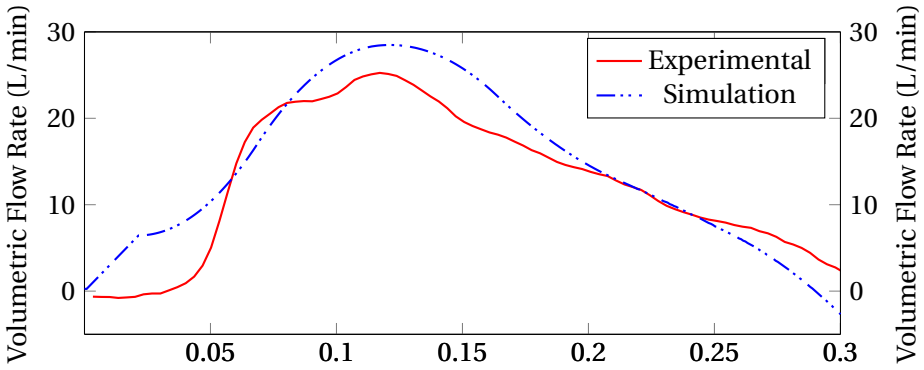

Figure 5.8: Experimental and simulation volumetric flow rate

The experimental and numerical average pressure drop is summarised in Table 5.3. The experimental pressure drop for method 2 (7.32 mmHg) was lower than method 1 (15.18 mmHg), where the experimentally measured average pressure drop form the ViVitro CPD was 15.28 mmHg. Examining only method 1 further, the turbulent average pressure drop (13.49 mmHg) was closer to the experimentally measured average pressure drop (15.28 mmHg) than the laminar flow simulation (12.53 mmHg).

Table 5.3: Experimental and simulation average pressure drop for the PV tall heart valve

	Average Pressure Drop [mmHg]		
	Experiment	Laminar	Turbulent
Method 1	15.18	12.53	13.49
Method 2	7.32	12.40	13.80
ViVitro	15.28	-	-

In order to quantify the error between the numerical and experimental results, the RMS error, correlation coefficient and coefficient of determination for the pressure drop and volumetric flow rate is shown in Table 5.4. The errors were determined for the full data set (starting from time 0 s) and the half data set (starting from second experimental peak time) for the pressure drop. The half data set RMS error was lower that the full

data set RMS error, as the error during the first 50 ms simulation time is not accounted for. The correlation coefficient is closer to 1 for the half data set than the full data set, indicating a better correlation when only the half data set is used. This is confirmed by the larger coefficient of determination for the half data set. The simulation procedure was able to determine to pressure drop from 50 ms and onwards only. The volumetric flow rate coefficient of determination was 0.859, indicating a reasonable agreement between the numerical model and experimental results. The turbulent simulation volumetric flow rate error is the same as the laminar flow simulation error.

Table 5.4: Comparison of the error measurements for the pulse duplicator pressure drop and volumetric flow rate with the numerical simulation results

			Pressure Drop [mmHg]		Volumetric Flow Rate [L/min]
	Measure of Error	Symbol	Full Data Set	Half Data Set	
Laminar	RMS Error	RMS	15.66	4.044	4.79
	Correlation Coefficient	r	0.394	0.885	0.881
	Coefficient of determination	R^2	0.154	0.778	0.859
Turbulent	RMS Error	RMS	15.73	4.401	
	Correlation Coefficient	r	0.403	0.885	
	Coefficient of determination	R^2	0.162	0.784	

The Bland-Altman plot for the laminar (squares) and turbulent (plus) flow simulations compared to the experimental pressure drop is shown in Figure 5.9. The Bland-Altman plot shows a large confidence interval of 28.67 mmHg. The majority of the results situated near the mean difference line occur for low experimental pressure drop values, with a consistent rise in the difference as the experimental pressure drop increases. The numerical model over-predicts the pressure drop when compared to the experimental results. The Bland-Altman plot for the simulation volumetric flow rate input and experimentally measured volumetric flow rate is shown in Figure 5.10. The majority of points situated near the mean difference line occur for large volumetric flow rates, whereas significant deviation occurs during low volumetric flow rates. The numerical model over-predicts the volumetric flow rate when compared to the experimental results as the majority of points lie beneath the mean difference line.

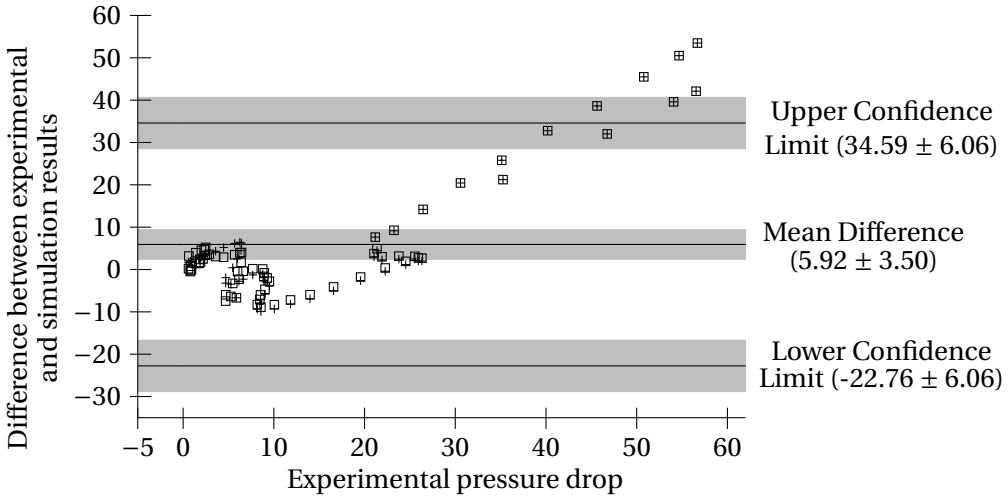

Figure 5.9: Bland-Altman plot of the laminar and turbulent flow simulation pressure drop versus the experimental pressure drop

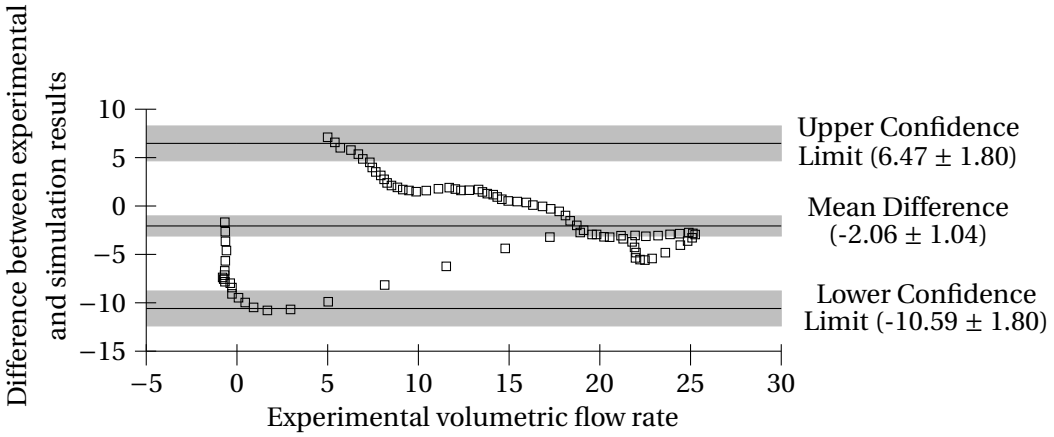

Figure 5.10: Bland-Altman plot of the simulation volumetric flow rate versus the experimental volumetric flow rate

5.4.5 Velocity

The velocity profiles through the PV tall heart valve for the laminar and turbulent flow simulations were compared to the experimental velocity profile at 100 ms into the cardiac cycle in Figure 5.11. The experimental velocity magnitude of 2.66 m/s was much larger than the simulation results of approximately 1.9 m/s. The width of the experimental velocity jet was approximately 12 mm at 100 ms, which was smaller than the simulation results velocity jet of approximately 16 mm. The velocity profiles at peak velocity are shown in Figure 5.12. The experimental velocity reached a maximum velocity of 4.5 m/s, where the laminar and turbulent simulations had a maximum velocity of 2.86 m/s and

2.69 m/s respectively. The width of the velocity jet at the heart valve orifice was approximately 17 mm for the experimental and simulation results. The experimental velocity jet narrowed significantly approximately 40 mm downstream of the heart valve.

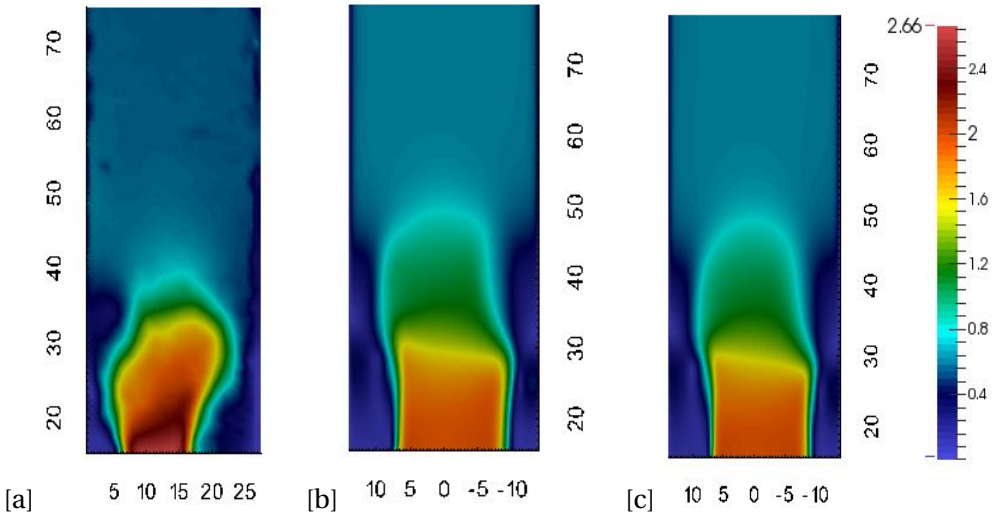

Figure 5.11: Comparison of the velocity profiles at 100 ms into the cardiac cycle for the (a) experimental, (b) laminar flow and (c) turbulent flow simulations

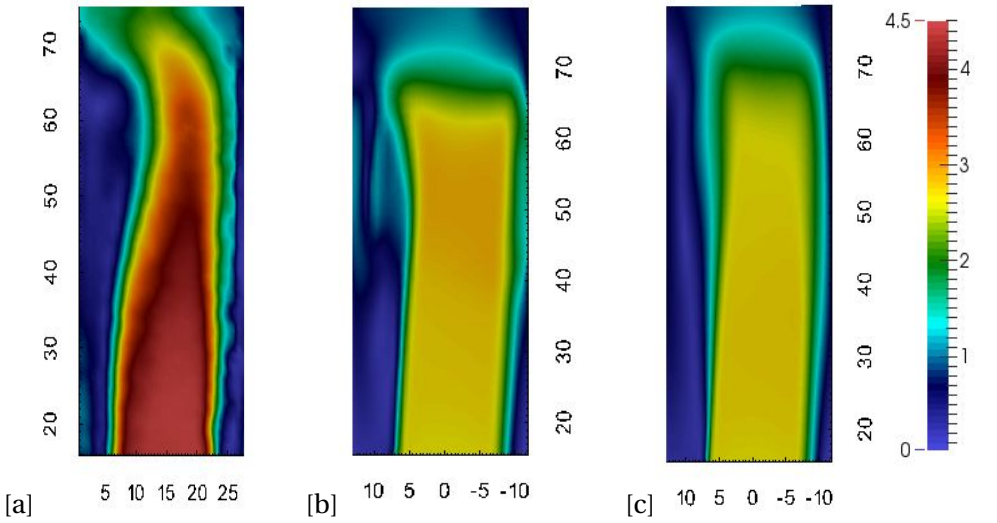

Figure 5.12: Comparison of the velocity profiles at peak velocity for the (a) experimental, (b) laminar flow and (c) turbulent flow simulations

5.4.6 Viscous shear stress

The VSS profiles through the PV tall heart valve for the laminar and turbulent flow simulations was compared to the experimental VSS profile at 100 ms and peak velocity in Figure 5.13 and Figure 5.14 respectively.

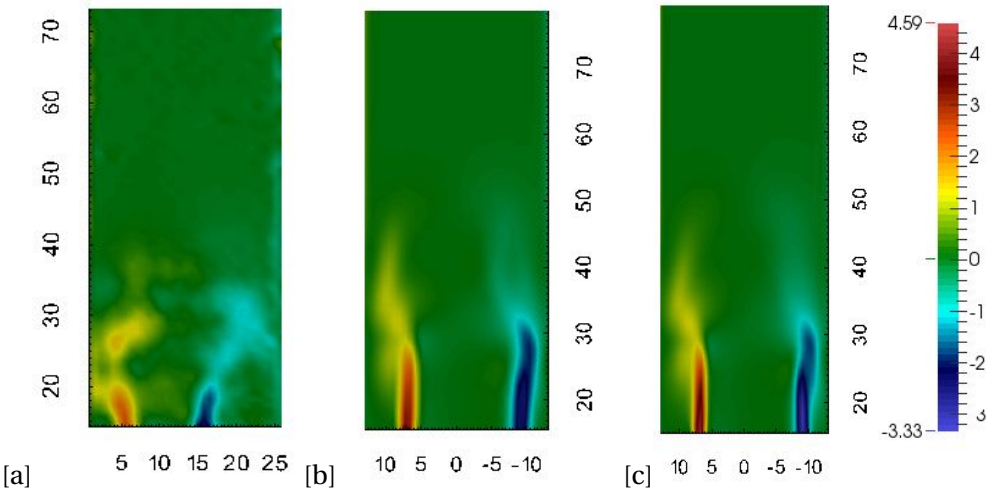

Figure 5.13: Comparison of the VSS profiles at 100 ms into the cardiac cycle for the (a) experimental, (b) laminar flow and (c) turbulent flow simulations

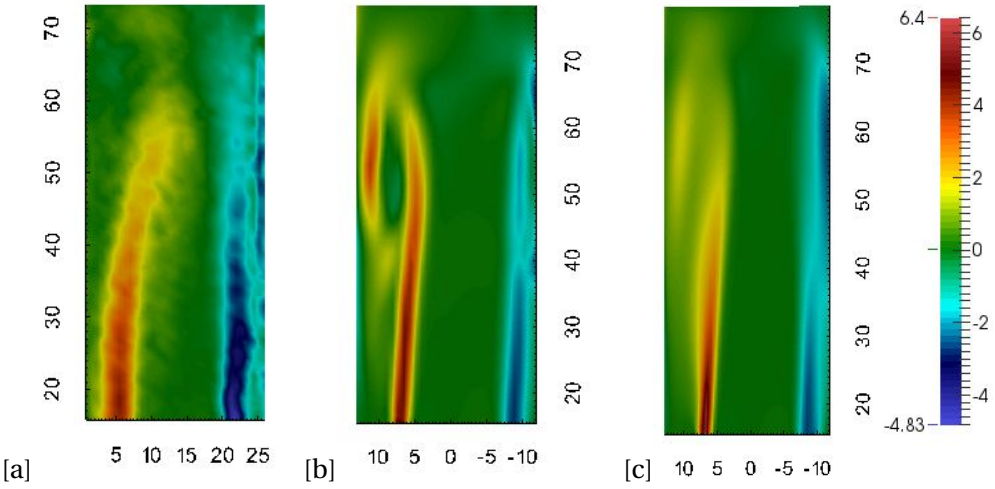

Figure 5.14: Comparison of the VSS profiles at peak velocity for the (a) experimental, (b) laminar flow and (c) turbulent flow simulations

At 100 ms, the experimental VSS jets were closer together than the simulation VSS jets. At peak velocity, the maximum experimental VSS was 6.69 Pa, whereas the maximum simulation VSS was 6.4 Pa and 6.32 Pa for the laminar and turbulent simulation respectively. Once again as with the PIV results, the absolute value of the VSS is important. At peak velocity, each VSS jet of the experimental results were thicker than the VSS jets of the simulation results.

5.4.7 Wall shear stress

As described in Section 2.5, $y^+ < 5$ can be used for near wall modelling resolving through the boundary layer, however $y^+ < 1$ is preferred and $y^+ > 30$ is required to use wall func-

tions that integrate through the boundary layer. A critical aspect of the moving interface is the first cell layer height, as mesh deformation can quickly decrease cell quality and cause the simulation to diverge. A second challenge with FSI modelling with turbulence models was the impact that the boundary conditions had on the results. For a turbulent kinetic energy, κ, on the moving interface of $1x10^{-9}$, the simulation diverged after 23.5 ms of simulated time, whereas the simulation ran to completion when $\kappa = 1x10^{-5}$ was used. Two simulations were performed to test the impact the turbulent kinetic energy boundary condition had on the WSS, where Sim 1 had $\kappa = 1x10^{-5}$ and Sim 2 had $\kappa = 1x10^{-9}$ (Table 5.5).

Table 5.5: Comparison of y^+ and wall shear stress at various time steps for two simulations with different boundary conditions

	Time (s)	0.054	0.058	0.062	0.066	0.07	0.0725
y^+	Sim 1	2.13	2.07	2.11	2.36	2.55	2.61
	Sim 2	1.97	2.05	2.1	2.28	2.46	2.49
WSS	Sim 1	139	101	96	106	142	156
	Sim 2	146	105	108	130	144	159

Sim 2 only ran from 50 ms to 73.5 ms before the solid simulation diverged. Decreasing the time step and increasing the fluid convergence criteria for each coupling iteration had no impact on the coupling divergence. The difference in the WSS between Sim 1 and Sim 2 was determined to evaluate the impact of the boundary condition on the WSS results. Figure 5.15 compared the y^+ values for Sim 1 and Sim 2 at 70 ms into the simulation. The large y^+ values occur near the tips of the heart valve leaflet.

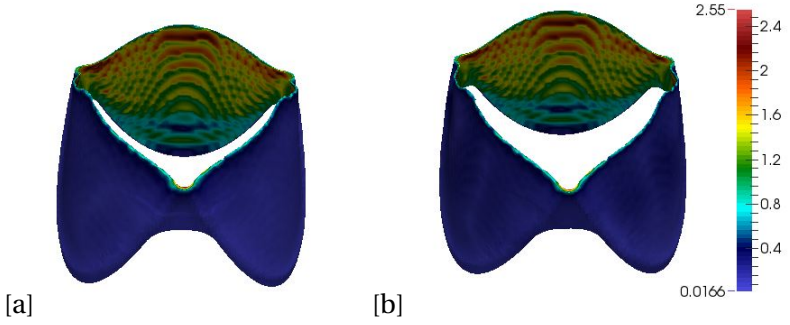

Figure 5.15: Comparison of the heart valve leaflets wall maximum y^+ value for (a) Sim 1 and (b) Sim 2

The WSS at the tip of the heart valve leaflet is shown in Figure 5.16. On examination of the WSS on the leaflets, the peak WSS occurs at small locations along the leaflet tip only. By displaying the surface mesh, the peak WSS occurs between two mesh elements.

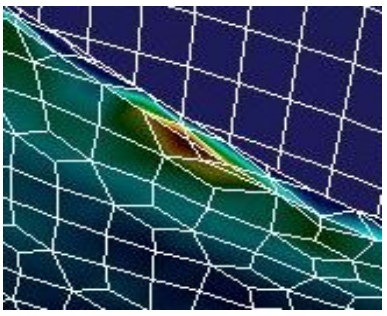

Figure 5.16: Wall shear stress peak value at the leaflet edge

Figure 5.17 shows the WSS where the maximum value is set to 40 Pa. The area with the largest WSS is located only near the leaflet edges. Examining Table 5.5, the the WSS difference between Sim 1 and Sim 2 increases as the velocity magnitude increases. Therefore at larger flow rates, the WSS error may increase due to the turbulent kinetic energy boundary condition.

The WSS was plotted from before the sudden contraction until after the heart valve leaflet tips, for the laminar and turbulent simulations as shown in Figure 5.18 and Figure 5.19 at 100 ms and peak velocity respectively. As the maximum WSS may be distorted due to the mesh quality at specific locations, the maximum WSS in the figure legend was set to the maximum WSS at the curved contraction upstream of the heart valve leaflets. At 100 ms, the turbulent simulation had a larger WSS of 130 versus 117 Pa for the laminar flow simulation. At peak velocity, the turbulent simulation had a larger WSS of 183 versus 165 Pa for the laminar flow simulation. The WSS across the heart valve leaflets was lower than the WSS at the sudden contraction, apart from the small locations of large WSS regions (Figure 5.16). Examining the inside of the heart valve leaflets, the WSS on the upper half of the leaflets is between 40 and 60 Pa, well above the platelet activation threshold of 10 Pa.

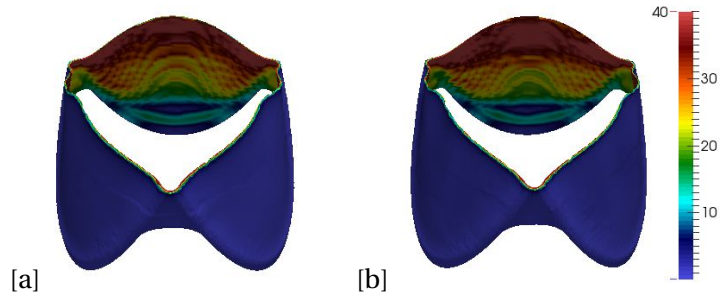

Figure 5.17: Comparison of the heart valve leaflets wall shear stress with a maximum of 40 Pa for (a) Sim 1 and (b) Sim 2

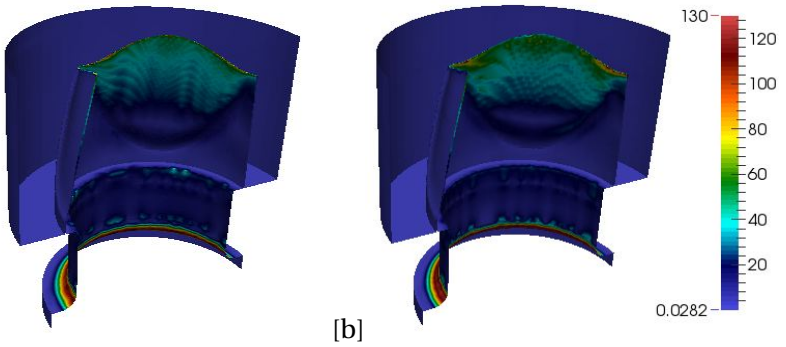

Figure 5.18: Comparison of the wall shear stress profiles at 100 ms into the cardiac cycle for the (a) laminar flow and (b) turbulent flow simulations

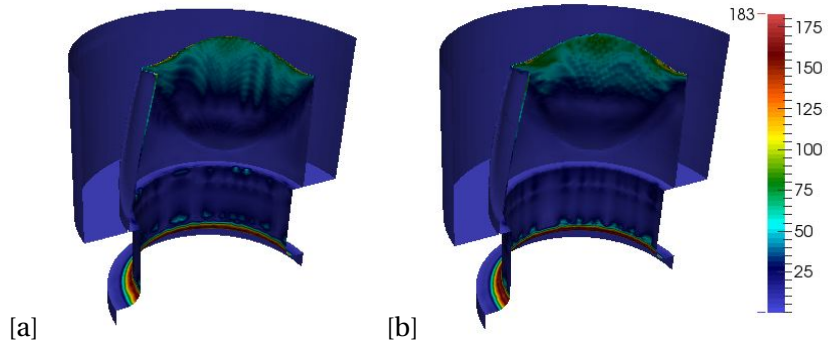

Figure 5.19: Comparison of the wall shear stress profiles at peak velocity for the (a) laminar flow and (b) turbulent flow simulations

5.4.8 Solid displacement

The displacement of the heart valve leaflets during opening is shown in Figure 5.20. A maximum displacement of 6.84 mm occurred at the tip of the heart valve leaflet at 110ms into the cardiac cycle. All leaflets extend radially outwards until approximately 31 ms (Figure 5.20c). One half of the leaflet begins to move towards the centre (inward facing arrows in Figure 5.20d) of the heart valve whilst the other half continues outwards. Once one half of the leaflet has moved out completely, the second half follows until all three leaflets are completely open (Figure 5.20f). The final open position of the heart valve resembles the open position of the experimental results (Figure 3.13b).

The same opening characteristics are present for the PV tall heart valve during pulse duplication, shown in Figure 5.21. The valve can be seen to open from Figure 5.21 (a) to (b) in a similar manner to the simulated valve shown in Figure 5.20 (d) to (e). The closing of the PV tall valve was similar to the opening, where one half of the leaflet moved towards the centre of the valve before the other, as shown in Figure 5.21 (c) to (d).

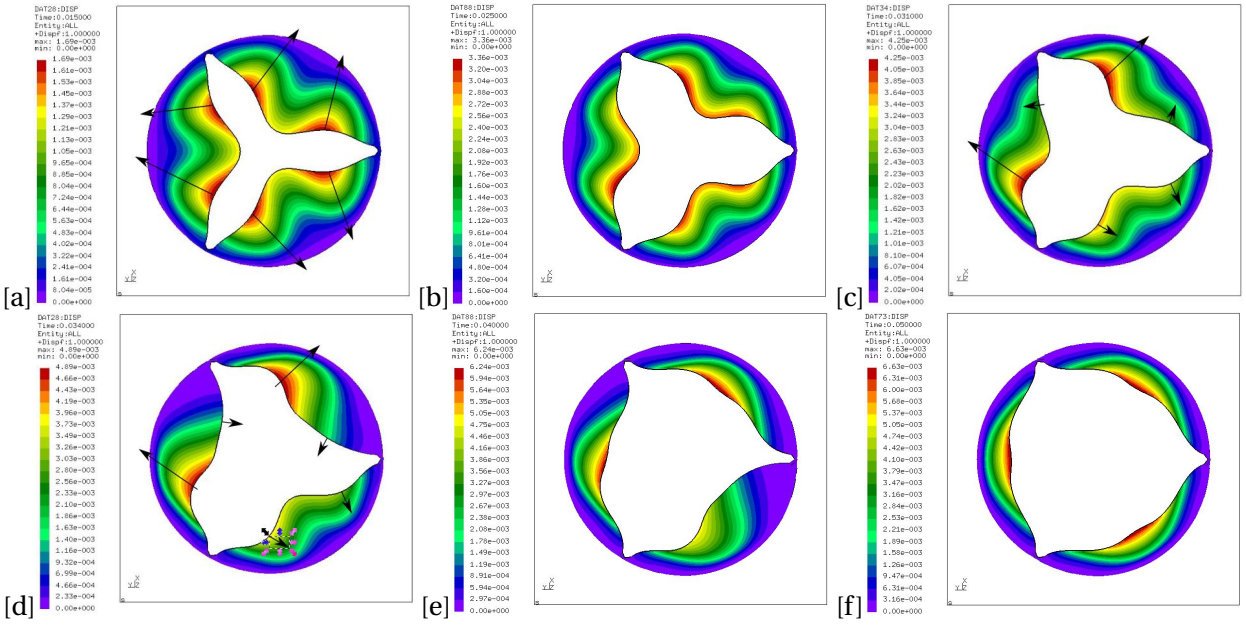

Figure 5.20: Solid domain heart valve leaflet displacement during opening at (a) 15 ms, (b) 25 ms, (c) 31 ms, (d) 34 ms, (e) 40 ms and (f) 50 ms

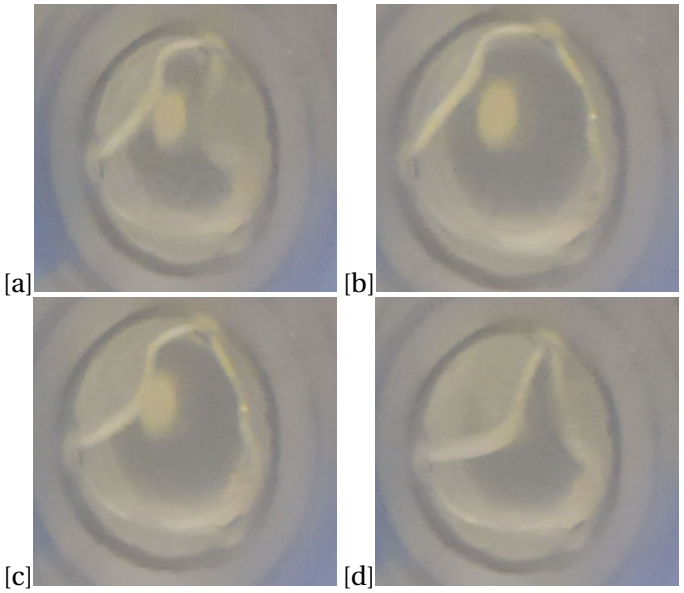

Figure 5.21: PV tall heart valve leaflet at various stages of opening (a - b) and closing (c - d) during pulse duplication

5.4.9 Solid stress

The displacement, maximum and minimum von Mises stress of the heart valve leaflets is summarised in Table 5.6. A maximum displacement of 6.84 mm occured at the tip of the heart valve leaflet at 110ms into the cardiac cycle, before the peak velocity occured.

A maximum stress of 2.79 MPa occured at the same time as the maximum displacement. The von Mises stress at 110 ms is shown in Figure 5.22. The maximum stress occurs at the point of attachment of the polyurethane material with the titanium frame.

Table 5.6: Solid domain displacement, maximum von Mises stress and minimum von Mises stress at various time steps

Time [ms]	Displacement [mm]	Max Stress [MPa]	Min Stress [kPa]	Time [ms]	Displacement [mm]	Max Stress [MPa]	Min Stress [kPa]
15	1.69	2.08	5.15	90	6.82	2.71	6.83
20	2.49	2.4	6.78	100	6.83	2.75	4.03
25	3.36	2.51	6.12	110	6.84	2.79	2.74
29	3.88	2.62	7.48	115	6.84	2.79	2.65
31	4.32	2.65	4.62	120	6.84	2.77	2.77
34	4.89	2.63	4.51	125	6.84	2.76	3.13
37	5.66	2.61	4.86	130	6.83	2.73	3.83
40	6.24	2.16	7.12	135	6.82	2.69	5.12
85	6.81	2.65	6.19	140	6.81	2.65	6.29

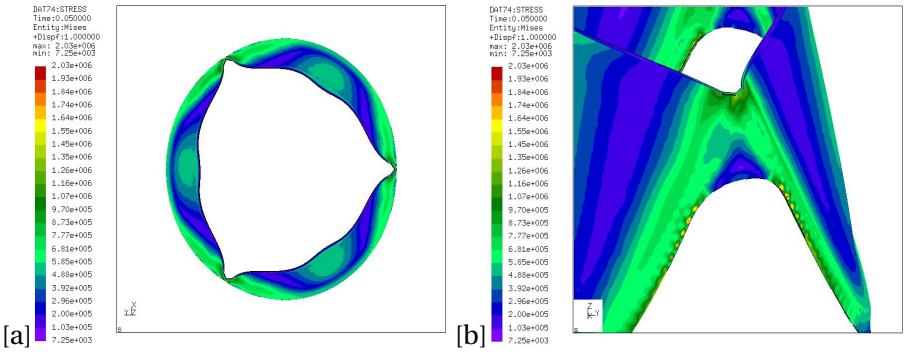

Figure 5.22: von Mises stress profile for the heart valve leaflet in the fully open position

5.5 Discussion

5.5.1 Mesh motion

The RBF mesh motion solver used in this study used coarsening of the boundary points. The RBF mesh motion solver currently suffers from being too computationally and memory inefficient without coarsening, making it impractical to solve for the RBF system matrix (Equation 2.31) with all boundary points used for the interpolation matrix. A secondary problem was found where the same face areas on separate processors were not equal when significant coarsening was used, resulting in the simulations diverging. A solution was found by setting the specific faces equal to each other across processors after mesh motion(Appendix D.1.2). Rewriting the mesh motion solver to utilise all boundary points was outside the scope of this thesis.

Solving for the RBF system matrix using standard linear solvers is a $O(N^2)$ expense procedure in computation and memory, however various methods have been developed to reduce the computational expense. Gumerov and Duraiswami [119] used a fast multipole method to reduce the cost down to a $O(Nlog(N))$ in computation and memory. Yokota *et al.* [120] used a collocation method, where the points in the domain are divided into smaller groups with a buffer layer, where the interpolation matrix is solved for a smaller number of points. The buffer layer ensures that the smaller interpolation matrix is "influenced" by the entire domain. This method was shown to $O(N)$ complexity in both computation and memory. Wang *et al.* [121] used delauney triangulation to reduce the size of the RBF domain to solve for a smaller system matrix of the delauney triangles.

5.5.2 Solver coupling

The increase in speed of the IQN-ILS method is due to the "learning" capability of the IQN-ILS method, reducing the number of iterations per time step after approximately 5 - 10 time steps have been performed. The results agree with that found in Uekermann [90] and Bogaers [88]. The coupling may potentially be improved by employing manifold mapping, as performed by Blom [122]. Manifold mapping may offer improvements over current Quasi-Newton methods, however the Quasi-Newton methods are currently one of the fastest and stable methods for partitioned FSI coupling, and already fully integrated into preCICE.

5.5.3 Pulse duplication

The simulation pressure drop does not correlate with the experimental pressure drop during the first 60 ms of the cardiac cycle. This can be attributed to two physical factors in the experiments. Firstly, the heart valve is completely closed in diastole during the experiments, where the ventricle has to pump the fluid against an almost completely closed valve, whereas the heart valve in the simulation has a gap between all three leaflets to enable meshing between the leaflets. The gap between the leaflets provides less resistance to the flow of fluid, resulting in a lower initial pressure drop. A similar observation of a large pressure drop difference between experimental and simulation results was found by Kadhim *et al.* [123].

Secondly, the CPD has a VIA compliance chamber between the linear actuator and ventricle. As the linear actuator moves forward to pump fluid through the heart valve, the air in the VIA chamber absorbs a portion of the actuator displacement, delaying the increase in volumetric flow rate. The pressure drop increases as the volumetric flow rate gradient increases. However, as the VIA impacts the measured volumetric flow rate through the valve, the simulation volumetric flow rate input and experimentally measured volumetric flow rate differs. Once the valve opens, a sharp increase in the volumetric flow rate occurs once the heart valve opens and fluid begins to accelerate, resulting in a large pressure drop in order to accelerate the fluid.

The average pressure drop for the turbulent flow simulation was closer to the experimental average pressure drop than the laminar flow simulation, however both underpredicted the average pressured drop due to the large pressure spike of the experimental results before 50 ms. The RMS, correlation coefficient and coefficient of determination all had increased accuracy when the data from method 2 was used, confirming that the pressure drop error between the experiments and simulations occurs before 50 ms. The Bland-Altman plot shows that the largest error between the experimental and simulation pressure drop occurs at large pressure drop. The confidence interval of 28.67 is too large for the results to be considered accurate. The error in the Bland-Altman plot for the pressure is due to the physical mechanisms taking place in the CPD during valve opening. The numerical model currently does not account for the compliance chambers and a heart valve starting in the completely closed position.

5.5.4 Velocity

The velocity magnitude for both of the simulation results are lower than the experimental results. The lower magnitude of the velocity at 100 ms may be attributed to the larger orifice area of the heart valve in the simulation, however there is little difference of the orifice width of the experimental and simulation results at peak velocity. The leaflets were modelled as 150 μm thick to match the manufacturing setting, however the dip moulding procedure does not results in perfectly even thickness throughout the leaflet. The result is a leaflet that varies in thickness in the experimental testing, reducing the leaflets ability to open.

The velocity magnitude of the simulations increases sharply between the recirculation zone and the velocity jet, where the fluid velocity increases from 0 m/s to 2.8 m/s across an approximately 1 mm thick VSS region, as opposed to an increase from 0 m/s to 4.5 m/s across an approximately 3 mm thick VSS region. The quick acceleration of the fluid for the simulations results in a larger area for the fluid to flow through for the simulations compared to the experimental results, assisting in reducing the peak velocity magnitude for the simulations. In order to determine the reason for the difference in velocity gradient between the central jet and the recirculation zone, the simulations were rerun with the fluid viscosity doubled. The increase in viscosity had negligible impact on the velocity magnitude and the velocity gradient.

5.5.5 Viscous shear stress

The numerical VSS profile differed from the experimental VSS profile, where the left side VSS jet (red) was larger in magnitude for the numerical results, whereas the right side VSS jet (blue) was larger in magnitude for the experimental results. As the simulation velocity magnitude was less than the experimental results, the larger magnitude of the left side VSS jet is due to the very large velocity gradient through the thin VSS jet (fluid accelerates quickly over a short distance). The experimental VSS jets are thicker than the numerical VSS jets, allowing the fluid to accelerate to a large velocity magnitude without having a large VSS.

The magnitude of the VSS within trileaflet heart valves is difficult to find in literature, with the majority of the literature focusing on the velocity magnitude and solid stress in the leaflets [61; 124; 66]. Ge *et al.* [36] evaluated the VSS of a bileaflet mechanical heart valve and found the VSS was 3 Pa in both PIV experiments and numerical simulations. Borazjani [68] found the simulated VSS of a bileaflet mechanical heart valve and trileaflet heart valve had a maximum VSS of 3.2 Pa. The VSS profile in Borazjani [68] during the open phase exhibit a straight, smooth VSS jet off each leaflet similar to the findings of this study. A difference in the tube geometry result in differing results as Borazjani [68] included the sinus regions on an aortic annulus. Smadi *et al.* [106] used the Low Re $\kappa - \omega$ model to simulate the flow through a dysfunctional mechanical heart valve and found that the shear stress increases significantly if there is a blockage or if the heart valve does not open fully. No shear stresses were reported in the results by Gilmanov and Sotiropoulus [58]; Mao *et al.* [61]; Xu *et al.* [84] who all performed FSI simulations on trileaflet heart valves.

The numerical method developed is capable of determining the downstream VSS for trileaflet heart valves. The measured VSS within the fluid downstream and upstream of the heart valves were found to be lower than the minimum threshold for platelet activation of 10 Pa, and in reasonable agreement with the experimental PIV results. The WSS is a more important numerical simulation parameter as the shear stress against a surface could potentially be much larger than in the fluid domain.

5.5.6 Wall shear stress

The WSS at the sudden contraction was much larger than the threshold limit for platelet activation, indicating that with the current PIV experimental setup, the sudden contraction may be the largest contributor to platelet activation. The heart valve leaflet WSS was larger than 10 Pa which may also contribute to platelet activation over extended use. The large WSS in this region is due to the sudden acceleration of the fluid, where after there is a short region of flow separation. The turbulent flow simulation WSS were consistently larger than the laminar flow simulations. The choice to use turbulent models could be seen as an overly conservative design criteria, as the design criteria would be more difficult to satisfy with each design.

The WSS on the upper half of the heart valve leaflets are between 40 Pa and 60 Pa, indicating the potential for platelet activation due the the sudden contraction as well as the leaflet WSS. The difference between the laminar and turbulent flow simulations showed a difference in WSS at the leaflet tip only, however both simulation models had similar WSS patterns. The accurate prediction of WSS for a complex simulation such as a heart valve is often met with scepticism due to the complex FSI nature of the numerical model and mesh distortion. For a simple diverging nozzle, Stewart *et al.* [108] found the WSS at the sudden expansion to be in the order of approximately 70 Pa to 100 Pa at Re = 6500, similar in magnitude to the WSS of the upper half of the heart valve leaflets. Even for a simple diverging nozzle the predicted WSS is well above the platelet activation threshold.

Gilmanov and Sotiropoulus [58] found the WSS to be a maximum of 1.4 Pa for a trileaflet heart valve, whereas Ghosh *et al.* [125] found the WSS of a surgically implanted trileaflet aortic heart valve to be 92.06 Pa. Gharaie *et al.* [107] found the WSS to vary between 149.23 Pa to 165 Pa for different mesh sizes of the fluid domain. A study of a bileaflet mechanical heart valve by Dumont *et al.* [78] showed a maximum WSS on the leaflets to be approximately 40 Pa, whereas a study by Mirkhani *et al.* [79] on a similar heart valve reported a maximum WSS of 500 Pa in the small hinges region of the heart valve. These values are much larger than the study by Gilmanov and Sotiropoulus [58] and provide a level of confidence in the results of the numerical simulations in this study.

The use of computational studies opens up a secondary avenue for determining the hemolysis and platelet activation threshold. The WSS values were an order of magnitude larger than the VSS values in the numerical simulations. In the hemolysis and platelet activation threshold experiments, the WSS could not be measured. It may be that the actual WSS is larger than the free stream VSS in the experiments and could be the main cause of platelet activation and hemolysis. Further studies combining experimental threshold analysis with numerical simulations to determine the link between VSS, WSS and platelet activation and hemolysis threshold should be performed to assist in the numerical simulation design of heart valves.

5.5.7 Solid displacement

The heart valve leaflets do not open in a uniform manner, where one half of a single leaflets extends outwards before the other half. A similar finding with mechanical heart valves was observed by Borazjani [126], where the leaflet kinematics of the mechanical heart valve were asymmetric. In the case of Borazjani, both the boundary conditions and computational mesh were symmetric. Borazjani [126] concluded that the asymmetric results with the symmetric mesh and boundary conditions was a result of natural flow instabilities.

A similar asymmetric opening of the heart valve leaflets was observed in the pulse duplication experimentation. The asymmetric opening in the experimental testing could be due to small asymmetries of the test setup and varying thickness of the leaflets. However caution must be taken as the asymmetric opening of the numerical simulations may be mesh dependant, as symmetric meshes were not used. A complete mesh independence study with symmetry boundary conditions should be performed, however this cannot be performed with the current mesh motion solver. An explanation for using the RBF mesh motion solver with symmetry boundaries is provided in Appendix E.3.

5.5.8 Solid stress

The numerical simulations showed that the heart valve experienced the largest stress at the top of the pillar at the attachment point of the polyurethane with the frame. This coincided with the experimental observation of a heart valve that failed by de-laminating at the top of the pillar during extended pulse duplication testing. Failure at the top of the pillar occurred for only one heart valve, therefore a conclusion regarding the strength

of the heart valve cannot be determined from a single experiment alone, however some light is shed into potential problematic regions of the current design.

The stress in the heart valve leaflets was approximately an order of magnitude larger than found in van Aswegen [127], however the material properties were vastly different. Tensile strength tests were performed on a strip of the polyurethane material and found that the Young's Modulus was 25.6 MPa. FSI studies on biological tissue heart valves used Young's Modulus values from 3 MPa [66] to 5 MPa [127]. The maximum solid stress in this study (2.79 MPa) was in good comparison to Gharaie *et al.* [107] (2.8 MPa), however the maximum stress in Gharaie *et al.* [107] occurred at the top of the leaflet attachment region during diastole.

5.6 Conclusion

A numerical simulation procedure was developed using a combination of mesh motion and domain remeshing in the fluid simulation to perform transient FSI simulations of heart valves. Software changes were required to Calculix and openFOAM (Section 5.3) in order to perform FSI simulations of heart valves. Results showed that the IQN-ILS coupling scheme was more efficient than the Aitken under-relaxation scheme. The medium and fine fluid meshes were found to differ insignificantly during opening, whereas the fine solid mesh provided the most accurate results for the solid displacement and stress. The interface boundary turbulent kinetic energy, κ, impacted the stability of the solid simulation when the value of κ was reduced too low.

The turbulent flow simulation pressure drop matched the experimental results better than the laminar flow simulation. The simulations reasonably predicted the VSS magnitude but not the velocity magnitude. The simulations revealed that the largest WSS occurred at the sudden contraction upstream of the heart valve and not on the heart valve leaflets itself. The largest solid stress occurred at the top of the heart valve frame where delamination of the leaflets off of the titanium frame could occur, in line with observed experimental results.

The numerical simulation procedure has shown to be a capable R&D tool that could be used to compare different heart valve designs during the early development phase. The pressure drop, VSS and WSS can be determined for each valve design in a much shorter time period than manufacturing and experimentally testing each design. On the contrary, more development is required to determine the simulation procedure capability as a clinical tool. To be useful as a clinical tool, simulations involving moving aortic walls must be combined with the moving heart valve leaflets to mimic the physiology of the body. However, the current numerical procedure has been used within the current development environment and is being used simultaneously with experimental testing to decrease development time.

Chapter 6

Conclusion

6.1 Summary of findings

The aim of the study was to evaluate the hemodynamic performance of a new polyurethane valve based on an original design, using a combination of experimental testing and numerical simulation. The experimental results were compared to the original design and a commercially available tissue valve. The experimental evaluation of the heart valve was performed using a combination of pulse duplication and PIV, and the numerical simulations were performed using open-source software only.

Objective 1: Perform pulse duplication experiments on three different trileaflet heart valves:

The pressure drop, EOA and percentage regurgitation was measured for the tissue, PV short and PV tall heart valves. The average pressure drop of the PV short heart valve was significantly larger than the tissue and PV tall heart valves due to the small geometric area of the open heart valve during systole. The EDP was lower for the PV short heart valve due to the significant leakage during diastole, allowing a significant portion of fluid to flow back through the heart valve during diastole and lowering the aortic pressure.

The EOA of the PV short heart valve was lower than the tissue and PV tall heart valves which had superior EOA performance above minimum ISO regulation requirement. The PV short had the largest leakage volume due to the gap between the leaflets during diastole, whereas the PV tall heart valve had a larger closing volume due to the leaflets requiring reverse flow to close them. The necessity of reverse flow for the PV tall valve was due to the manner in which the leaflets would stay open unless an external force acted on the leaflets.

The input settings of the CPD was found to influence the measured performance of the heart valves. The amount of air placed in the VIA adapter impacted the pressure oscillations of the ventricle pressure, flow rate waveforms and pressure waveforms, and the hemodynamic performance of the heart valves (Appendix B).

Objective 2: Perform particle image velocimetry experiments on three different trileaflet heart valves:

The VSS, RSS, RSS_{maj} and TVSS were determined for each heart valve to predict the onset of hemolysis or platelet activation. The PV short heart valve had the largest velocity magnitude due to the small geometric orifice area, whereas the PV tall heart valve had the smallest velocity magnitude due to the largest geometric orifice area. The PIV results during diastole confirmed the larger reverse flow required to close the PV tall heart valve, where the reverse flow dropped significantly once the heart valve was closed, indicating sufficient sealing between the leaflets.

The VSS for all three heart valves was below 10 Pa, considered to be the threshold for platelet activation. The RSS_{maj} was larger in the leaflet opening area (maximum of 2580) than in the central jet, predicting hemolysis and platelet activation, however the RSS indicated that no hemolysis would occur (maximum of 502 Pa). The RSS and RSS_{maj} should not be used interchangeably as the results may differ between the two methods. The TVSS revealed that the shear stress in the sub-grid scale range may be more than double the VSS measured on the macro scale, potentially indicating platelet activation, however the TVSS values were all below the threshold for hemolysis of 60 Pa. By filtering large velocity fluctuation, the RSS and RSS_{maj} results can be reduced, however the filtering had little impact on the VSS and TVSS. More work is required to determine the exact hemolysis and platelet activation threshold limits for all performance metrics.

Objective 3: Development of a numerical simulation procedure using open-source software for simulating trileaflet heart valves:

A numerical procedure for simulating heart valves using only open-source software was succesfully developed and evaluated. The RBF mesh motion procedure, combined with remeshing, was shown to be capable of handling the large deformations of the heart valve leaflets, however distortion of the leaflets surface occurred during certain stages of the heart valve opening (Appendix F.2). The IQN-ILS coupling method was shown to outperform the Aitken under-relaxation method which has typically been used for strongly coupled problems (Section 5.4.3).

The numerical pressured drop waveform did not match the experimental pressure drop waveform due to physical assumptions in the numerical modelling. The average pressure drop for the turbulent flow simulation matched the experimental results better than the laminar flow simulation (Section 5.4.4).

The velocity profile and magnitude of the numerical simulation did not match the experimental PIV results. The numerical simulation provided a reasonable approximation of the VSS magnitude within the velocity field donwstream of the heart valve. The largest WSS was observed at the sudden contraction upstream of the heart valve (maximum of 183 Pa), and a WSS magnitude of approximately 40 Pa to 60 Pa was found on the upper half of the heart valve leaflet.

The numerical simulation predicted asymmetric opening of the heart valve leaflet, however the asymmetry of the leaflet opening may be due to the asymmetric mesh and not due to the physics of the problem. A maximum von Mises stress of 2.79 MPa was observed at the point of attachment of the polyurethane material with the titanium frame, matching observations where a heart valve failed by delaminating off the frame at the

top of the frame pillar.

6.2 Contributions

To the best of the authors knowledge, this work was the first to provide a comparison between the VSS, RSS, RSS_{maj} and TVSS performance metrics for the prediction of hemolysis and platelet activation in a trileaflet heart valve. Previous work used either the RSS or RSS_{maj}, however this study showed that these metrics may provide vastly differing results. A combination of all four performance metrics is recommended during experimental testing.

A numerical procedure for simulating a heart valve using open-source software, utilising a moving mesh based method was presented, using the RBF mesh motion scheme and domain remeshing. The IQN-ILS coupling scheme was shown to offer superior convergence performance compared to Aitken under-relaxation for the simulation of heart valves. It was shown to be possible to model the hemodynamic performance of a heart valve that can be used in the design stage to compare various designs before manufacture.

6.3 Recommendations for future work

A number of research areas have been identified for further research to improve the experimental testing and simulation of heart valve hemodynamics.

Pulse duplication

Current pulse duplication methods use pulse duplicators with rigid walls. The use of flexible tubing to mimic the soft tissue of the aortic wall should be implemented into the ViVitro Labs pulse duplicator. The use of flexible tubing for the aorta may help to dampen out the pressure fluctuations and allow for determining the influence of the size of the aortic sinus region.

Particle image velocimetry

The use of stereoscopic PIV may improve the shear stress prediction by incorporating the out of plane velocity measurements. This may improve not only the VSS results, but also the TVSS results. Modifications to the downstream viewing area to include sinus regions may results in more physiologically correct velocity fields, however the laser sheet distortion around the curved walls of the sinus region need to be examined.

Fluid-structure interaction simulations

The RBF mesh motion solver currently uses the software Eigen to solve for a large, dense matrix. The use of local basis functions with sparse matrix solvers may reduce RAM and CPU usage. A numerical method for modelling the heart valve during diastole should be investigated by using the preCICE coupler to enforce the pressure boundary conditions for a contact simulation to determine the stresses in the leaflet during closing and diastole, as well as measuring the leakage flow through a closed heart valve.

List of References

[1] Venes, D. and Taber, C.W.: *Taber's Cyclopedia Medical Dictionary*. 20th edn. Taylor and Francis Group, 2005.

[2] Dasi, L., Simon, H., Sucosky, P. and Yoganathan, A.: Fluid mechanics of artificial heart valves. *Clinical and experimental pharmacology and physiology*, 2009.

[3] American Heart Assosciation: Problem: Heart valve regurgitation. 2016. Available at: `http://www.heart.org/HEARTORG/Conditions/More/HeartValveProblemsandDisease/Problem-Heart-Valve-Regurgitation_UCM_450736_Article.jsp#.V6mywU197IU`

[4] University of South Carolina Department of Surgery: Valves of the heart. Available at: `http://www.surgery.usc.edu/cvti/pg-heartsurgery-valvesoftheheart.html`

[5] Van Nooten, G., Caes, F., Francois, K., Van Bellleghem, Y., Bove, T., Vandenplas, G. and Taeymans, Y.: Twenty years' single-center experience with mechanical heart valves: A critical review of anticoagulation policy. *The Journal of Heart Valve Disease*, vol. 21, pp. 88 – 98, 2012.

[6] Kaneko, T. and Aranki, S.: Anticoagulation for prosthetic valve. *Thrombosis*, vol. 2013, 2013.

[7] Hewitson, J. and Zilla, P.: Children's heart disease in sub-saharan africa: Challenging the burden of disease. *South African medical journal*, 2010.

[8] Yoganathan, A., He, Z. and Casey Jones, S.: Fluid mechanics of heart valves. *Annual review of Biomedical Engineering*, 2004.

[9] Alves, P.: Surface modifications of ploy urthane films by plasma and ultraviolet light to improve haemocompatibility for artificial heart valves. *Colloids and Surfaces B: Biointerfaces*, vol. 29, no. 1, pp. 47–65, 2013.

[10] Zilla, P., Brink, J., Human, P. and Bezuidenhout, D.: Prosthetic heart valves: Catering for the few. *Biomaterials*, 2008.

[11] Kutting, M., Roggenkamp, J., Urban, U., Schmitz-Rode, T. and Steinseifer, U.: Polyurethane heart valves: past, present and future. *Expert Review of Medical Devices*, vol. 8, pp. 227 – 233, 2011.

[12] Bernacca, G., Mackay, T., Wilkinson, R. and Wheatley, D.: Polyurethane heart valves: Fatigue failure, calcification, and polyurethane structure. *Journal of Biomedical Materials Research*, 1997.

[13] Yacoub, M. and Takkenberg, J.: Will heart valve tissue engineering change the world? *Nature Clinical Practice Cardiovascular Medicine*, 2004.

[14] World Health Organisation: The atlas of heart disease and stroke. 2003.
Available at: `http://www.who.int/cardiovascular_diseases/en/cvd_atlas_02_rheumaticHD.pdf?ua=1`

[15] Aggarwal, S., Gross, C.M., Porcelli, R.J. and Black, S.M.: Chapter 14 - pulmonary hemodynamics. In: *Comparative Biology of the Normal Lung (Second Edition)*, 2nd edn, pp. 205 – 243. Academic Press, San Diego, 2015.

[16] Sacks, M., Merryman, W. and Schmidt, D.: On the biomechanics of heart valve function. *Journal of Biomechanics*, 2009.

[17] Campbell, R.: *Fluid-Structure Interaction*. PhD, The State University of Pennsylvania, 2010.

[18] ViVitroLabs and Inc.: Pulse duplicators. 2018.
Available at: `https://vivitrolabs.com/wp-content/uploads/2016/02/Pulse-Duplicator-Brochure-2016-VIVI-MKT-046.pdf`

[19] ViVitroLabs and Inc.: Pulse duplicator ev brochure. 2016.
Available at: `https://vivitrolabs.com/product/endovascular-ev-simulator/pulse_duplicator_ev_brochure/`

[20] Rodriguez, R.: *Redesign and Performance Evaluation of a Cardiac Pulse Duplicator*. Master's thesis, Department of Mechanical and Mechatronic Engineering, Stellenbosch university, 2017.

[21] Retta, S., Kepner, J., Marquez, S., Herman, B.A. Shu, M. and Grossman, L.: In-vitro pulsatile flow measurement in prosthetic heart valves: An inter-laboratory comparison. *The Journal of Heart Valve Disease*, 2017.

[22] Capulli, A., Emmert, M., Pasqualini, F., Kehl, D., Caliskan, E., Lind, J., Sheehy, S., Park, S., Ahn, S., Weber, B., Goss, J., Hoerstrup, S. and Parker, K.: Jetvalve: Rapid manufacturing of biohybrid scaffolds for biomimetic heart valve replacement. *Biomaterials*, 2017.

[23] Yokoyama, Y., Kawaguchi, O., Shinshi, T., Steinseifer, U. and Takatani, S.: A new pulse duplicator with a passive fill ventricle for analysis of cardiac dynamics. *The Journal of Artificial Organs*, 2010.

[24] Schleicher, M., Sammler, G., Schmauder, M., Fritze, O., Huber, A.J., Schenke-Layland, K., Ditze, G. and Stock, U.A.: Simplified pulse reactor for real-time long-term in vitro testing of biological heart valves. *Annals of Biomedical Engineering*, vol. 38, pp. 1919 – 1927, 2010.

[25] International Organisation of Standards: *ISO 5840:2015(en):Cardiovascular implants - Cardiac valve prostheses - Part 1: General requirements*, 2015.

[26] Dynamics, D.: Measurement principles of piv. 2018.
Available at: `https://www.dantecdynamics.com/measurement-principles-of-piv`

[27] Prasad, A.: Stereoscopic particle image velocimetry. *Experiments in Fluids*, 2000.

[28] Browne, P., Ramuzat, A., Saxena, R. and Yoganathan, A.P.: Experimental investigation of the steady flow downstream of the st. jude bileaflet heart valve: A comaparison between laser doppler velocimetry and particle image velocimetry techniques. *Annals of Biomedical Engineering*, vol. 28, pp. 39 – 47, 2000.

[29] Kheradvar, A., Groves, E., Falahatpisheh, A., Mofrad, M., Hamed Alavi, S., Tranquillo, R., Dasi, L., Simmons, C., Jane Grande-Allen, K., Goergen, C., Baaijens, F., Little, S., Canic, S. and Griffith, B.: Emerging trends in heart valve engineering: Part iv. computational modeling and experimental studies. *Annals of Biomedical Engineering*, vol. 43, pp. 2314 – 2333, 2015.

[30] Grigioni, M.: Innovative technologies for the assessment of cardiovascular medical devices: state-of-the-art techniques for artificial heart valve testing. *Expert Review of Medical Devices*, vol. 1, pp. 81 – 93, 2004.

[31] Dantec Dynamics: Dynamicstudio - the smart software for imaging systems. 2000.

[32] Falahatpisheh, A. and Kheradvar, A.: High-speed particle image velocimetry to assess cardiac fluid dynamics in vitro: From performance to validation. *European Journal of Mechanics B/Fluids*, 2012.

[33] Del Gaudio, C., Gasbarroni, P. and Romano, G.: Experimental investigations on the fluid-mechanics of an electrospun heart valve by means of particle image velocimetry. *Journal of the mechanical behaviour of biomedical materials*, 2016.

[34] Toninato, R., Salmon, J. Susin, F., Ducci, A. and Burriesci, G.: Physiological vortices in the sinuses of valsalva: An in vitro approach for bio-prosthetic valves. *Journal of Biomechanics*, vol. 49, pp. 2635 – 2643, 2016.

[35] Annerel, S., Claessens, T., Degroote, J., Segers, P. and Vierendeels, J.: Validation of a numerical fsi simulation of an aortic bmhv by in vitro piv experiments. *Medical Engineering and Physics*, 2014.

[36] Ge, L., Dasi, L., Sotiropoulus, F. and Yoganathan, A.: Characterization of hemodynamic forces induced by mechanical heart valves: Reynolds vs. viscous stresses. *Annals of Biomedical Engineering*, 2007.

[37] Dasi, L.a.: Vorticity dynamics of a bileaflet mechanical heart valve in an axisymetric aorta. *Physics of Fluids*, vol. 19, pp. 36 – 54, 2007.

[38] Ducci, A., Pirisi, F., Tzamtzis, S. and Burriesci, G.: Transcatheter aortic valves produce unphisiological flows which may contribute to thromboembolic events: An in-vitro study. *Journal of Biomechanics*, 2016.

[39] Hutchinson, C., Sullivan, P. and Ethier, C.: Measurements of steady flow through a bileaflet mechanical heart valve using stereoscopic piv. *Medical and Biological Engineering and Computing*, vol. 49, pp. 36 – 54, 2011.

[40] Kaminsky, R., Kallweit, S., Weber, H., Claessens, T., Jozwik, K. and Verdonck, P.: Flow visualization through two types of aortic prosthetic heart valves using stereoscopic high-speed particle image velocimentry. *International Center for Artificial Organs and Transplantation*, vol. 31, pp. 869 – 879, 2007.

[41] Marassi, M., Paone, N., Pinotti, M. Scalise, L. and Tomasini, E.: Development of an advanced mechanical heart valves piv test bench.

[42] Leo, H., Dasi, L., Carberry, J., Simon, H. and Yoganathan, A.: Fluid dynamic assessment of three polymeric heart valves using particle image velocimetry. *Annals of Biomedical Engineering*, vol. 34, pp. 936 – 952, 2006.

[43] Hasler, D., Landolt, A. and Obrist, D.: Tomographic piv behind a prosthetic heart valve. *Experiments in Fluids*, vol. 57, 2016.

[44] Li, C., Lo, C. and Lu, P.: Estimation of viscous dissipative stresses induced by a mechanical heart valve using piv data. *Annals of Biomedical Engineering*, vol. 38, pp. 903 – 916, 2010.

[45] Yen, J., Chen, S., Chern, M. and Lu, P.: The effect of turbulent viscous shear stress on red blood cell hemolysis. *The Japanese Society for Artificial Organs*, vol. 17, pp. 178 – 185, 2014.

[46] Sutera, S., Croce, P. and Mehrjardi, M.: Hemolysis and subhemolytic alterations of human rbc induced by turbulent shear flow. *Trans American Society of Artificial Organs*, 1972.

[47] Lu, P., Lai, H. and Liu, J.: A reevaluation and discussion on the threshold limit for hemolysis in a turbulent shear flow. *Journal of Biomechanics*, 2001.

[48] Sheng, J., Meng, H. and Fox, R.: A large eddy piv method for turbulence dissipation rate estimation. *Chemical Engineering Science*, vol. 55, pp. 4423 – 4434, 2000.

[49] Versteeg, H. and Malalasekera, W.: *An introduction to computational fluid dynamics: The finite volume method*. 2nd edn. Prentice Hall, 2007.

[50] Lee, H., Tatsumi, E. and Taenaka, Y.: Flow visualization of a monoleaflet and bileaflet mechanical heart valve in a pneumatic ventricular assist device using a piv system. *ASAIO Journal*, 2010.

[51] Raghav, R., Okafor, I., Quach, M., Dang, L., Marquez, S. and Yoganathan, A.: Long-term durability of carpentier-edwards magna ease valve: A one billion cycle in vitro study. *The Society of Thoracic Surgeons*, vol. 101, pp. 1759 – 1767, 2015.

[52] Grigioni, M., Daniele, c., D'Avenio, G. and Barbaro, V.: A discussion on the threshold limit for hemolysis related to reynolds shear stress. *Journal of Biomechanics*, vol. 32, pp. 1107 – 1112, 1999.

[53] Kysela, B., Jašíková, D., Konfršt, J., Šulc, R. and Ditl, P.: Estimation of turbulence dissipation rate by Large eddy PIV method in an agitated vessel. *EPJ Web of Conferences*, vol. 92, pp. 4 – 8, 2015.

[54] Shim, E. and Chang, K.: Numerical analysis of three-dimensional bjork-shiley valvular flow in an aorta. *Journal of Biomechanical Engineering*, vol. 119, pp. 45 – 51, 1997.

[55] King, M., Corden, J., David, T. and Fisher, J.: A three-dimensional, time-dependant analysis of flow through a bileaflet mechanical heart valve: comparison of experimental and numerical results. *Journal of Biomechanics*, vol. 29, pp. 609 – 618, 1996.

[56] Ge, L., Jones, S., Sotiropoulus, F., Healy, T. and Yoganathan, A.: Numerical simulation of flow in mechanical heart valves: grid resolution and the assumption of flow symmmetry. *Journal of Biomechanical Engineering*, vol. 125, pp. 709 – 718, 2003.

[57] Nobili, M. and Morbiducci, U.: Numerical simulation of the dynamics of a bileaflet prosthetic heart valve using a fluid-structure interaction approach. *Journal of Biomechanics*, 2008.

[58] Gilmanov, A. and Sotiropoulus, F.: Comparative hemodynamics in an aorta with bicuspid and trileaflet valves. *Theoretical and Computational Fluid Dynamics*, vol. 30, pp. 67 – 85, 2016.

[59] Ge, L. and Sotiropoulus, F.: A numerical method for solving the 3d unsteady incompressible navier-stokes euations in curvilinear domains with complex immersed boundaries. *Journal of Computational Physics*, vol. 225, pp. 1782 – 1809, 2007.

[60] Alemu, Y. and Bluestein, D.: Flow-induced platelet activation and damage accumulation in a mechanical heart valve: numerical studies. *Artificial Organs*, vol. 31, no. 9, pp. 677 – 688, 2007.

[61] Mao, W., Li, K. and Sun, W.: Fluid-structure interaction study of transcatheter aortic valve dynamics using smoothed particle hydrodynamics. *Cardiovascular Engineering and Technology*, vol. 7, pp. 374 – 388, 2016.

[62] Bavo, A.M., Rocatello, G., Iannaccone, F., Degroote, J., Vierendeels, J. and Segers, P.: Fluid-structure interaction simulation of prosthetic aortic valves: Comparison between immersed boundary and arbitrary lagrangian-eulerian techniques for the mesh representation. *PLOS One*, vol. 11, p. e0154517, 2016.

[63] Prakash, S. and Ethier, C.: Requirements for mesh resolution in 3d computational hemodynamics. *Journal of Biomechanical Engineering*, vol. 123, pp. 134 – 144, 2001.

[64] De Hart, J., Peters, G., Schreurs, P. and Baaijens, F.: A three-dimensional computational analysis of fluid-structure interaction in the aortic valve. *Journal of Biomechanics*, vol. 36, pp. 103 – 112, 2003.

[65] Marom, G., Haj-Ali, R., Raanani, E., Schäfers, H. and Rosenfeld, M.: A fluid-structure interaction model of the aortic valve with coaptation and compliant aortic root. *Medical and Biological Engineering and Computing*, vol. 50, pp. 173 – 182, 2012.

[66] Kemp, I.: *Development, Testing and Fluid Structure Interaction Simulation of a Bioprosthetic Valve for Transcatheter Aortic Valve Implantation.* Master's thesis, Department of Mechanical and Mechatronic Engineering, Stellenbosch university, 2012.

[67] Wu, W., Pott, D., Mazza, B., Sironi, T., Dordoni, E., Chiastra, C., Petrini, Lorenzaand Pennati, G., Dubini, G., Steinseifer, U., Sonntag, S., Kuetting, M. and Migliavacca, F.: Fluid-structure interaction model of a percutaneous aortic valve: Comparison with an in vitro test and feasibility study in a patient-specific case. *Annals of Biomedical Engineering*, vol. 44, no. 2, pp. 590 – 603, 2016.

[68] Borazjani, I.: Fluid structure interaction, immersed boundary finite element method simulations of bio prosthetic heart valves. *Computer methods in applied mechanics and engineering*, 2013.

[69] Farhat, C., Van der Zee, K. and Philippe, G.: Provably second-order time-accurate loosely-coupled solution algorithms for transient nonlinear computational aeroelasticity. *Computer Methods in Applied Mechanics and Engineering*, vol. 195, pp. 1973 – 2001, 2006.

[70] Joubert, E.: *Numerical and Experimental Investigation of One-way Fluid Structure Interaction of a Vertical Cantilever Beam in an Air Stream.* Ph.D. thesis, Deparment of Mechanical and Mechatronic Engineering, Stellenbosch University, 2015.

[71] Stein, K., Benney, R., Kalro, V., Johnson, A. and Tezduyar, T.: Parallel computation of parachute fluid-structure interactions. *14th Aerodynamic Decelerator Systems Technology Conference*, vol. 97, 1997.

[72] Donea, J., Giuliani, S. and Halleux, J.: An arbitrary Lagrangian-Eulerian finite element method for transient dynamic fluid-structure interactions. *Computer Methods in Applied Mechanics and Engineering*, vol. 33, pp. 689 – 723, 1982.

[73] De Hart, J., Peters, G., Schreurs, P. and Baaijens, F.: A computational of fluid-structure interaction analysis of a fiber-reinforced stentless aortic valve. *Journal of Biomechanics*, vol. 36, pp. 699 – 712, 2003.

[74] Hsu, M.-C., Kamensky, D., Bazilevs, Y., Sacks, M.S. and Hughes, T.J.R.: Fluid-structure interaction analysis of bioprosthetic heart valves: significance of arterial wall deformation. *Computational Mechanics*, vol. 54, no. 4, pp. 1055 – 1071, 2014.

[75] Monolithic ale finite element fluid-structure interaction modeling of aortic valves. *22nd Congress of the European Society of Biomechancis*, 2016.

[76] Hoffman, J., Jansson, J. and Jansson, N.: Fenics-hpc: Automated predictive high-performance finite element computing with applications in aerodynamics. *Proceedings of the 11th International Conference on Parallel Processing and Applied Mathematics, PPAM*, 2015.

[77] Alnæs, M.S., Blechta, J., Hake, J., Johansson, A., Kehlet, B., Logg, A., Richardson, C., Ring, J., Rognes, M.E. and Wells, G.N.: The fenics project version 1.5. *Archive of Numerical Software*, vol. 3, no. 100, 2015.

[78] Dumont, K., Vierendeels, J., Kaminsky, R., van Nooten, G., Verdonck, P. and Bluestein, D.: Comparison of the hemodynamic and thrombogenic performance of two bileaflet mechanical heart valves using a cfd/fsi model. *Journal of Biomechanical Engineering*, vol. 129, 2007.

[79] Mirkhani, N., Davoudi, M.R., Hanafizadeh, P., Javidi, D. and Saffarian, N.: On-x heart valve prosthesis: Numerical simulation of hemodynamic performance in accelerating systole. *Cardiovascular Engineering and Technology*, vol. 7, pp. 223 – 237, 2016.

[80] Peskin, C.: Numerical analysis of blood flow in the heart. *Journal of Computer Physics*, vol. 25, pp. 220 – 252, 1977.

[81] Peskin, C. and McCracken, M.: A vortex method for blood flow through heart valves. *Journal of Computer Physics*, vol. 35, pp. 183 – 205, 1980.

[82] Kang, S.: *Numerical modelling of turbulent flows in arbitrarily complex natural streams*. PhD, University of Minnesota, 2010.

[83] Jasak, H., Rigler, D. and Tukovic, Z.: Validation of finite volume immersed boundary method. 2014.

[84] Xu, F., Morganti, S., Zakerzadeh, R., Kamensky, D. Auricchio, F., Reali, A., Hughes, T., Sacks, M. and Hsu, M.: A framework for designing patient-specific bioprosthetic heart valves using immersogeometric fluid-structure interaction analysis. Tech. Rep., The institute for Computational Engineering and Sciences, The University of Texas at Austin, 2017.

[85] Jasak, H. and Tukovic, Z.: Immersed boundary method in foam: Theory, implementation and use. 2015.

[86] Sotiropoulus, F. and Yang, X.: Immersed boundary methods for simulating fluid-structure interaction. *Progress in Aerospace Sciences*, vol. 65, pp. 1 – 21, 2014.

[87] Gatzhammer, B.: *Efficient and Flexible Partitioned Simulation of Fluid-Structure Interactions*. Ph.D. thesis, Technische Universität München, 2014.

[88] Bogaers, A.: *Efficient and robust partitioned solution schemes for fluid-structure interactions*. Ph.D. thesis, University of Cape Town, 2015.

[89] Wick, T.: Solving monolithic fluid-structure interaction problems in arbitrary lagrangian eulerian coordinates with the deal.ii library. *Archives of Numerical Software*, vol. 1, pp. 1 – 19, 2013.

[90] Uekermann, B.: *Partitioned Fluid-Structure Interaction on Massively Parallel Systems*. PhD, Technische Uniersität München, 2016.

[91] Förster, C., Wall, W.A. and Ramm, E.: Artificial added mass instabilities in sequential staggered coupling of nonlinear structures and incompressible viscous flows. *Computer Methods in Applied Mechanics and Engineering*, vol. 196, pp. 1278 – 1293, 2007.

[92] Degroote, J., Bruggeman, P., Haelterman, R. and Vierendeels, J.: Stability of a coupling technique for partitioned solvers in FSI applications. *Computers and Structures*, vol. 86, pp. 2224 – 2234, 2008.

[93] Causin, P., Gerbeau, J. and Nobile, F.: Added-mass effect in the design of partitioned algorithms for fluid-structure problems. *Computer methods in applied mechanics and engineering*, vol. 194, pp. 4506 – 4527, 2005.

[94] Cheung, L.: *Conjugate Heat Transfer with the Multiphysics Coupling Library preCICE*. Master's thesis, Technische Uniersität München, 2016.

[95] Bos, F.: *Numerical simulation of flapping foil and wind aerodynamics: Mesh de- formation using radial basis functions*. Ph.D. thesis, Technical University Delft, 2009.

[96] *New Method For Mesh Moving Based On Radial Basis Function Interpolations*. 2006.

[97] Bayona, V., Flyer, N., Lucas, G. and Baumgaertner, A.: A 3-d rbf-fd solver for modeling the atmospheric global electric circuit with topography. *Geoscience Model Development*, vol. 8, pp. 3007 – 3020, 2015.

[98] Wang, T., Wüchner, R., Sicklinger, S. and Bletzinger, K.-U.: Assessment and improvement of mapping algorithms for non-matching meshes and geometries in computational fsi. *Computational Mechanics*, vol. 57, no. 5, pp. 793 – 816, 2016.

[99] de Villiers, E.: *The potential of Large Eddy Simulation for the modelling of wall bounded flows*. PhD, Imperial College of Science, Technology and Medicine, 2006.

[100] SU2: Transitional flat plate. 2018.
Available at: `https://su2code.github.io/tutorials/Transitional_Flat_Plate/`

[101] *Mathematics of Large Eddy Simulation of Turbulent Flows*. Springer, 2005.

[102] Bredberg, J.: On the wall boundary conditions for turbulence models. Tech. Rep., Department of Thermo and Fluid Dynamics, Chalmers University of Tecnology, 2000.

[103] Salim, S.M. and Cheah, S.: Wall y+ strategy for dealing with wall-bounded turbulent flows. *International MultiConference of Engineers and Computer Scientists*, 2009.

[104] *Computational Fluid Dynamics: Principles and Applications*. 2nd edn. Elsevier, 2001.

[105] Cfd-Online: Transitional flat plate. 2018.
Available at: `https://www.cfd-online.com/W/images/b/b0/HRNvsLRN.png`

[106] Smadi, O., Hassan, I., Pibarot, P. and Kadem, L.: Numerical and experimental investigations of pulsatile blood flow pattern through a dysfunctional mechanical heart valve. *Journal of Biomechanics*, vol. 43, pp. 1565 – 1572, 2010.

[107] Gharaie, S.H., Mosadegh, B. and Morsi, Y.: In Vitro Validation of a Numerical Simulation of Leaflet Kinematics in a Polymeric Aortic Valve Under Physiological Conditions. *Cardiovascular Engineering and Technology*, vol. 9, pp. 42 – 52, 2018.

[108] Stewart, S.F., Paterson, E.G., Burgreen, G.W. and Harharan, P.: Assessment of cfd performance in simulations of an idealized medical device: Results of fda's first computational interlaboratory study. *Cardiovascular Engineering and Technology*, 2012.

[109] Jennings, L., Betturfield, M., Walker, P., Watterson, K. and Fisher, J.: The influence of ventricular input impedance on the hydrodynamic performance of bioprosthetic aortic roots in vitro. *Journal of Heart Valve Disease*, 2001.

[110] Saikrishnan, N., Yap, C.-H., Milligan, N.C., Vasilyev, N.V. and Yoganathan, A.P.: In vitro characterization of bicuspid aortic valve hemodynamics using particle image velocimetry. *Annals of Biomedical Engineering*, vol. 40, pp. 1760 – 1775, 2012.

[111] Stewart, S.F., Harharan, P., Paterson, E.G. and Burgreen, G.W.: Results of fda's first interlaboratory computational study of a nozzle with a sudden contraction and conical diffuser. *Cardiovascular Engineering and Technology*, 2013.

[112] openFOAMWiki: Installation/linux/foam-extend-4.0. 2018.
Available at: `https://openfoamwiki.net/index.php/Installation/Linux/foam-extend-4.0`

[113] Blom, D.: Fluid-structure interaction solvers for foam-extend. 2016.
Available at: `https://github.com/davidsblom/FOAM-FSI`

[114] Dhondt, G. and Wittig, K.: Calculix: A free software three-dimensional structural finite element program. 2017.
Available at: `http://www.calculix.de/`

[115] Bungartz, H.-J., Lindner, F., Gatzhammer, B., Mehl, M., Scheufele, K., Shukaev, A. and Uekermann, B.: preCICE – a fully parallel library for multi-physics surface coupling. *Computers and Fluids*, vol. 141, pp. 250–258, 2016. Advances in Fluid-Structure Interaction.

[116] Thubrikar, M.: *The Aortic Valve*. 1st edn. CRC Press Inc., 1990.

[117] SimScale: K-omega sst. 2018.
Available at: `https://www.simscale.com/docs/content/simulation/model/turbulenceModel/kOmegaSST.html`

[118] Wiki, C.O.: Turbulence free stream boundary conditions. 2014.
Available at: `https://www.cfd-online.com/Wiki/Turbulence\_free-stream\_boundary\_conditions\#Specific\_dissipation\_rate`

[119] Gumerov, N.A. and Duraiswami, R.: Fast radial basis functions interpolation via preconditioned krylov iterations. *Society for Industrial and Applied Mathematics*, vol. 29, pp. 1876 – 1899, 2007.

[120] Yokota, R., Barba, L. and Knepley, M.G.: Petrbf - a parallel o(n) algorithm for radial basis function interpolation with gaussians. *Computational Methods in Applied Mathematics and Engineering*, vol. 199, pp. 1793 – 1804, 2010.

[121] Wang, Y., Qin, N. and Zhao, N.: Delaunay graph and radial basis function for fast quality mesh deformation. *Journal of Computaional Physics*, vol. 294, pp. 149 – 172, 2015.

[122] Blom, D.S., Van Zuijlen, A.H. and Bijl, H.: Acceleration of strongly coupled fluid-structure interaction with manifold mapping. *11th World Congress on Computational Mechanics*, 2014.

[123] Kadhim, S.K., Nasif, M.S., Al-Kayiem, H.H. and Al-Waked, R.: Computational fluid dynamics simulation of blood flow profile and shear stresses in bileaflet mechanical heart valve by using monolithic approach. *Simulation Transactions of the Society for Modeling and Simulation International*, vol. 94, pp. 93 – 104, 2018.

[124] Kamensky, D., Hsu, M.-C., Schillinger, D., Evans, J.A., Aggarwai, A., Bazilevs, Y., Sacks, M.S. and Hughes, T.J.: An immersogeometric variational framework for fluid-structure interaction: Application to bioprothetic heart valves. *Computer methods in applied mechanics and engineering*, vol. 284, pp. 1005 – 1053, 2015.

[125] Ghosh, R.P., Marom, G., Rotman, O.M., Bianchi, M., Prabhakar, S., Horner, M., Slepian, M.J. and Bluestein, D.: Evaluation of novel polymeric transcatheter and surgical aortic valves with fluid-structure interaction models and experimental analysis. *Summer Biomechanics, Bioengineering and Biotransport Conference*, 2017.

[126] Borazjani, I.: *Numerical Simulations of Fluid-Structure Interaction Problems in Biological Flows*. PhD, University of Minnesota, 2008.

[127] van Aswegen, K.: *Dynamic modelling of a stented aortic valve*. Master's thesis, Department of Mechanical and Mechatronic Engineering, Stellenbosch university, 2008.

[128] *Nonlinear finite element methods*. Springer, 2008.

[129] *Nonlinear Solid Mechanics: A Continuum Approach for Engineering*. John Wiley and Sons, 2001.

[130] Davis, K., Müller, J.H., Meyer, C.J. and Smit, F.E.: Evaluating the impact of air compliance chamber volumes on valve performance for three different heart valves. *2018 3rd Biennial South African Biomedical Engineering Conference (SAIBMEC)*, pp. 1 – 4, 2018.

[131] Gerbeau, J.-F. and Vidrascu, M.: A quasi-newton algorithm based on a reduced model for fluid-structure interaction problems on blood flows. *Mathematical Modelling and Numerical Analysis*, vol. 37, pp. 631 – 647, 2003.

[132] Formaggia, L., Gerbeau, Jean-Frederic adn Nobile, F. and Quarteroni, A.: On the coupling of 3d and 1d navier-stokes equations for flow problems in compliant vessels. Tech. Rep., Reasearch Report RR-3862 INRIA. 2000. <inria-00072794>, 2006.

[133] Fernandez, M.A. and Moubachir, M.: A newton method using exact jacobians for solving fluid-structure coupling. Tech. Rep., Reasearch Report RR-5085 INRIA. 2004. <inria-00071498>, 2006.

[134] Malan, A. and Oxtoby, O.: An accelerated, fully-coupled, parallel 3d hybrid finite volume fluid-structure interaction scheme. *Computer Methods in Applied Mechanics and Engineering*, 2012.

[135] Blom, D.S.: *Efficient Numerical Methods for Partitioned Fluid-Structure Interaction Simulations*. PhD, Technische Uniersiteit Delft, 2017.

[136] Richter, T.: Goal-oriented error estimation for fluid-structure interaction problems. *Computer methods in applied mechanics and engineering*, 2012.

[137] Syrakos, A., Varchanis, S., Dimakopoulos, Y., Goulas, A. and Tsamopoulos, J.: A critical analysis of some popular methods for the discretisation of the gradient operator in finite volume methods. *Physics of Fluids*, vol. 29, 2016.
Available at: `https://www.researchgate.net/publication/304128076`

[138] Syrakos, A.: Gauss linear gradient scheme results in zeroth-order accuracy. 2017.
Available at: `https://bugs.openfoam.org/view.php?id=2596`

[139] preCICE: Xml reference. 2018.
Available at: `https://github.com/precice/precice/wiki/XML-Reference`

Appendix A

Governing Equations

A.1 Fluid domain

The fluid domain is modelled using the arbitrary-lagrangian eulerian (ALE) formulation of the Navier-Stokes equations, which accounts for the movement of the fluid domain mesh. The continuity and momentum formulation of the Navier-Stokes equation for an incompressible, Newtonian fluid is given by

$$\nabla \cdot \mathbf{u} = 0 \tag{A.1}$$

$$\rho(\frac{\partial \mathbf{u}}{\partial t} + (\mathbf{u} - \mathbf{u}_m) \cdot \nabla \mathbf{u}) = -\nabla p + \mu \Delta \mathbf{u} + \rho \mathbf{f} \tag{A.2}$$

where ρ is the fluid density, $\mathbf{u}$ is the fluid velocity, $\mathbf{u}_m$ is the velocity of the fluid mesh, p is the fluid pressure, μ is the dynamic viscosity of the fluid and $\mathbf{f}$ is the external body forces acting in the domain Ω_f. The energy equation is omitted for brevity as no heat transfer or temperature variations is considered in this study. Equation A.2 is divided by the fluid density

$$\frac{\partial \mathbf{u}}{\partial t} + (\mathbf{u} - \mathbf{u}_m) \cdot \nabla \mathbf{u} = -\nabla p + \nu \Delta \mathbf{u} + \mathbf{f} \tag{A.3}$$

where p is now the kinematic pressure and ν is the kinematic viscosity. openFOAM uses the kinematic pressure and kinematic viscosity in the formulation of the Navier-Stokes equations. To determine the surface traction for FSI simulations, the surface pressure and surface velocity gradient must be multiplied by the fluid density

$$S_{traction} = A\rho(\mathbf{n} \cdot p + \nu(\mathbf{SnGrad} \cdot \Delta \mathbf{u})) \tag{A.4}$$

where A is the surface area, $\mathbf{n}$ is the direction component normal to the interface surface and **SnGrad** is the gradient of a vector normal to the interface surface.

A.2 Solid domain

The structural domain formulation, as described in [128; 129] used for the simulations is presented for structures with large deformations. It is assumed that the material is a

homogeneous, isotropic, elastic structure. The dynamics of a solid structure is defined relating the forces acting upon and within a structure to its deformation. The dynamics of a solid structure is defined in differential form by

$$\rho \frac{\partial^2 \mathbf{u}}{\partial t^2} = \nabla \cdot \mathbf{S} + \rho \mathbf{f} \tag{A.5}$$

where the second derivative of displacement, $\frac{\partial^2 \mathbf{u}}{\partial t^2}$ defines the acceleration of a material point, and the surface forces are defined by the 2^{nd} Piola-Kirchoff stress tensor $\mathbf{S}$ and must be modelled according to the non-linear geometric deformation. To do this, the displacement of a material point $\mathbf{X}$ to a spatial point $\mathbf{x}$ can be defined as

$$\mathbf{x} = \mathbf{X} + \mathbf{u}(\mathbf{X}, t) \tag{A.6}$$

where the deformation gradient can then be defined as

$$F = \frac{\partial x}{\partial \mathbf{X}} = \begin{bmatrix} \frac{\partial x_1}{\partial \mathbf{X}_1} & \frac{\partial x_1}{\partial \mathbf{X}_2} & \frac{\partial x_1}{\partial \mathbf{X}_3} \\ \frac{\partial x_2}{\partial \mathbf{X}_1} & \frac{\partial x_2}{\partial \mathbf{X}_2} & \frac{\partial x_3}{\partial \mathbf{X}_3} \\ \frac{\partial x_3}{\partial \mathbf{X}_1} & \frac{\partial x_3}{\partial \mathbf{X}_2} & \frac{\partial x_3}{\partial \mathbf{X}_3} \end{bmatrix} = \frac{\partial (\mathbf{X} + \mathbf{u})}{\partial \mathbf{X}} = \delta + \frac{\partial \mathbf{u}}{\partial \mathbf{X}} = \delta + \mathbf{H} \tag{A.7}$$

where $\mathbf{H}$ is the displacement gradient and δ is the unit tensor. A strain tensor $\mathbf{E}$ is defined using the newly formulated deformation gradient $\mathbf{F}$

$$\mathbf{E} = \frac{1}{2}(\mathbf{F}^T\mathbf{F} - \delta) = \frac{1}{2}(\mathbf{H} + \mathbf{H}^T + \mathbf{H}^T\mathbf{H}) \tag{A.8}$$

where the calculation of $\mathbf{H}^T\mathbf{H}$ makes the above relation of the deformation gradient non-linear. For cases where the deformation is small, the term $\mathbf{H}^T\mathbf{H}$ is omitted from the strain tensor $\mathbf{E}$. The above strain tensor needs to be related to the stress in the material by a constitutive equation. Here, the 2^{nd} Piola-Kirchoff stress tensor $\mathbf{S}$ relates to the Cauchy stress tensor by

$$\mathbf{S} = J\mathbf{F}^{-1}\sigma\mathbf{F}^{-T} \tag{A.9}$$

where J is the determinant of the deformation gradient F. The relation between the stress and strain is determined by the non-linear strain energy density function

$$\mathbf{S} = \frac{\partial W}{\partial \mathbf{E}} \tag{A.10}$$

If the material in question is

1. isotropic and linearly elastic
2. symmetric for $\mathbf{S}$ and $\mathbf{E}$
3. the stain energy density function is positive definite

then the constitutive relation can be defined as

$$S_{ij} = \lambda E_{kk}\delta_{ij} + 2\mu\mathbf{E} \tag{A.11}$$

where δ_{ij} is the kronecker delta, λ and μ are *Lame* constants defined by the material Young's Modulus, E, and Poisson ratio, ν

$$E = \frac{\mu(3\lambda + 2\mu)}{\lambda + \mu} \tag{A.12}$$

$$\nu = \frac{\lambda}{2(\lambda + \mu)} \tag{A.13}$$

Either the material properties, E and ν, or *Lame* constants, λ and μ, are enough to solve for Equation A.11, which is in turn used to solve for A.5.

Appendix B

Pulse Duplication Experimental Setup

A VivitroLabs (ViVitro Labs Inc., British Columbia, Canada) cardiac pulse duplicator (CPD), model:10647 and serial number:6151, was used to perform the pulse duplication experiments at the University of the Free State. A Carolina Medical Electronics ultrasonic flow meter, model:FM501 and serial number:141602HA, was used to measure the volumetric flow rate through the heart valve. The Vivitro CPD is ISO accredited for performing pulse duplication tests, and is considered a world standard in CPD's. A side view of the CPD is shown in Figure B.1 along with a front view of the CPD in Figure B.2.

The inner section of the aortic chamber is completely filled with fluid, and the outer section is filled with air leading to the aortic root compliance chamber. The inner section of the aortic chamber can be partially emptied to reduce the difference between the peak systolic pressure and end diastolic pressure. The systemic resistance line can be adjusted to adjust the peak systolic pressure.

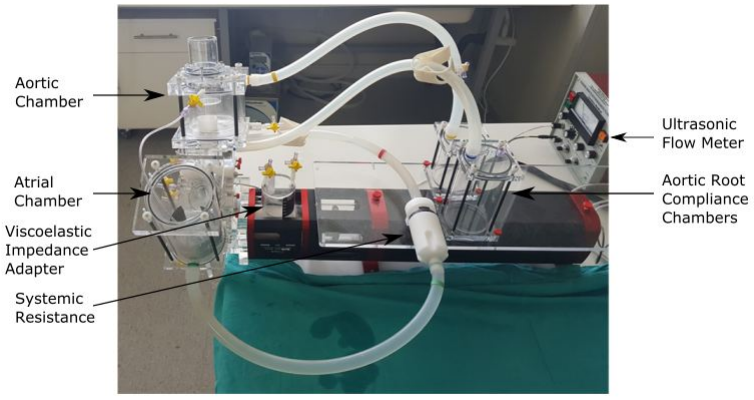

Figure B.1: Side view of the VivitroLabs pulse duplicator

The atrial chamber is open to atmospheric air with an overflow line from inner section of the aortic chamber. The ventricle sac in the ventricle chamber (Figure B.2) is filled

during diastole with fluid from the atrial chamber, and is ejected into the aortic chamber during systole. The ventricle chamber surrounding the ventricle sac is filled with distilled water and is completely filled with no air apart from the VIA chambers.

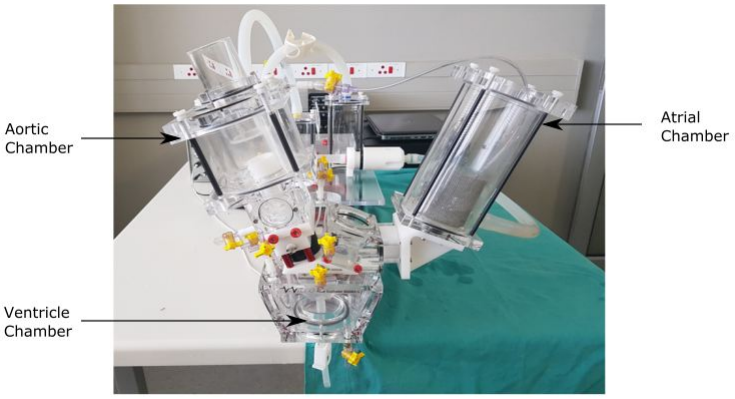

Figure B.2: Front view of the VivitroLabs pulse duplicator

The volume of air in the viscoelastic impedance adapter (VIA) chamber (Figure B.3) impacts the results obtained from pulse duplication, and can be adjusted by inserting air into the chamber through a syringe. A study on the VIA air volumes on the hemodynamic performance was performed and the results shown in the article following [130].

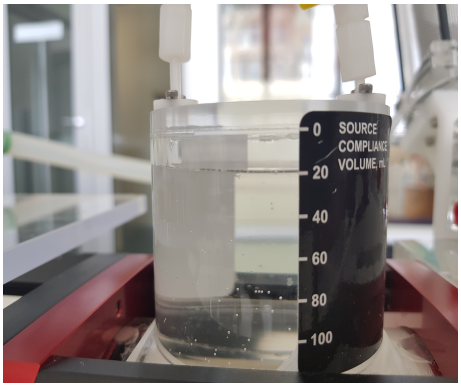

Figure B.3: Side view of the viscoelastic impedance adapter

Evaluating the impact of air compliance chamber volumes on valve performance for three different heart valves

Kyle Davis
Department of Mechanical and Mechatronic Engineering
University of Stellenbosch
Stellenbosch, South Africa
kdavis@sun.ac.za

Jacobus. H. Muller
Department of Mechanical and Mechatronic Engineering
University of Stellenbosch
Stellenbosch, South Africa
cobusmul@sun.ac.za

Chris J. Meyer
Department of Mechanical and Mechatronic Engineering
University of Stellenbosch
Stellenbosch, South Africa
cjmeyer@sun.ac.za

Francis E. Smit
Department of Cardiothoracic Surgery
University of the Free State
Bloemfontein, South Africa
smitfe@ufs.ac.za

***Abstract*— Pulse duplication offers a means of testing the performance of heart valves in an *in-vivo* setting. Results obtained from current pulse duplicators are subject to the setup and physical testing settings. The ViVitro Pulse Duplicator from ViVitroLabs Inc. offer compliance chambers to mimic the systemic circulation of a human body. In addition to the compliance chambers, a Viscoelastic Impedance Adapter (VIA) is situated between the pulse duplicator linear actuator and ventricle sac. The volume of air in the VIA allows for the user to adjust the pressure and flow rate waveforms to mimic physiological waveforms but may also impact on the measured performance of heart valves. Three different valves were tested in a ViVitro pulse duplicator where the VIA air volume was set to 10 ml and 40 ml of air. The air volume shifts the pressure and flow rate waveforms in time and impact the physical operating conditions of the valves with constant input settings in the ViVitest software.**

Keywords—pulse duplication, heart valves, viscoelastic impedance adapter

I. INTRODUCTION

Demand for artificial heart valves (HV's) is growing yearly, where the demand is projected to grow from 290 000 in 2003 to approximately 850 000 replacements by 2050 [1]. Current artificial HV's are inferior in performance to a native HV. In pursuit to find the ideal artificial HV, no effort is spared in testing the HV's, from pulse duplication (PD) to fatigue testing. PD introduces newchallenges, particularly in ensuring that physiologically correct pressure and flow rate waveforms are generated, and to generate these conditions repeatedly [2]. To ensure the correct physiological function of a PD, compliance chambers filled with air are used to mimic the systemic circulation [3]. In addition to systemic compliance chambers, the ViVitro PD (ViVitroLabs Pulse Duplicator, Canada) makes use of an additional compliance chamber called the Viscoelastic Impedance Adapter (VIA), located between the linear actuator and the ventricle sac [4]. The purpose of the VIA is to dampen out the sharp changes in momentum of the fluid surrounding the ventricle generated by the linear actuator, to provide physiologically correct pressure and flow rate waveforms. The amount of damping produced by the VIA can be altered by varying the volume of air inside the VIA output compliance and the VIA source compliance chambers. Along with the change in waveforms, adjustment of the VIA compliance may impact.

The purpose of this study was to perform PD with three different HV's and to vary the VIA compliance to determine the impact on the pressure waveform, volumetric flow rate waveform, the measured input settings and valve performance.

II. EXPERIMENTAL METHODS

A. Pulse duplication

A ViVitroPD was used to perform pulse duplication on three different HV's. Before testing commenced, the flow meter was validated against the linear actuator flow rate and zeroed under no flow conditions. The pressure transducers were validated against a calibrated pressure transducer and zeroed under atmospheric conditions. The VIA compliance air volume was varied between 10 ml and 40 ml of air in each of the output and source compliance chambers.

B. Devices

PD was performed on an Edwards LifeScience Perimount 19mm aortic valve (tissue), a low profile 19mm custom designed polyurethane valve with a height of 5.2mm (PV short), and a tall profile 19mm polyurethane valve with a height of 8.9mm (PV tall). The polyurethane valves were designed to have different hemodynamic behavior by increasing or decreasing the height of the valve, thereby adjusting the angle which the valves occludes the flow through the valve.

A sewing ring was stitched onto the two polyurethanes valves, whereas the tissue valves is supplied with a sewing

ring. The sewing ring was fitted into a plastic retainer which in turn was sealed and inserted into a silicon rubber fitting for the ViVitro PD.

C. Pulse duplication settings

All three valves were tested under the same input conditions. ViVitroViVitest software calculates the cardiac output (CO) as the total volume expelled by the ventricle during forward flow in systole (FFV) minus the regurgitation volume. The CO is therefore not only dependent in the input settings, but also on the valve performance. The second factor affecting the input settings is that the volume of air in the VIA chamber impacts the stroke volume of the ventricle. The higher volume of air in the VIA chamber absorbs a larger displacement of the superpump motion, thereby reducing the measured stroke volume (SV) and FFV.

Three separate tests were conducted:

1. Test 1: beats per minute (BPM) = 70, SV = 72 ml, VIA=10 ml
2. Test 2: BPM = 70, SV = 72 ml, VIA=40 ml
3. Test 3: BPM = 70, CO = Matching Test 1 on ViVitest software (SV adjusted accordingly to match the CO values), VIA = 40 ml

D. Performance measurements

The performance of the valves was evaluated according to ISO 5840 for the pressure drop, effective orifice area (EOA) and regurgitation volume [5].The average pressure drop was calculated by subtracting the aortic pressure from the ventricle pressure, and averaging the pressure drop over the period where the pressure drop was positive. The EOA was determined according to ISO 5840

$$EOA = \frac{Q_{rms}}{51.6\sqrt{\frac{\Delta P}{\rho}}} \quad (1)$$

where ΔP is the mean pressure drop [mmHg], ρ is the fluid density [kg/m^3], and the Q_{rms} was determined by

$$Q_{rms} = \sqrt{\frac{\int_{t_1}^{t_2} q_v(t)^2 dt}{t_2 - t_1}} \quad (2)$$

where t_1 is the time at the start of the positive pressure drop period [s], t2 is the time at the end of the positive pressure drop period [s], and $q_v(t)$ is the volumetric flow rate [ml/s]. The regurgitation volume was determined by measuring the volume of fluid that flowed backwards through the HV after forward flow ended until the end of the cycle.

III. Results

E. Waveforms

The pressure drop waveforms for the PV tall valve is shown in Fig. 1 for Test 1, Test 2 and Test 3. The maximum

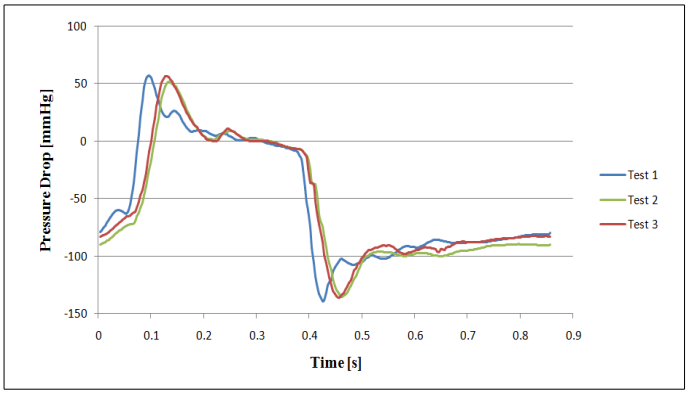

Fig 1: Pressure drop waveform for the PV tall valve for 10ml and 40 ml VIA compliance

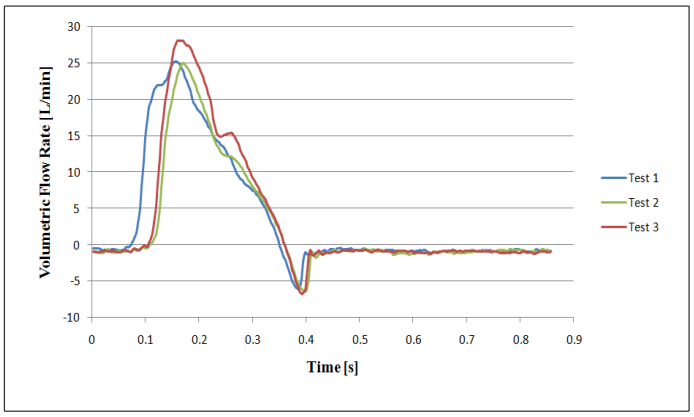

Fig 2: Volumetric flow rate waveforms for the PV Tall valves for 10 ml and 40 ml VIA compliance

pressure drop for Test 2 and Test 3 was shifted later in time by approximately 33 ms when compared to Test 1. A maximum pressure drop of 56.69 mmHg, 51.59 mmHg and 56.26 mmHg was measured for Test 1, Test 2 and Test 3 respectively. The peak back pressure across the closed valve in diastole was lower for Test 2 and Test 3 than Test 1, and were offset in time by approximately 33 ms when compared to Test 1.

The volumetric flow rate for Test 1, Test 2 and Test 3 is shown in Fig. 2. The maximum volumetric flow rate was increased by approximately 2.83 L/min between Test 1 and Test 3, where the FFV was equal. The beginning of forward flow was delayed by approximately 33 ms, similar to that of the pressure drop waveform. The magnitude of the reverse flow through the valve during the leakage phase varied minimally (from approximately 0.4 s and onwards).

F. Valve comparison

The results of the tissue, PV tall and PV short valve is shown in Table 1, Table 2 and Table 3 respectively. Test 1 and Test 2 was run at 70 BPM and 72 SV, however the FFV differed due to the change in the VIA compliance. The difference in the FFV between Test 1 and Test 2 occurred for all HV's. The FFV in Test 3 was increased to that of Test 1 by increasing the SV to 81.5 ml for the tissue and PV tall valve, and to 80ml for the PV short valve. The CO was equal to approximately 4

L/min for Test 1 and Test 3 for the tissue valve, 3.75 L/min for the PV tall valve and between 3.31 L/min and 3.37 L/min for the PV short valve.

Table 1: PD results for the Tissue valve

	Tissue		
	Test 1	Test 2	Test 3
VIA [ml]	10	40	40
BPM	70	70	70
SV [ml]	72	72	81.5
CO [L/min]	4	3.29	4.02
FFV [ml]	63.01	53.24	64.62
Pressure Drop [mmHg]	13.53	11.93	15.45
EOA	1.48	1.45	1.53
Regurgitation [ml]	-5.88	-6.29	-7.18

Table 2: PD results for the PV Tall valve

	PV Tall		
VIA [ml]	10	40	40
BPM	70	70	70
SV [ml]	72	72	81.5
CO [L/min]	3.74	3	3.76
FFV [ml]	63.54	52.3	63.5
Pressure Drop [mmHg]	15.28	14.6	18.35
EOA	1.4	1.31	1.47
Regurgitation [ml]	-10.08	-9.48	-9.76

Table 3: PD results for the PV Short valve

	PV Short		
VIA [ml]	10	40	40
BPM	70	70	70
SV [ml]	72	72	81
CO [L/min]	3.37	2.59	3.31
FFV [ml]	62.52	53.11	63.3
Pressure Drop [mmHg]	26.89	26.86	29.46
EOA	1.02	0.92	1.04
Regurgitation [ml]	-14.33	-16.12	-15.95

The CO varied between the valves for the same test conditions, ranging from a maximum of 4 L/min for the tissue HV to a minimum of 2.6 L/min for the PV short HV.

IV. Discussion

G. *Waveforms*

The pressure drop and volumetric flow rate waveforms in Fig. 1 and Fig. 2 both shifted by approximately 33 ms in time when the air volume was increased from 10 ml to 40 ml. The control of the air volume damped out unphysiological oscillations of the pressure readings due to the rigid walls of the PD. The peak pressure drop was slightly lower for Test 2 due to the lower volume of fluid that flowed through the valve, noted by the lower FFV for Test 2.

The maximum volumetric flow rate increased by approximately 2.83 L/min for Test 3 when compared to Test 1 and Test 2, impacting the physical input conditions that the valve was tested under. The waveform was shifted approximately 33 ms in time for Test 2 and Test 3 due to higher VIA compliance. The added volume of air is compressed during systole as the linear actuator moves forward, delaying the compression of the ventricle and the forward flow through the valve. The VIA air chambers compress and change in volume, reducing the volume of fluid able to pass through the valve, altering the effective SV of the PD. The effect of the shift in the waveforms was observed by Jennings *et al.* for a ViVitro Pulse Duplicator [6].

H. *Valve performance*

When comparing two different HV's, obtaining the same CO may induce a higher FFV for one valve over the other due to differences in the regurgitation volume. If two valves have a CO of 5 L/min at 70 BPM, this equates to 72 ml SV. However, if the CO corrects for the regurgitation, as the ViVitest software does, the correct FFV is the SV plus the regurgitant volume. Therefore, using the CO as a measure of the physical input settings may result in two HV's being tested under different conditions. In order to test for the valves under identical conditions, the pump waveform, heart rate and FFV should be identical. The net volume of fluid output from the ventricle into the systemic circuit will not be identical due to the regurgitation volume, which is valve dependent.

Test 1 and Test 2 had identical heart rate and SV settings. The pressure drop was lower for Test 2 for all HV'scompared to Test 1. The pressure drop of the tissue valve was the lowest due to the soft biological material, followed by the PV tall and the PV short. The PV short had the highest pressure drop due to its low profile and small geometric orifice area during systole, where as the PV tall valve had a large geometric orifice when open. The pressure drop of Test 3 for each valve was larger than Test 1 dueto the increase in FFV. The larger flow rate of the FFV has the effect of increasing the valve pressure drop.

The CO between the valves under the same test conditions varied due to the difference in regurgitation volume. The tissue valve had the lowest regurgitation volume due to the fast closing of the leaflets at the end of systole, and effective sealing of the leaflets during diastole. The PV short valve has a large gap between the leaflets, even under diastolic pressure, resulting in a large leakage volume for the valve.

As the regurgitant volume is a measurement performance outcome, it is incorrect to use it as an input setting by assuming the same CO value for multiple valves. Instead, a constant VIA setting, along with the SV setting should be used as input test conditions to evaluate multiple HV's.

V. Conclusion

The use of a VIA has the potential to create physiologically accurate pressure drop waveforms and volumetric flow rate waveforms due to the added dampening of the VIA air chambers. The air chambers dampen the sudden change in velocity of the pump linear actuator. Too much air in the VIA compliance risks performing experiments at incorrect input conditions, as well as comparing the performance of different valves under differing input conditions.It is recommended to perform all PD tests with 10 ml of air in the VIA chambers as 10 ml provides adequate damping of the oscillations whilst leaving the actual input conditions that the valve experiences similar to the input conditions set in the ViVitest software.

VI. References

[1] M.H. Yacoub and J.J. Takkenberg, "Will heart valve tissue engineering change the world?", *Nat. Clin. Prac.Cardiovas. Med.*, vol. 2, pp. 60–61, 2005

[2] S.M. Retta, J. Kepner, S. Marquez, B.A. Herman, M.C.S. Shu, L.W. Grossman,"In-Vitro Pulsatile Flow Measurement in Prosthetic Heart Valves: An Inter-Laboratory Comparison", *The Journal of Heart Valve Disease*, vol. 26, pp. 72-80, 2017

[3] A. Ducci, F. Pirisi, S. Tzamtzis, G. Burriesci," Transcatheter aortic valves produce unphysiological flows which may contribute to thromboembolic events: An in-vitro study", *Journal of Biomechanics*, vol. 49, pp. 4080-4089, 2016

[4] ViVitroLabs Inc.. 2018. *Pulse Duplicator.* [ONLINE] Available at: https://vivitrolabs.com/product/pulse-duplicator/#. Accessed 22 February 2018].

[5] International Organization for Standardization,"Cardiovascular implants – Cardiac valve prostheses – Part 1: General requirements (ISO 5840-1:2015)

[6] L.M. Jennings, M. Butterfield, P.G. Walker, K.G. Watterson and J. Fisher, "The Influence of Ventricular Input Impedance on the Hydrodynamic Performance of Bioprosthetic Aortic Roots In Vitro", *The Journal of Heart Valve Disease*, vol. 10, pp. 269-275, 2001

Appendix C

Particle Image Velocimetry Setup and Results

The paricle image velocimetry (PIV) test were performed on a cardiac pulse duplicator (CPD) at the University of Stellenbosch. The procedure used for pulse duplication follows the testing conditions described in Section 3.3, and was setup according to Rodriguez [20]. A rig was built to support the camera mounted vertically (Figure C.1) above the viewing areas for the PIV experiments (Figure 4.1). The downstream viewing area was situated between the heart valve and the aortic compliance chamber, where as the upstream viewing area was situated between the ultrasonic flow meter and the heart valve.

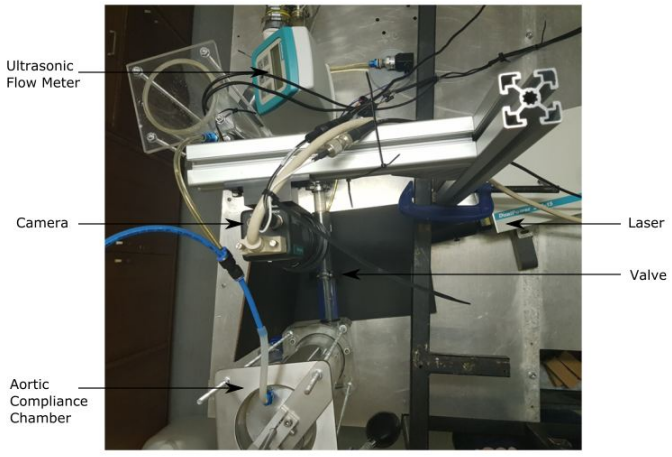

Figure C.1: Vertical position of the camera used for the PIV experiments

The PIV laser was position on a mount horizontally next to the viewing areas and aligned with the mid-plane of the viewing areas (Figure C.2). A clamp holding the upstream and downstream tubes was painted in matte black to limit any laser light scatter. Matte black wooden boards were positioned underneath and behind the viewing areas to reduce laser light scatter.

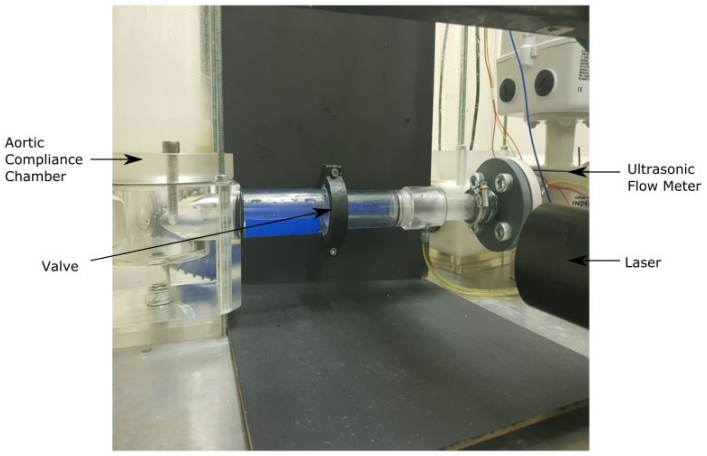

Figure C.2: Horizontal position of the PIV laser

A custom calibrate sheet was manufactured to fit inside of the CPD upstream and downstream tubes whilst filled with fluid. The distance between each black dot is 5 mm and input into the image de-warping function. The calibration sheet before de-warping and after de-warping is shown in Figure C.3. The technical drawings for the revised CPD design for PIV testing is shown in Figures C.4 to Figure C.7.

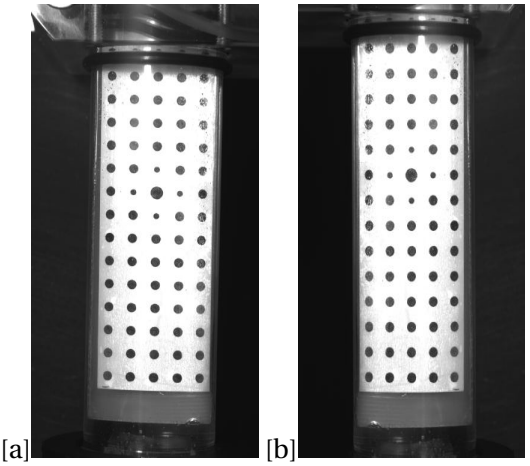

Figure C.3: Images of the calibration sheet (a) before de-warping and (b) after de-warping and image rotation to align with the axis

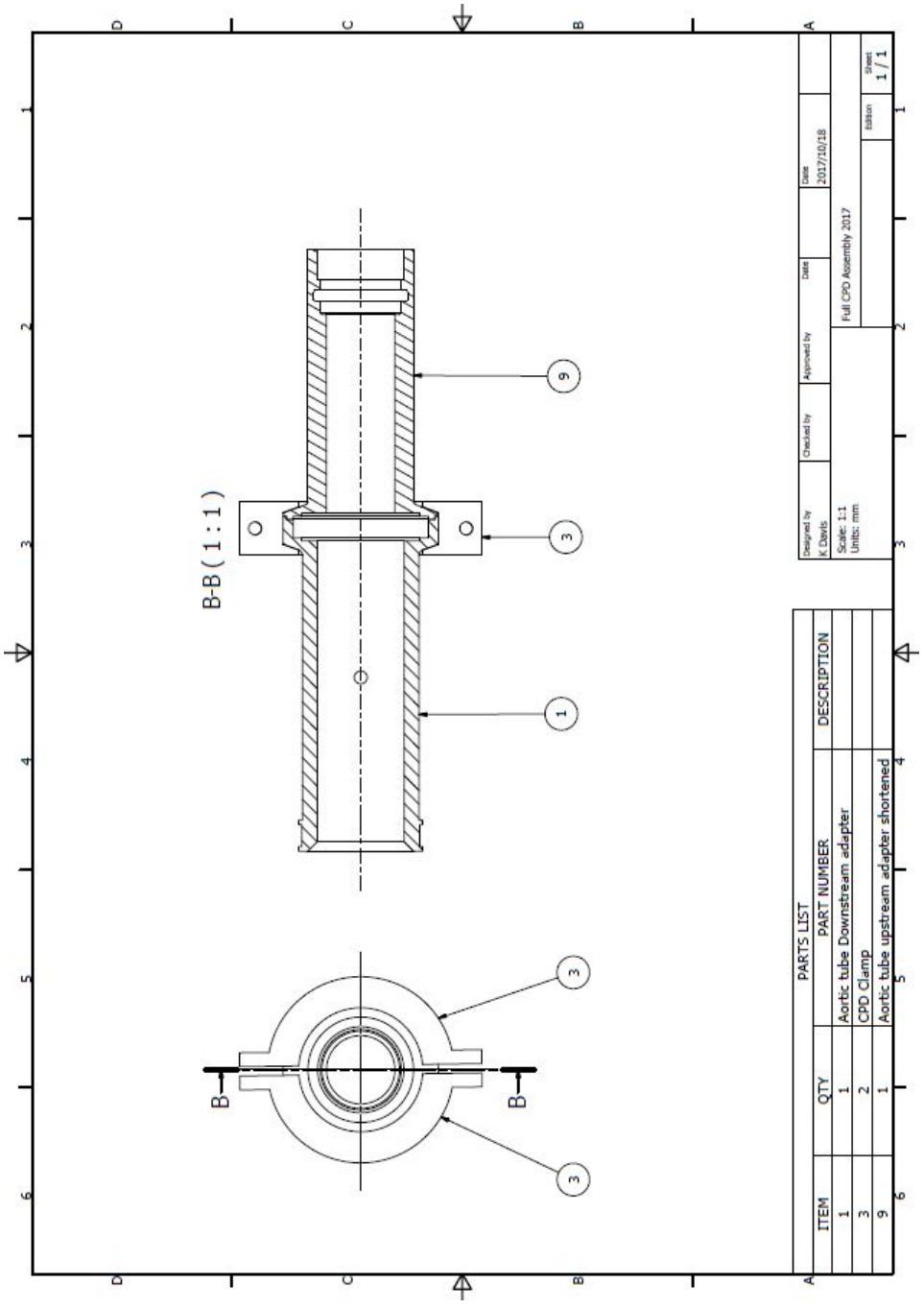

Figure C.4: Assembly IDW drawing of the pulse duplication heart valve housing for the PIV experiments

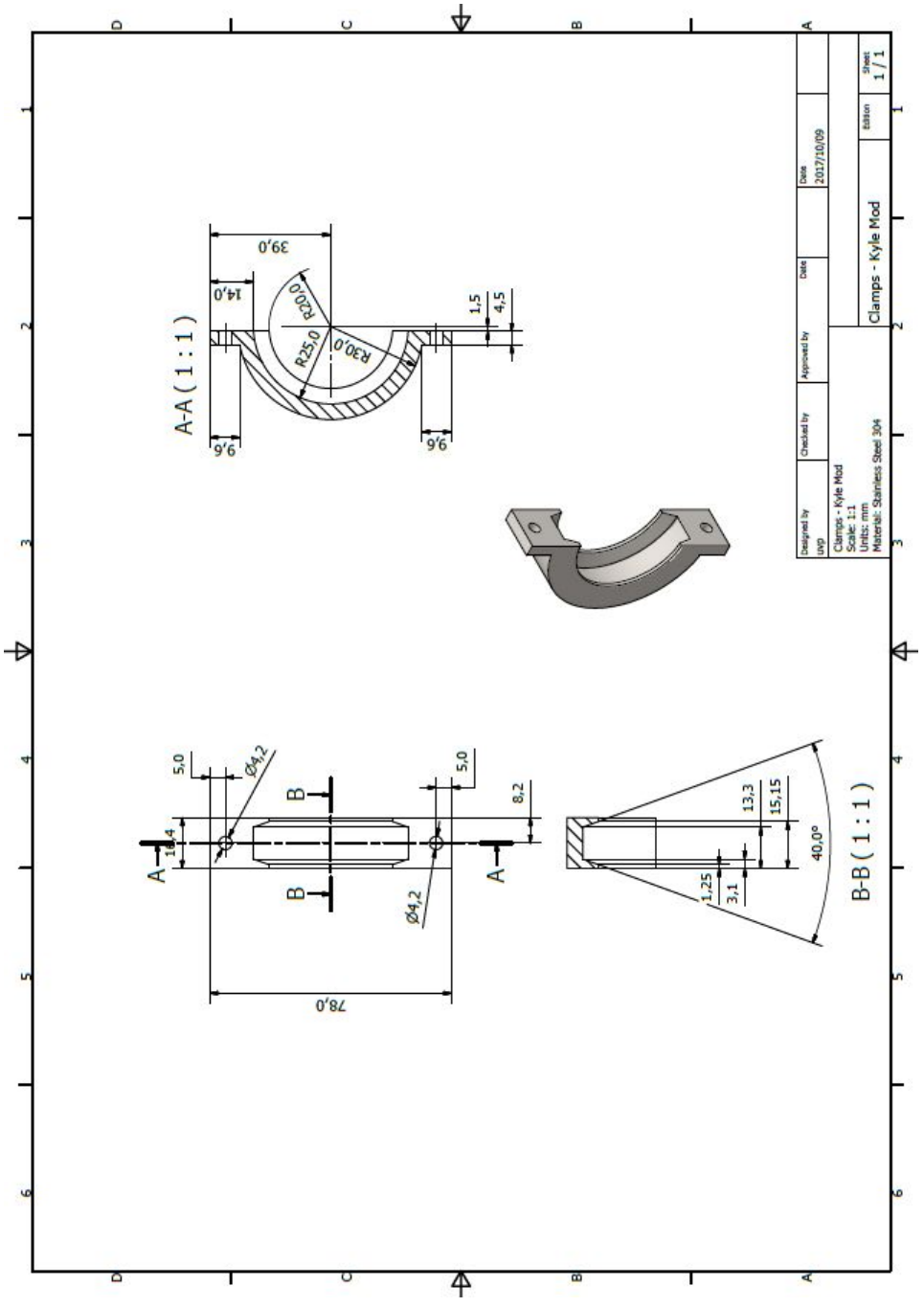

Figure C.5: IDW drawing of the clamps that hold the upstream and downstream adapters together

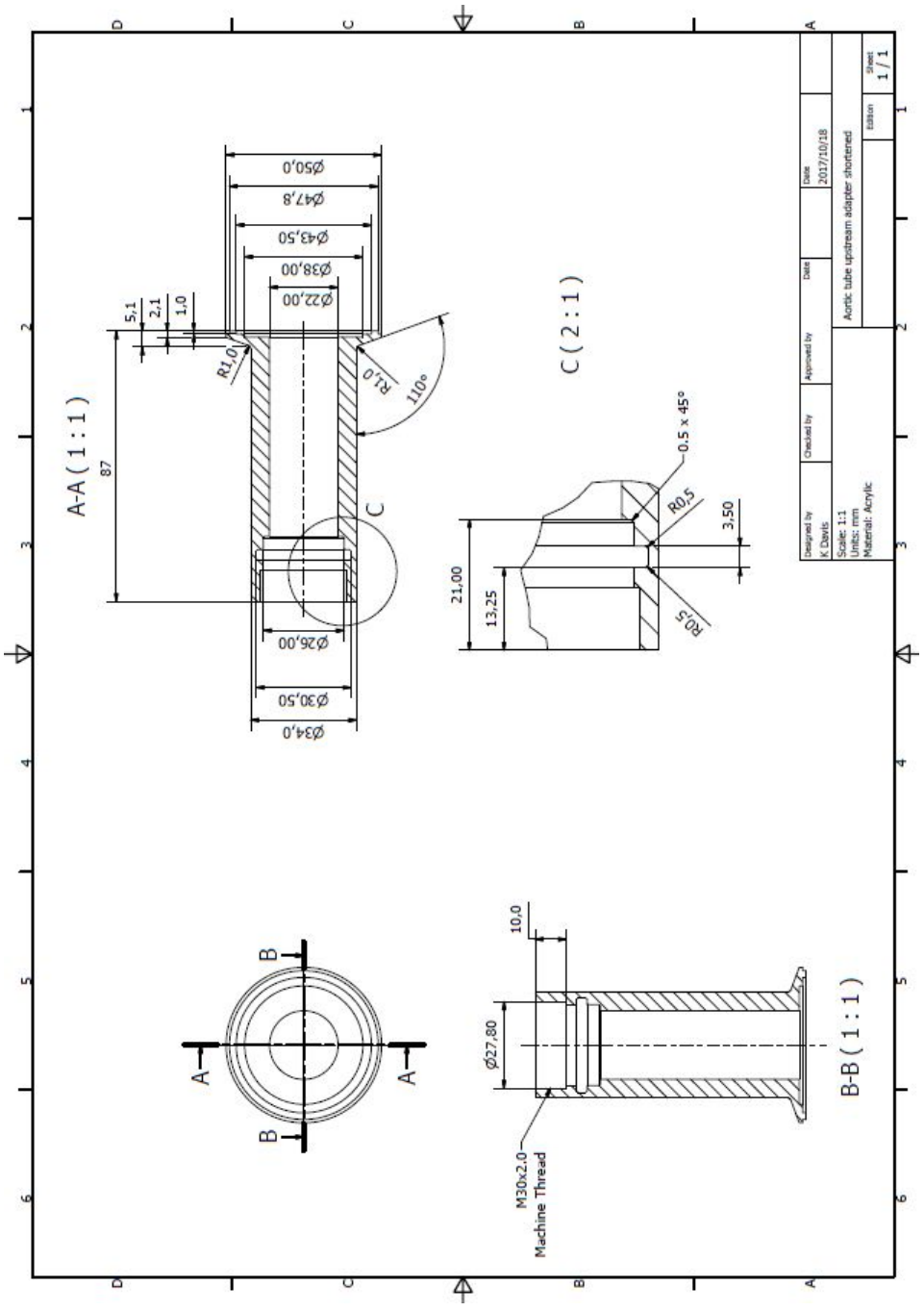

Figure C.6: IDW drawing of the upstream adapter for the viewing area during diastole

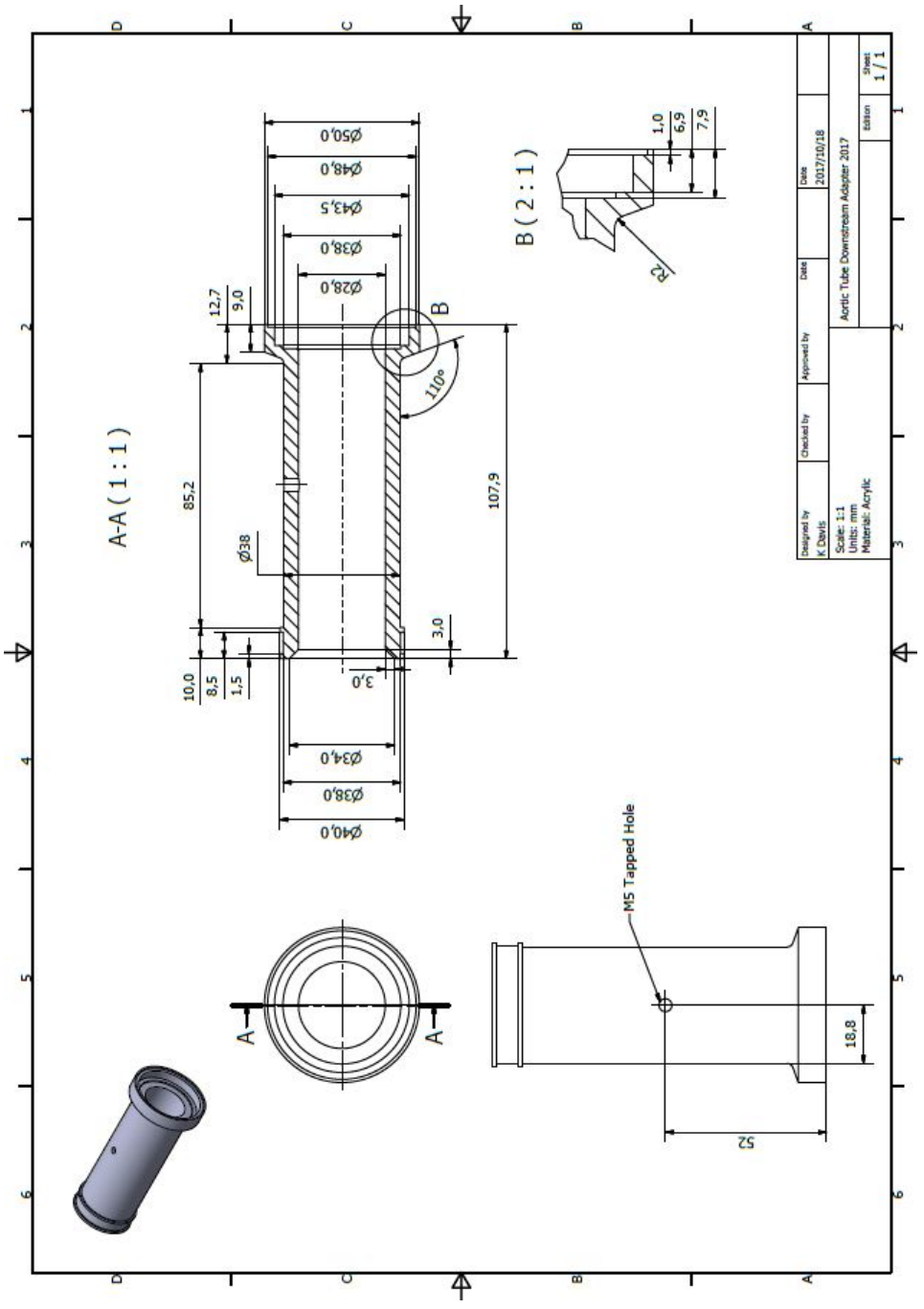

Figure C.7: IDW drawing of the downstream adapter for the viewing area during systole

Appendix D

Software Code

D.1 Numerical simulation software

D.1.1 CalculiX

The first CalculiX adapter in preCICE was released for CalculiX 2.12. A problem was found in the restarting function in CalculiX 2.12 where the restart input file would not load. The preCICE adapter was then modified for CalculiX 2.10, enabling the use of simulation restarts. When restarting a simulation, extremely large force residuals between $1x10^6$ to $1x10^9$ were noticed in the CalculiX simulation and diverged after a few iterations in the first time step. In order to solve the issue, the implementation of the *Precice_Setup* function in *nonlingeo_precice.c* was examined. It was noted the the *Precice_Setup* function was called before *inicont.c*, *results.f* and *mafillsm.f* functions in CalculiX. CalculiX performs a restart by running the previously mentioned C and Fortran functions to set up the solvers based on the previous simulation data. By moving the *Precice_Setup* function in *nonlingeo_precice.c* to the start of the iteration loop and after the aforementioned Fortran files, the CalculiX simulation was able to setup up all necessary matrices necessary for the simulation before changing the force input variables. This adjustment made no impact on the coupling setup for simulations without a restart, but added stability to the restarting capability of CalculiX.

D.1.2 openFOAM mesh motion

The RBF mesh motion solver was previously implemented in two ways:

1. No Coarsening: All of the points on the boundary patches specified in the *DynamicMeshDict* file was used in the RBF interpolation of Equation 2.30. This lead to the formation of extremely large, dense linear matrices to be solved, and made the method unsuitable for meshes larger than 10 000 points with 16Gb of RAM.

2. Coarsening: A greedy algorithmwas implemented to select a small number of points to perform the RBF interpolation within a specified error tolerance. The coarsening algorithms were implemented using either Unit coarsening or Adaptive coarsening.

Unit coarsening applied a unit displacement in the x direction to all boundary points, after which the greedy algorithm iteratively selected specific boundary points to form the RBF interpolation matrix to determine the displacements of all of the points in the mesh. As the greedy algorithm selected points to satisfy the unit displacement and not the actual displacement, movement of the fluid domain interface did not follow the movement of the solid domain. To solve this, adaptive coarsening can be used. Adaptive coarsening applies the actual displacements from the solid domain to the fluid domain interface, after which the greedy algorithm selects points to interpolate the required interface displacements and fixed boundaries in the fluid domain. However the greedy algorithm would be activated every iteration, and may potentially cause floating point errors when performed repeatedly, leading to simulation crashes.

The unit coarsening solver was modified to use the actual displacements of the interface after the solid domain completed the first iteration of the first time step. This meant that a relatively small number of boundary points could be used to perform the RBF interpolation, while satisfying the correct interface displacements within a reasonable error specified by the user.

Adaptive coarsening greedy selection

```
if (! rbf->computed)
{
    this->values = values;       //Values of the actual
        displacements from FSI solver
    matrix unitDisplacements(positions.rows(), positions.cols()
        ); // Matrix defining rows and cols of displacement
    unitDisplacements.setZero();

    assert( unitDisplacement.rows() >= nbMovingFaceCenters );

    /* The setting of the unit displacement becomes redundant.
        Only the actual displacements are
         required for the greedy algorithm

    greedySelection( unitDisplacement );
    */
    greedySelection( this->values );     //Greedy selection with
         actual displacements
    }
}
```

The current implementation of the RBF mesh motion solver implemented in foam-extend-3.2, when used with coarsening, suffers from stability issues. Upon observation, using too few boundary points resulted in the maximum errors of the interpolation being too large. This resulted in the points shared across an inter-processor boundary not being equal, resulting in different face areas of the shared faces across processor interfaces and led to stability problems in the fluid solver. A visual representation of the problem and solution is shown in Figure D.1, where image (a) is the entire mesh over all processors before mesh movement, image (b) is the mesh seen by processor A (domain Ω_A), image (c) is the mesh seen by processor B (domain Ω_B), and image (d) is the entire mesh after

mesh motion with the interface across Ω_A (red line) not matching that of Ω_B (blue line). Initially in the parallelisation of the RBF motion solver, all points on each processor was shared between processors, however this was a very expensive operation and limited the maximum mesh size due to the computational expense. Therefore, the points on each inter-processor interface had to be shared between processors after the RBF interpolation.

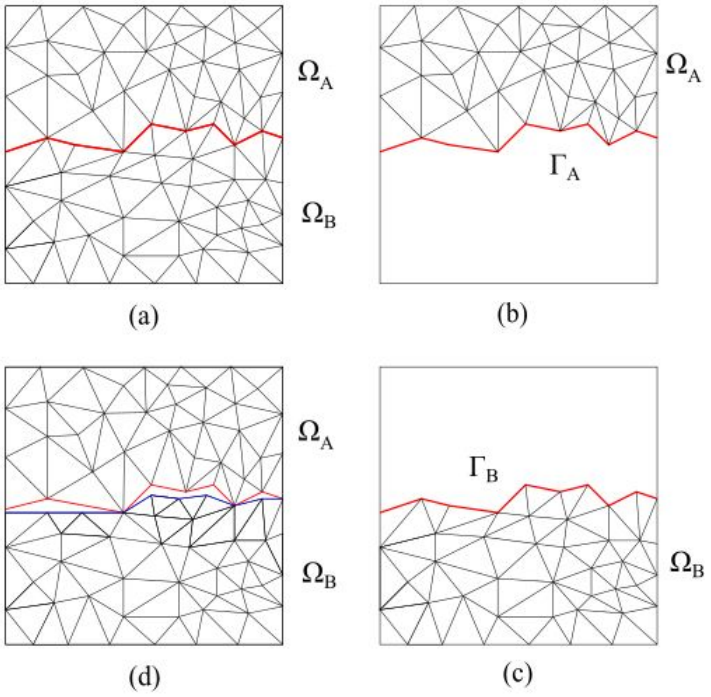

Figure D.1: Mesh partitioning across multiple processes during mesh motion, a) mesh on participant A and B before mesh motion, b) mesh on participant A only, c) mesh on participant B only and d) mesh on participant A and B after mesh motion

The procedure for implementing the changes to the mesh motion procedure to enable parallel operation is summarised in Algorithm 5.

Algorithm 5 openFOAM parallel mesh motion procedure

1: **procedure** ALL PATCHES ARE REQUIRED IN EITHER *movingPatches*, *staticPatches* OR *fixedPatches*
2: search for patches that have not been specified in *dynamicMeshDict* (only inter-processor patches)
3: gather list of points on processor boundary
4: use *reduce* function to gather all inter-processor points into each processor
5: find neighbouring points on each processor
6: set motion of each point equal to each other

Selection of inter-processor points

```
forAll( mesh().boundaryMesh(), i )
{
    const labelList & meshPoints = mesh().boundaryMesh()[i].
        meshPoints();
    vectorField points = mesh().boundaryMesh()[i].points();

    if ( !isFixedPatch && !isStaticPatch && !isMovingPatch &&
        entryNumber == 0)
    {
        // Enforces selection of only one inter-processor
            boundary
        entryNumber = 1;
        // Obtain size of all points on boundary
        meshPointsSize = meshPoints.size();
        // Sets the mesh points size on all processors
        nbGlobalMeshPoints[Pstream::myProcNo()] =
            meshPointsSize;
        // Combines all processors mesh point sizes
        reduce(nbGlobalMeshPoints, sumOp<labelList>());
        // Run through number of points on previous processors
            until the current processor
        for (int i = 0 ; i < Pstream::myProcNo() ; i++)
        {
            globalPointOffset += nbGlobalMeshPoints[i];
        }
        // Set the spatial position of the points in each
            domain equal to the current point spatial position
            on the current processor
        for ( int i = 0 ; i < meshPointsSize ; i++ )
        {
            allProcPointsList[ i + globalPointOffset] =
                meshPoints[i];
            allProcPoints[ i + globalPointOffset ][0] =
                valuesInterpolationField[meshPoints[i]][0];
            allProcPoints[ i + globalPointOffset ][1] =
                valuesInterpolationField[meshPoints[i]][1];
            allProcPoints[ i + globalPointOffset ][2] =
                valuesInterpolationField[meshPoints[i]][2];
        }
        //Combine all new point positions on each processor
        reduce(allProcPointsList, sumOp<labelList>() );
        reduce(allProcPoints, sumOp<vectorField>() );
    }
}
```

Once the new point locations were known and shared, the point spatial positions on processor 2 was set to the point spatial positions on processor 1, processor 3 set to processor 2 and so forth. This limitation means that only the *simple* domain decomposition procedure can be used, where the domain is decomposed in one direction only and enforces one interface between each processor.

New point positions on all processors

```
// New set of points to be shared across processors.
reduce(newAllProcPointsList, sumOp<labelList>() );
// Run through number of points on previous processors until
    the current processor
if (Pstream::myProcNo() == (Pstream::nProcs() - 1) )
{
    for (int i = 0 ; i < Pstream::myProcNo() ; i++)
    {
        globalPointOffset += nbGlobalMeshPoints[i];
    }
    // Loop through each point and set the point ID and spatial
        position equal at every point
    for ( int i = 0 ; i < meshPointsSize ; i++ )
    {
    newAllProcPoints[i + globalPointOffsetNew][] = (
        allProcPoints[i + globalPointOffset][] +
        newAllProcPoints[i + globalPointOffsetNew][] )/2;
    allProcPoints[i + globalPointOffset][] = newAllProcPoints[i
        + globalPointOffsetNew][];
    }
}

.
.
.
// Loop through each point on processor
while ( i < meshPointsSize )
{
    // Set the point ID number
    int pointID = newAllProcPointsList[i + globalPointOffsetNew
        ];
    // Obtain point coordinates at point ID
    valuesInterpolationField[pointID] = newAllProcPoints[i +
        globalPointOffsetNew];
    i++;
}

assert( newPoints.size() == valuesInterpolationField.size() );
// Assert new points to be used by openfoam
newPoints = valuesInterpolationField;
```

D.2 PIV post processing

The velocity vectors are output as an Excel.*csv* file from the Dantec Dynamics post-processing software which was sorted into the x and y components. The VSS was calculated by determining the velocity gradients in the x and y direction and multiplied by the viscosity, μ. The VSS scilab post-processing code is shown in *Viscous Shear Stress* below.

Viscous Shear Stress

```
if ViscousShear == 1 then
    for cycle = CycleStart:CycleEnd
            for i = 1:(N_x - 2)
                for j = 1:(N_y - 2)
                    v_Tau = (v(i+2,j+1,1,cycle) - v(i,j+1,1,
                        cycle))/(2*x);
                    u_Tau = (u(i+1,j+2,1,cycle) - u(i+1,j,1,
                        cycle))/(2*y);
                    tau(i,j,1,cycle) = meu*(v_Tau + u_Tau);
                end
            end
        end
end
```

The RSS and RSS$_{maj}$ scilab post-processing implementation is shown in the *Reynolds Shear Stress* box below. The cycleStart and cycleEnd values could be altered to determine the impact of the number of consecutive image set on the RSS and RSS$_{maj}$ results.

Reynolds Shear Stress

```
for i = 1:N_x
    for j = 1:N_y
        for cycle = CycleStart:CycleEnd
            u_Prime(i,j,cycle) = u(i,j,cycle) - u_mean(i,j);
            v_Prime(i,j,cycle) = v(i,j,cycle) - v_mean(i,j);
            tau_Rey_xx_Ensemble(i,j) = (u_Prime(i,j,cycle)*
                u_Prime(i,j,cycle)) + tau_Rey_xx_Ensemble(i,j);
            tau_Rey_yy_Ensemble(i,j) = (v_Prime(i,j,cycle)*
                v_Prime(i,j,cycle)) + tau_Rey_yy_Ensemble(i,j);
            tau_Rey_xy_Ensemble(i,j) = (u_Prime(i,j,cycle)*
                v_Prime(i,j,cycle)) + tau_Rey_xy_Ensemble(i,j);
        end
        tau_Rey_xx_Ensemble(i,j) = rho*(tau_Rey_xx_Ensemble(i,j
            )/CycleEnd);
        tau_Rey_yy_Ensemble(i,j) = rho*(tau_Rey_yy_Ensemble(i,j
            )/CycleEnd);
        tau_Rey_xy_Ensemble(i,j) = rho*(tau_Rey_xy_Ensemble(i,j
            )/CycleEnd);
        RSS_Maj_Ensemble(i,j) = ((((tau_Rey_xx_Ensemble(i,j) -
            tau_Rey_yy_Ensemble(i,j))/2)^2) + ((
            tau_Rey_xy_Ensemble(i,j))^2))^0.5;
    end
end
```

The TVSS scilab post-processing implementation is shown in the *Turbulent Viscous Shear Stress* box below. The velocity gradient was determined as in the VSS procedure and used as an input into the subgrid scale (SGS) formula to determine the TVSS.

Turbulent Viscous Shear Stress

```
for i = 1:(N_x - 2)
    for j = 1:(N_y - 2)
        v_Tau_mean = (v_mean_2(i+2,j+1) - v_mean_2(i,j+1))/(2*x
            );
        u_Tau_mean = (u_mean_2(i+1,j+2) - u_mean_2(i+1,j))/(2*y
            );

        SGS_S(i,j) = 0.5*(((v_mean_2(i+2,j+1) - v_mean_2(i,j+1)
            )/(2*x))+((u_mean_2(i+1,j+2) - u_mean_2(i+1,j))/(2*y
            )));
        SGS_Delta = (2*x);                  //x and y are the same
        SGS_Constant = 0.17;
        SGS_SBar(i,j) = (2*SGS_S(i,j)*SGS_S(i,j))^0.5;
        SGS_tau(i,j) = -2*(SGS_Constant^2)*(SGS_Delta^2)*
            SGS_SBar(i,j)*SGS_S(i,j);
        SGS_Epsilon(i,j) = -1*(SGS_tau(i,j)*SGS_S(i,j));
        SGS_Shear(i,j) = (0.5*rho*meu*SGS_Epsilon(i,j))^0.5;
        //-------End Smagorinsky SGS Model
            ----------------------

        Kol_Length(i,j) = ((kinVis^3)/SGS_Epsilon(i,j))^0.25;
        Kol_Time(i,j) = ((kinVis)/SGS_Epsilon(i,j))^0.5;
    end
end
```

Appendix E

Numerical Coupling Validation

E.1 Wave propagation through tube

Wave propagation through a tube has been studied by numerous researchers to validate FSI coupling [131; 132; 133; 134; 135]. However, the literature shows various input settings for the simulations, including differences in viscosity, pressure inlet magnitude and the time the pressure inlet was applied for. A summary of the various input settings found in literature are shown in Table E.1.

Table E.1: Numerical simulation input settings for various wave propagation simulations

Author	Fluid density	Fluid viscosity	Solid density	Young Modulus, E	Poisson	Pressure inlet	Time applied
Gerbeau [131]	1 g/cm3	0.03 poise	1.2 g/cm3	3x10^6 dynes/cm2	0.3	13332 dynes/cm2	0.005 s
Oxtoby [134]	1 g/cm3	0.03 g/cm s	1.2 g/cm3	3*10^6 g/cm s2	0.3	13332 Pa	0.003 s
Formaggia [132]	1 g/cm3	0.03 poise	1.2 g/cm3	3x10^6 dynes/cm2	0.3	13332 dynes/cm2	0.005 s
Fernandez [133]	1 g/cm3	0.003 poise	1.2 g/cm3	3x10^6 dynes/cm2	0.3	1.3332*10^(-4) dynes/cm2	0.003 s
Blom [135]	1000 kg/m3	0.003 Pa.s	1200 kg/m3	3x10^5 N/m2	0.3	1333.2 Pa	0.003 s

The pressure and velocity plots through the tube at 5 ms and 10 ms is shown in Figure E.1 and Figure E.2 respectively. The simulations were performed with the same input settings as Blom [135]. The simulations were also performed using the input pressure setting at the inlet according to Malan and Oxtoby [134], however large displacements were observed and the simulation diverged after 2 ms of simulation time. The results of the tube wall deformation agreed with Blom [135] and showed the stability and rapid convergence of the IQN-ILS coupling scheme.

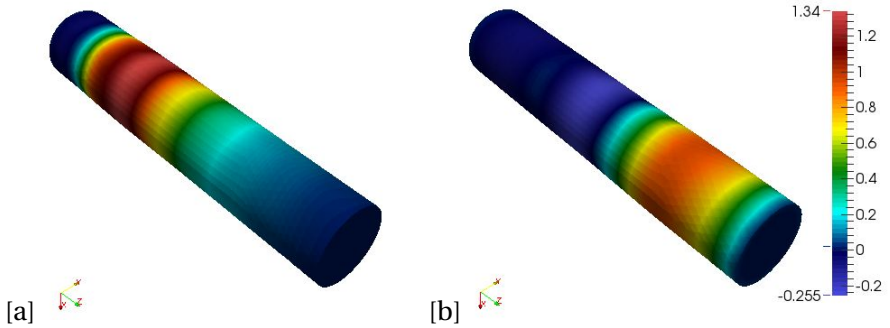

Figure E.1: Pressure distribution through an expanding tube

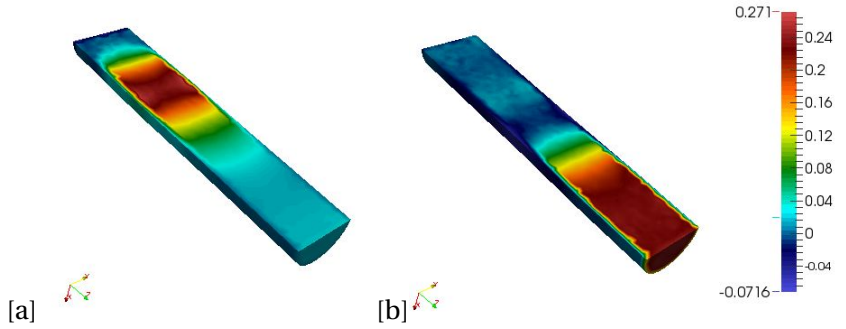

Figure E.2: Velocity distribution through an expanding tube

E.2 Beam in cross flow

A simple beam in cross flow (Figure E.3) was performed for the FSI validation as performed by Blom [135] and Richter [136]. As with the wave propagation problem, the setup of the simulations differ in the literature. Both Blom [135] and Richter [136] used a fluid and solid density of 1000 kg/m^3, a kinematic viscosity of 0.001 m^2/s and a Poisson's ratio of 0.4. The simulation setup differed with the Young's modulus, where Blom [135] used a value of 1x10^4 Pa and Richter [136] used 5x10^5 Pa.

Blom [135] recorded a maximum x-direction displacement at point location (0.45,0.15,0.15) of approximately 0.018 m. In attempting to replicate the simulation of Blom [135], divergence occurred due to the low Young's modulus. The simulation performed with the input settings of Richter [136] converged. The velocity profile around the beam at time 40 ms and 400 ms is shown in Figure E.4a and Figure E.4b.

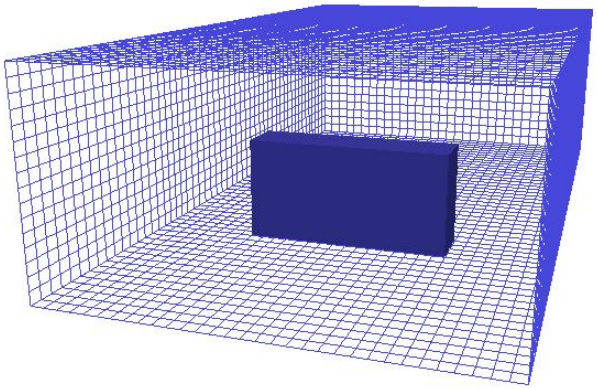

Figure E.3: Geometry of a beam in cross flow

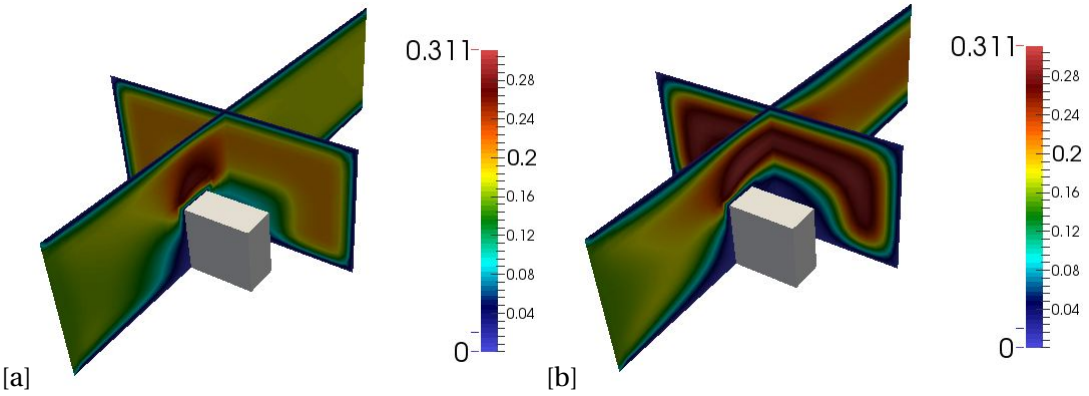

Figure E.4: Velocity distribution through the beam in cross flow simulation at (a) 40 ms and (b) 400 ms

The beam displacement in the x-direction at point location nearest to (0.45,0.15,0.15) is displayed in Figure E.5a, where the steady state displacement of the beam was 0.00022 m. The beam drag force is displayed in Figure E.5b, where the steady state drag force of the beam was 5 N.

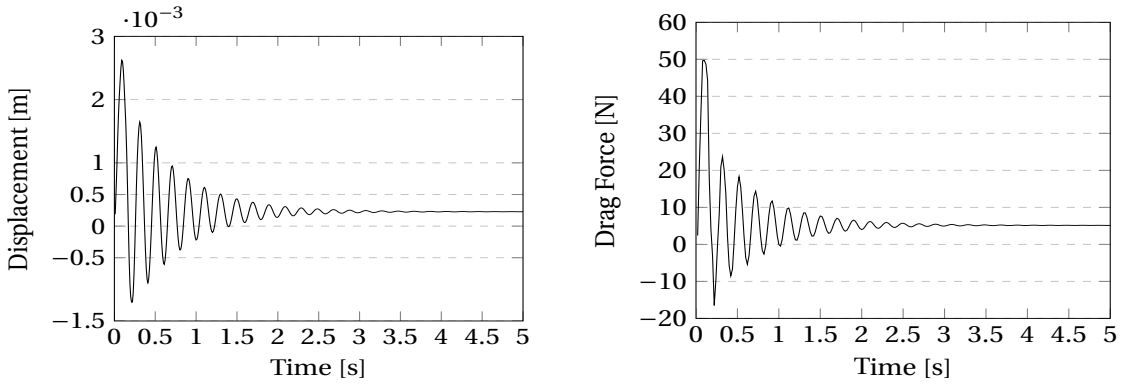

(a) (b)

Figure E.5: Steady state results of the beam in cross flow for the (a) x-displacement and (b) drag force

E.3 Mesh motion limitations

Currently, only 3D simulations can be performed with openFOAM and CalculiX coupled together. CalculiX is a 3D only solver and requires the out of plane deformations to be fixed for 2D simulations. However, the preCICE configuration file must still stipulate a 3D simulation case. Forcing the simulation to be 3D in the preCICE configuration file forces the openFOAM simulation to be 3D. openFOAM is able to perform 2D simulations by enforcing the out of plane direction displacement to be zero, however this is not performed for 3D simulations. By setting the preCICE configuration file to function in 3D, the openFOAM mesh motion solver is forced to function in 3D only. The current openFOAM and CalculiX combination forces the problem to be 3D.

Appendix F

Mesh Independence and Mesh Motion Analysis

F.1 Mesh independence

A mesh independence study was performed by examining the solid stress, fluid velocity and fluid pressure results. The solid displacement and von Mises stresses of the coarse, medium and fine solid domain is shown in Table F.1. The medium and fine solid displacements shows little difference at 15 and 20 ms. A larger difference was noted in the maximum von Mises stress between the medium and fine mesh, shown in Figure F.1. Examining the stress in the medium mesh, the maximum stress occured in one small region of the mesh at the top of one pillar only. The stresses shown in Figure F.1 for the medium mesh is between 2.17 MPa and 2.71 MPa for the region surrounding the edge where the polyurethane material attaches to the titanium frame, similar to the von Mises stress magnitude of the fine mesh.

Table F.2 shows the maximum fluid velocity and fluid pressure for the coarse, medium and fine fluid meshes. The coarse mesh did not match the velocity or pressure of the medium and fine mesh. The maximum fluid pressure, measured in mmHg, differed minimally between the medium and fine mesh. A small difference in the maximum velocity was observed between the medium and fine mesh. The fluid pressure and moving interface velocity at 25 ms into systole is shown in Figure F.2. The fluid pressure throughout the domain shows minimal difference between the meshes, and the maximum interface velocity differed by 0.001 m/s. For the remainder of the simulations, the medium fluid mesh was used with the fine solid mesh.

Table F.1: Solid displacement and von Mises stress for the coarse, medium and fine solid mesh at various time steps

	Solid Displacement (mm)				
	5ms	10ms	15ms	20ms	25ms
Coarse	0.209	0.878			
Medium	0.205	0.901	1.64	2.44	3.49
Fine	0.197	0.921	1.68	2.43	3.21

	Solid Stress (MPa)				
	5ms	10ms	15ms	20ms	25ms
Coarse	1.09	2.54			
Medium	1.35	3.33	4.53	5.31	5.69
Fine	0.668	1.54	2.07	2.4	2.51

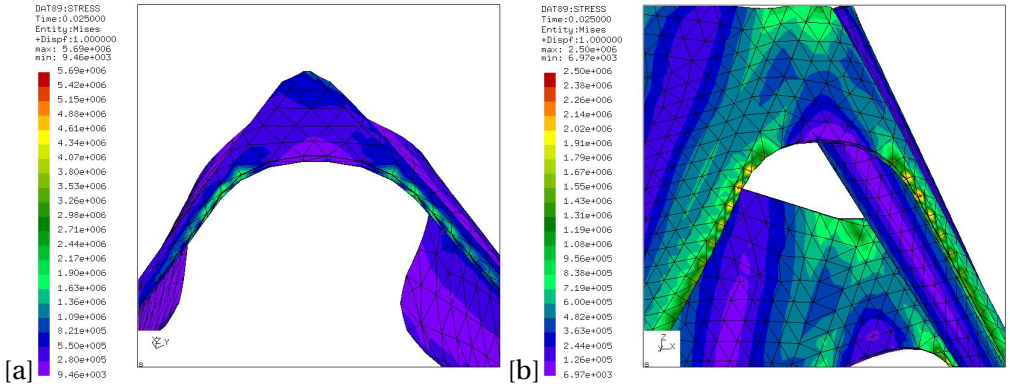

Figure F.1: von Mises distribution through the (a) medium and (b) fine solid mesh

Table F.2: Fluid pressure and velocity for the coarse, medium and fine fluid mesh at various time steps

	Pressure			Velocity		
	10ms	20ms	25ms	10ms	20ms	25ms
Coarse	14.53	15.16	-	0.624	0.991	-
Medium	14.05	14.45	3.47	0.524	0.859	0.876
Fine	14.13	14.45	3.48	0.551	0.868	0.874

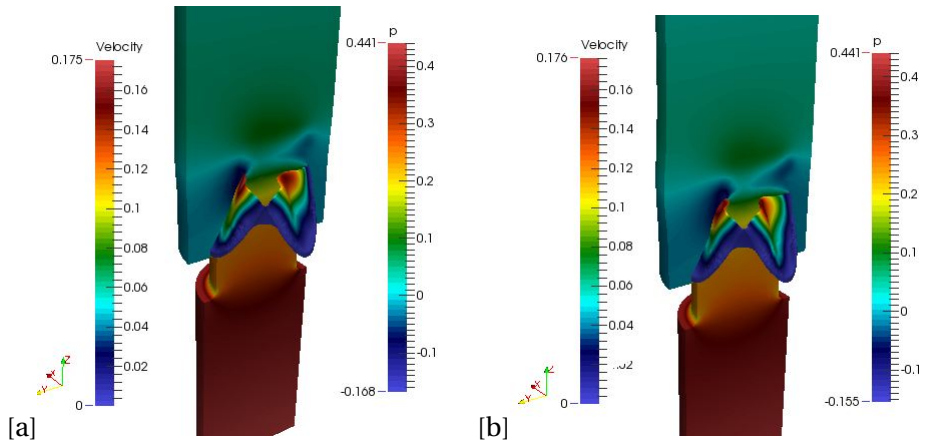

Figure F.2: Fluid pressure and heart valve leaflet velocity during heart valve opening for the (a) medium mesh and (b) fine mesh

F.2 Mesh motion analysis

Slices of the fluid domain mesh near the leaflet edge of the heart valve is shown in Figure F.3 and Figure F.4. Figure F.3 shows the mesh deformation from 0 ms (a) to 10 ms (b) of the simulation. The fluid domain had to stretch significantly between the leaflets as only a small number of cells could be placed in the gap. Mesh quality significantly improved after remeshing (Figure F.4a), where the simulation was restarted and ran until 25 ms (Figure F.4b). The amount of cell stretching is larger further from the moving interface, helping to maintain mesh quality on the moving interface. The fluid domain was remeshed after 25 ms, significantly improving the mesh quality until 31 ms, where a twisting motion of the leaflets occured before fully opening. The RBF mesh motion solver was easily able to handle the mesh deformation without forming negative cell volumes during the intervals specified above. This enabled complete opening of the heart valve leaflets after three remeshing steps.

After 31 ms, the heart valve twists in order to fully open, where one side of the leaflet moves towards the centre of the domain whilst the other half moves towards the outer wall. Once the first half of the leaflet has reached the open position near the outer wall, the second half is pulled outwards towards the outer wall. During this period, the RBF mesh motion function with coarsening has trouble with maintaining suitable mesh quality on the interface in certain regions. The only solution that could be found to solve for the mesh motion between 31 ms and 40 ms was to use a coarse mesh. The coarse mesh was able to easily deform until 40 ms. The medium size mesh was used from 40 ms, however a very grainy region on one leaflet was observed. The grainy region did not impact the convergence ability of openFOAM, but may cause accuracy problems. The mesh at 50 ms and the velocity profiles across the centre of two leaflets, one smooth and the other grainy, is shown in Figure F.5. A slightly higher velocity magnitude on the outer side of the grainy leaflet was observed, however this was due to the leaflet itself having a higher velocity magnitude as it was still moving outwards.

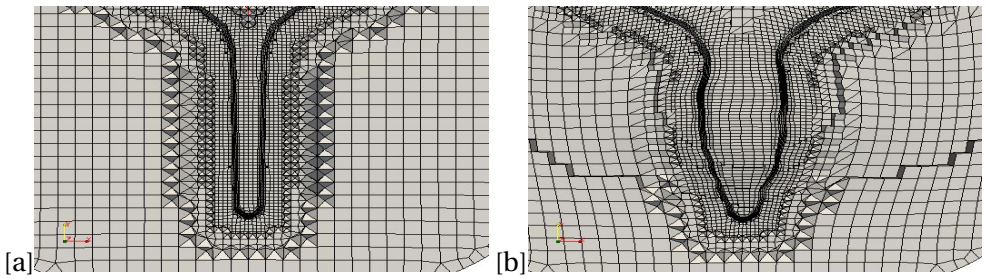

Figure F.3: Fluid domain mesh at time steps (a) 0 ms and (b) 10 ms before remeshing

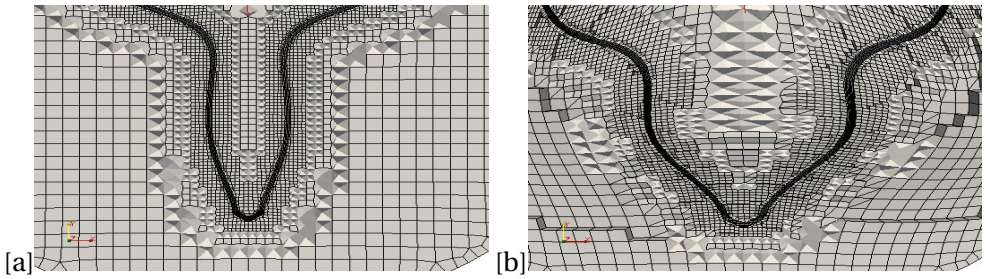

Figure F.4: Fluid domain mesh at time steps (a) 10 ms after remeshing and (b) 25 ms before remeshing

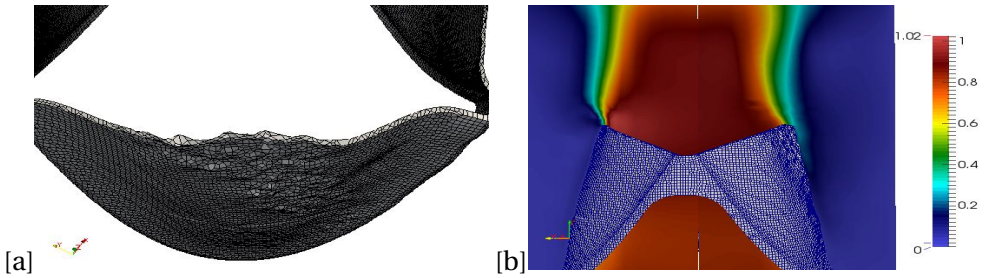

Figure F.5: Fluid domain (a) surface mesh quality after heart valve opening and (b) fluid domain velocity due to distorted surface mesh

The slice of the fluid domain mesh viewed from above the heart valve is shown in Figure F.6 from 230 ms and 274 ms simulation time before remeshing. The cells in the region above the frame pillars where two heart valve leaflets meet become squeezed as the leaflets approach each other, reducing the quality of the cells in these regions and causing the simulation to diverge due to inverted elements.

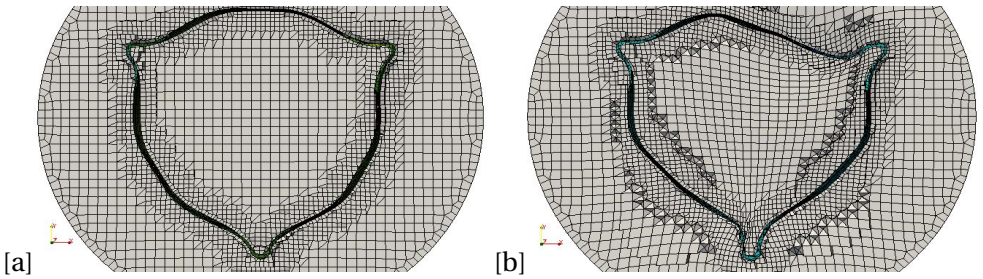

[a] [b]

Figure F.6: Fluid domain mesh at time steps (a) 230 ms and (b) 274 ms before remeshing

As the heart valve closes, a similar phenomena is observed during closing to that of opening, where one half of the leaflet moves inwards before the other half. The remeshed fluid domain at 274 ms and deformed mesh at 282 ms is shown in Figure F.7. The remeshed fluid domain at 282 ms and deformed mesh at 287 ms is shown in Figure F.8. The closing phase occurs quicker than the heart valve opening. During closing, the mesh elements pinch together and causes the simulation to diverge, thereby increasing the number or remeshing steps necessary to perform the closing of the heart valve. Instability of the solid domain simulation after restarting at 286 ms limited the further simulation of the closing of the heart valve.

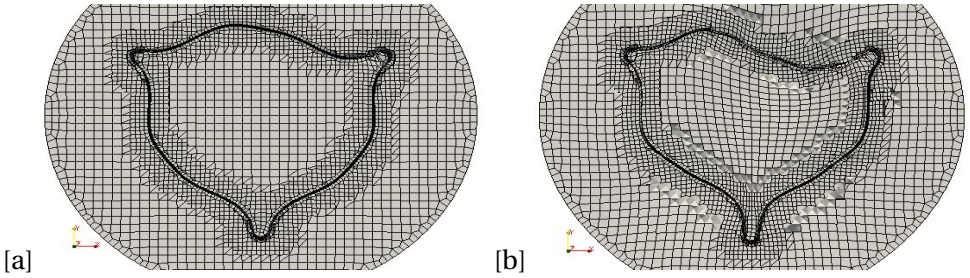

[a] [b]

Figure F.7: Fluid domain mesh at time steps (a) 274 ms after remeshing and (b) 282 ms before remeshing

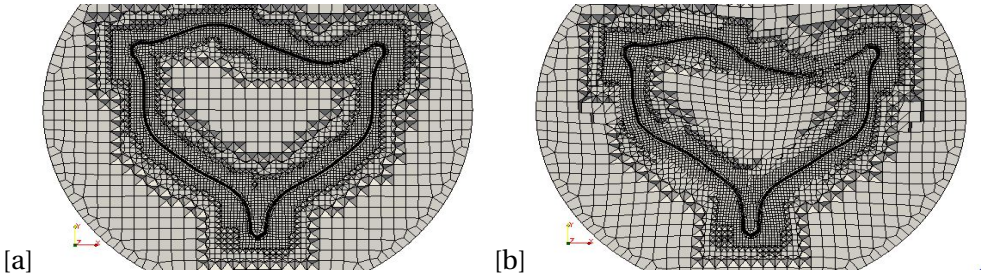

[a] [b]

Figure F.8: Fluid domain mesh at time steps (a) 282 ms after remeshing and (b) 287 ms before remeshing

Appendix G

Numerical Simulation Settings

G.1 openFOAM settings

All the relevant openFOAM settings including the finite volume schemes, solvers and dynamic mesh dictionaries are provided below. The first order backward differencing scheme was used as it is an efficient time integration scheme, as well as unconditionally stable for first and second order time integration [135]. The least squares gradient scheme was used as it provides second order accurate solutions even when extended to unstructured meshes [137; 138].

fvSchemes

```
    ddtSchemes
    {
            default bdf1;
    }

    gradSchemes
    {
        default Gauss linear;
            grad(U) leastSquares;
        grad(nuTilda) cellLimited Gauss linear 1;
        grad(k) cellLimited Gauss linear 1;
        grad(omega) cellLimited Gauss linear 1;
        grad(epsilon) cellLimited Gauss linear 1;



    }
    divSchemes
    {
        default Gauss linear;
        div(phi,U) Gauss linearUpwindV leastSquares;
        div(phi,k)  Gauss linearUpwind cellLimited Gauss linear
             1;
        div(phi,epsilon) bounded Gauss linearUpwind grad(
            epsilon);
        div(phi,omega) bounded Gauss linearUpwind grad(omega);
        div(phi,nuTilda) bounded Gauss linearUpwind grad(
```

```
            nuTilda);
        div((nuEff*dev(grad(U).T()))) Gauss linear;
    }
interpolationSchemes
    {
        default linear;
        interpolate(HbyA) linear;
   }
laplacianSchemes
    {
        default Gauss linear limited 0.333;
    }
snGradSchemes
    {
        default limited 0.333;
    }
fluxRequired
    {
        default yes;
        p ;
    }
```

fvSolutions

```
PIMPLE
{
        nCorrectors 3;
        nNonOrthogonalCorrectors 2;
        tolerance 1e-5;
        relTol 0;
        maxIter 30;
        minIter 1;
        pisoTol 1e-1;
            residualControl
           {
                    U   1e-8;
                    p   1e-7;
           }
}

solvers
{
        p
        {
           solver GAMG;
           agglomerator faceAreaPair;
            mergeLevels 1;
            cacheAgglomeration true;
            nCellsInCoarsestLevel 500;
            tolerance 1e-7;
            relTol 1e-1;
            smoother GaussSeidel;
            nPreSweeps 1;
            nPostSweeps 2;
```

```
            nFinestSweeps 2;
            minIter 1;
                maxIter 5;
        }

        U
        {
            solver smoothSolver;
            smoother GaussSeidel;
            tolerance 1e-8;
            relTol 1e-2;
            minIter 1;
        }
            relaxationFactors
        {
                        U 0.5;
                        UFinal 0.5;
                p 0.2;
                        pFinal 0.2;
                        Up 0.2;
        }
}
```

The dynamicMeshDict requires all the patches to be specified, either as fixed, static, other or fixed. The coarsening can be set to select a minimum or maximum number of points. The *polynomial* and *cpu* settings must both be true to enable the addition of the polynomial terms in the RBF interpolation matrix for added stability. The thin-plate-spline basis function was used as it is independent of any user defined constant. The use of local basis functions is possible, however they are also implemented with a sparse matrix solver, so there is no gain in RAM or CPU usage.

dynamicMeshDict

```
dynamicFvMesh dynamicMotionSolverFvMesh;
solver RBFMeshMotionSolver;

movingPatches ( interface );
staticPatches ( );
otherPatches ( );
fixedPatches ( Fixed Inlet Outlet Wall );

coarsening
{
  enabled true;
  tol 1.0e-3;
  minPoints 1000;
  maxPoints 2000;
  livePointSelection false;
  tolLivePointSelection 1.0e-2;
  exportSelectedPoints false;
  twoPointSelection false;
}

interpolation
```

```
{
  function TPS;
  polynomial true;
  cpu true;
  //function WendlandC0;
  //radius 0.006;
}

faceCellCenters false;
```

G.2 CalculiX settings

There are certain key notes to make regarding setting up a CalculiX input file for FSI simulations. The first to note is that all points throughout the domain should be saved in a *.msh* file (not a specific requirement but will reduce debugging time). The points specific to individual interfaces should be placed inside a *.nam* file (such as *interface.nam*).

The forces specified on the boundary must be specified in each direction for each surface. Therefore the **CLOAD* input must be set individually for the *x*, *y* and *z* direction. Failing to do so would cause an error the array length of the force vectors and arbitrary forces will be applied to random points on the interface surface. The **DYNAMIC* settings must contain the time step and end time of the simulation (0.001 s and 0.01 s in the example below). The end time of the precice-config file must coincide with the specified end time for a restart file to be written at the simulation end. More information on the CalculiX configuration file can be found in

Calculix.inp

```
*INCLUDE, INPUT=all.msh
*INCLUDE, INPUT=fixed.nam
*INCLUDE, INPUT=interface.nam
*MATERIAL, Name=EL
*ELASTIC
 25600000, 0.3
*DENSITY
 1200.0
*SOLID SECTION, Elset=Eall, Material=EL
*STEP,NLGEOM,INC=1000000
*DYNAMIC,DIRECT,ALPHA=-0.2
 0.001,0.01
*BOUNDARY
 Nfixed,1,3,0
*CLOAD
 Ninterface,1,0
 Ninterface,2,0
 Ninterface,3,0
*RESTART, WRITE,FREQUENCY=1
*NODE FILE
 U
*EL FILE
 S, E
```

```
*END STEP
```

Calculix-Config

```
participants:

    Calculix:
        interfaces:
        - nodes-mesh: Calculix\textunderscore Mesh
          patch: interface
          read-data: [Forces0]
          write-data: [DisplacementDeltas0]

precice-config-file: ../fluid/constant/precice-config.xml
```

G.3 preCICE settings

The preCICE config file provides the necessary information for preCICE to perform FSI coupling. The config file is divided into:

1. data vectors and mesh names
2. defining the participants and mapping method
3. coupling scheme and post-processing technique

The input settings for the confid file can be changed in accordance with the preCICE XML reference [139]. The initial relaxation was set to *0.001* to provide stable operation during the first two time steps before the IQN-ILS coupling scheme could begin. Eight time steps were reused as it provided good efficiency in terms of CPU speed and RAM usage.

precice-config.xml

```
<?xml version="1.0"?>

<precice-configuration>

    <solver-interface dimensions="3">

        <data:vector name="Forces0" />
        <data:vector name="DisplacementDeltas0" />

        <mesh name="Fluid_Nodes">
            <use-data name="DisplacementDeltas0" />
        </mesh>

        <mesh name="Fluid_CellCenters">
            <use-data name="Forces0" />
        </mesh>
```

```
        <mesh name="Calculix_Mesh">
            <use-data name="DisplacementDeltas0" />
                <use-data name="Forces0" />
        </mesh>

        <participant name="Fluid_Solver">
            <use-mesh name="Fluid_Nodes" provide="yes" />
            <use-mesh name="Fluid_CellCenters" provide="yes" />
            <use-mesh name="Calculix_Mesh" from="Calculix" />
            <write-data mesh="Fluid_CellCenters" name="Forces0"
                 />
            <read-data mesh="Fluid_Nodes" name="
                DisplacementDeltas0" />
            <mapping:nearest-neighbor direction="write"
                constraint="conservative" from="
                Fluid_CellCenters" to="Calculix_Mesh" timing="
                initial"/>
            <mapping:nearest-neighbor direction="read"
                constraint="consistent" from="Calculix_Mesh" to=
                "Fluid_Nodes" timing="initial"/>
            <master:mpi-single/>
        </participant>

        <participant name="Calculix">
            <use-mesh name="Calculix_Mesh" provide="yes"/>
            <use-mesh name="Fluid_Nodes" provide="yes" />
            <write-data mesh="Calculix_Mesh" name="
                DisplacementDeltas0" />
            <read-data mesh="Calculix_Mesh" name="Forces0" />
        </participant>
        <m2n:sockets distribution-type="gather-scatter"
            exchange-directory="../" from="Fluid_Solver" to="
            Calculix" />

        <coupling-scheme:serial-implicit>
            <timestep-length value="1.0e-3" />
            <max-timesteps value="10" />
            <participants first="Fluid_Solver_Coarse" second="
                Calculix" />
            <exchange data="Forces0" from="Fluid_Solver_Coarse"
                 mesh="Calculix_Mesh" to="Calculix" />
            <exchange data="DisplacementDeltas0" from="Calculix
                " mesh="Calculix_Mesh" to="Fluid_Solver_Coarse"
                />
            <relative-convergence-measure limit="1.0e-3" data="
                DisplacementDeltas0" mesh="Calculix_Mesh"
                suffices="0" />
            <max-iterations value="150" />
            <extrapolation-order value="2" />

            <post-processing:IQN-ILS>
                <data name="DisplacementDeltas0" mesh="
                    Calculix_Mesh" />
                <initial-relaxation value="0.001" />
                        <max-used-iterations value="100" />
```

```
                <timesteps-reused value="8" />
                <filter type="QR1" limit="1e-5" />
            </post-processing:IQN-ILS>

        </coupling-scheme:serial-implicit>

    </solver-interface>

</precice-configuration>
```

An alternative to the IQN-ILS coupling scheme is Aitken relaxation, shown below. The code below replaces the IQN-ILS post-processing procedure above.

precice-config.xml

```
            <post-processing:aitken>
                <data name="DisplacementDeltas0" mesh="
                    Calculix_Mesh" />
                <initial-relaxation value="0.001" />
            </post-processing:aitken>
```

Appendix H

List of Publications

Publications

1. Davis, K., Muller, J.H., Meyer, C.J. and Smit, F.E., *Evaluating the impact of air compliance chamber volumes on valve performance for three different heart valves*, IEEE Xplore.

Conference Proceedings

1. Oral presentation: *Evaluating the impact of air compliance chamber volumes on valve performance for three different heart valves.* The South African Biomedical Engineering Conference in Stellenbosch, South Africa, April 2018

2. Oral presentation: *Numerical modelling of heart valves using preCICE* The European Computational Fluid Dynamics Conference, Glasgow, Sctoland, June 2018

3. Oral presentation: *Evaluation of Reynolds, viscous and turbulent viscous shear stress obtained from particle imaging velocimetry in the design of low cost polyurethane valves.* The World Congress of Biomechanics, Dublin, Ireland, July 2018